

NORTHWESTERN UNIVERSITY

Identifying Support Effects in Nanoparticle Catalysis

A DISSERTATION

SUBMITTED TO THE GRADUATE SCHOOL
IN PARTIAL FULFILLMENT OF THE REQUIREMENTS

for the degree

DOCTOR OF PHILOSOPHY

Field of Materials Science and Engineering

By

Zachary R. Mansley

EVANSTON, ILLINOIS

December 2021

© Copyright by Zachary R. Mansley 2021

All Rights Reserved

ABSTRACT

Identifying Support Effects in Nanoparticle Catalysis

Zachary R. Mansley

This thesis focuses on identifying structure-property-performance relationships in supported nanoparticle catalysts, where an active catalyst material is supported on a high surface area substrate. Identifying these relationships in supported nanoparticle catalysts can be quite challenging, as the complex structure of these catalysts results in numerous potential sources for changes to the catalytic performance. This work surmounts that hurdle by minimizing the number of changing properties between different substrate materials and carefully studying and tabulating the properties that do change, allowing any variations to the performance of the catalyst system to be rationalized.

To reduce the potential sources of changes to material properties and performance, a series of structurally similar lanthanide scandate supports with well-defined facets were used. This allows changes in both behavior of the supported nanoparticles and in catalytic testing to be compared to the few changing material properties between the substrates, and structure-property-performance relationships to be identified. This is in contrast to comparing supports such as alumina and titania, where the vast number of differences

between the two complicate the identification of any particular one as the source of change in performance.

The lanthanide scandate nanoparticles are synthesized by collaborators as beveled cubes, and their surfaces are studied first using a combination of spectroscopy, electron microscopy, and density functional theory. A double layer, Sc-rich surface termination is identified on a majority of the exposed surface area, indicating that the surface structure and chemistry is unchanged across the series of support materials. The surfaces of the beveled edges are also identified, and theoretical Wulff shapes are calculated using the excess energies of each surface as a function of the chemical potential of the scandium species at the surface.

Following these studies, Au nanoparticles were deposited on the support surfaces and the structures, orientations, and interfacial energies of the supported nanoparticles were assessed and compared across the different supports. Many twinned particles of Au were identified, so a modified Winterbottom construction was derived to model the thermodynamics of these particles. Studying the populations of Au on the supports, the crystallinity and preferred orientation of the Au nanoparticles was found to be different on each support, and it is hypothesized that this is due to the different lattice parameter of the various lanthanide scandate materials. Additionally, the structure of the double layer reconstruction on the pseudocubic (100) surfaces of the lanthanide scandate nanoparticles forms a structurally matched interface with the (110) surface of FCC nanoparticles – an interface not frequently observed.

The Au/LnScO₃ materials were then used as catalysts for CO oxidation, and Au/NdScO₃ was found to have the highest activation energy barrier for the reaction. Furthermore,

desorption measurements identified NdScO_3 as the support with the most basic surface. This behavior was found to be the result of chemically active 4f electrons in NdScO_3 , identified by density functional theory and published spectroscopy of the different lanthanide scandates. While the activity of these electrons increased the energy barrier for CO oxidation using Au, preliminary work with Pt suggests that this effect can be leveraged to reduce energy barriers in other systems.

Acknowledgements

First and foremost I must thank my advisor, Professor Laurie Marks, for his guidance and patience throughout my Ph.D. While he, much to my chagrin at the time, would rarely give straight answers or solutions to problems that he surely could have; he instead pushed and prodded me in the right direction to solve my scientific problems and attain solutions by my own hand. They say hindsight is 20/20, and considering those frustrating times now I surely would not be the scientist I am today without that experience. I also need to thank Professor Ken Poeppelmeier, while I may not *officially* be advised by him, our meetings and discussions always gave me new insight into our work (and your seemingly infinite, personal knowledge of the scientific community never ceased to amaze). I would also like to thank the other members of my committee, Professor Justin Notestein and Professor Peter Voorhees, for serving on both my thesis committee and my qualifying committee with Laurie and Ken.

I would not be writing this document today without the consistent support of all the members of the LDM group present between 2016 and today, including Pratik, Say, Tassie, Lawrence, Betty, Alex, Ryan, Chris, Tiffany, Karl, Emily, Ahmet, Shawn, and Edmund. I have to start with Ryan, who pioneered the synthesis of the lanthanide scandate particles that are the foundation of this thesis, woke up early (most!) every morning to come to the gym, and was always around to both brew and drink beer with me. Thanks to Chris, who tolerated me strolling into his cubicle multiple times per day to pitch ideas and ask

DFT questions, as well as his collaboration on XPS and the single crystal work. Thank you to Tassie for picking me up and driving me to and from Argonne countless times during the first few years, as well as the road trip to Pittsburgh. Thank you Tiffany for the help with learning DFT and how computers work, and Emily for taking over all of the responsibility for this project in the future. I would also like to thank the members of the Poeppelmeier group who listen to my materials focused group meeting talks and always have unique insights towards my projects.

My ability to perform experiments is entirely due to those who trained me and provided technical support along the way. For electron microscopy, I must thank Laurie again for his wealth of knowledge and insight, as well as Dr. Jianguo Wen at Argonne National Laboratory for instruction in practical aberration correction and allowing me to use the ACAT. Thanks to Dr. Neil Schweitzer at REACT for his trainings and discussions on all things catalysis and desorption, and everyone else who helped me along the way.

A special thanks to all of the members of my CFRS soccer team, Give 'Em El, for giving me a social life outside of school (even though you were all mostly Northwestern students) and inviting me to play with you all for years. Another thanks to my friend Jonathan Lopez, who I met in undergrad and since moving to Chicago would force me to come out and have fun.

Thank you to my family, your emotional support, and the holidays back home, were indispensable towards my mental health and the online card games were always a highlight. The few months when Kyle came to live in my one bedroom apartment with me were some of the best of the pandemic. They say you can't choose your family, but if I could, I wouldn't choose differently. Also, even though he won't be able to read this,

thank you to my dog, Billy. He brings so much to my life, and for better or for worse he forces me to go outside every day!

And of course, thank you to Natalie. Thank you for your presence in my life, always talking to me over the phone, and for all of the visits over the years. I could not have done this journey alone, and knowing you were there, even if it was in New York, made all of the difference. Thank you for everything you've done, and I can't wait for the rest of our time together not separated by 800 miles.

Chemistry without catalysis, would be a sword without a handle, a light without brilliance, a bell without a sound.

Alwin Mittasch

I would like to start by emphasizing the importance of surfaces. It is at a surface where many of our most interesting and useful phenomena occur. We live for example on the surface of a planet. It is at a surface where the catalysis of chemical reactions occur. . . In electronics, most if not all active circuit elements involve non-equilibrium phenomena occurring at surfaces.

Walter H. Brattain

God made the bulk; the surface was invented by the devil.

Wolfgang Pauli

List of abbreviations

ACAT: Argonne Chromatic Aberration-corrected TEM.

AFM: atomic force microscopy.

ALD: atomic layer deposition.

CSL: coincident site lattice.

DFT: density functional theory.

DPC: differential phase contrast.

DRIFTS: diffuse reflective infrared Fourier transform spectroscopy.

EDX: energy dispersive x-ray spectroscopy.

EELS: electron energy loss spectroscopy.

HAADF: high angle annular dark field.

HREM: high resolution electron microscopy.

ICP-MS/OES: inductively coupled plasma mass spectrometry/optical emission spectroscopy.

LTP: lamellar twinned particle.

MAADF: moderate angle annular dark field.

MIGS: metal induced gap states.

MTP: multiply twinned particle.

pDOS: partial density of states.

RMS: root mean square.

STEM: scanning transmission electron microscopy.

TEM: transmission electron microscopy.

TOF: turnover frequency.

TPD-MS: temperature programmed desorption with mass spectrometry.

XPS: x-ray photoelectron spectroscopy.

Table of Contents

ABSTRACT	3
List of abbreviations	6
Acknowledgements	8
Table of Contents	12
List of Tables	16
List of Figures	18
Chapter 1. Introduction	33
1.1. Motivation	33
1.2. Faceted Lanthanide Scandate Supports	36
1.3. Organization	38
Chapter 2. Experimental and Theoretical Methods	40
2.1. Transmission Electron Microscopy	40
2.2. Density Functional Theory	49
2.3. X-ray Photoelectron Spectroscopy	50
2.4. ICP-MS/OES	51
Chapter 3. Surfaces of (110) LnScO ₃ (Ln = Gd, Tb, Dy) Single Crystals	53

	13
3.1. Introduction	53
3.2. Methods	54
3.3. Experimental Results	56
3.4. XPS Model	58
3.5. Valence Neutrality of the Double Layer	61
3.6. Double Layer Solution and Electronic Structure	63
3.7. Conclusions	65
Chapter 4. LnScO ₃ Nanoparticle Surfaces	66
4.1. Introduction	66
4.2. Methods	68
4.3. {100} _{pc} Surfaces	69
4.4. {110} _{pc} Surfaces	78
4.5. Summary of Surface Energies and Theoretical Wulff Shapes	82
4.6. Conclusions	84
Chapter 5. Thermodynamics of Supported Polycrystals - a Modified Winterbottom	
Construction	85
5.1. Introduction	85
5.2. Theory	87
5.3. 5-fold Example	91
5.4. Sensitivity to Changing Parameters and Kinetics	94
5.5. Experimental Observation	96
5.6. Conclusions	100

	14
Chapter 6. Au Morphologies and Interfaces on LnScO ₃	101
6.1. Introduction	101
6.2. Methods	102
6.3. Results	103
6.4. Conclusions	111
Chapter 7. CO Oxidation with Au/LnScO ₃	113
7.1. Introduction	113
7.2. Methods	115
7.3. Results	117
7.4. Discussion	122
7.5. Conclusions	128
Chapter 8. The Pt(110) on LnScO ₃ (110) Interface	129
8.1. Introduction	129
8.2. Methods	130
8.3. Interfacial Structure	131
8.4. Induced Charges	133
8.5. Electronic Structure of the Interface	135
8.6. Conclusions	137
Chapter 9. Summary and Future Work	139
9.1. Summary	139
9.2. Theoretical and Experimental Analysis of Pt/LnScO ₃ - Electronic Structure	139
9.3. Experimental Analysis of Pt/LnScO ₃ - Adhesion and Orientation	141

9.4. Using Pt/LnScO ₃ for New Catalytic Reactions - Particle Strain Mismatch vs Support Basicity	143
9.5. Synthetic Control of LnScO ₃ Substrate Faceting	144
References	146
Appendix A. Surface Energy Minimization Proof	164
Appendix B. Substitution of γ_{eff}	166
Appendix C. Au Particle Size Statistics	168
Appendix D. Expanded turnover frequency (TOF) Results	170
Appendix E. Layer Resolved DOS of the Interface	173

List of Tables

- 4.1 Number of atoms and k-point meshes used in density functional theory (DFT) calculations. With the exception of the “(001) double layer (1x1)” and the “(010) Ln_2O vacant” structures, all k-point densities are the same. Those exceptions were not converged to higher densities as it quickly became apparent they were not realistic solutions. 69
- 4.2 Relative energy of each (1x1) and (2x2) structure compared to the minimum energy solution, 2a. Structures 2a-2g represent the (2x2) structures and 1a/1b are (1x1). Structures 2a-2d are translations of the low energy solution in Figure 4.3(b/d), while 2e-2g are based on the solved (110) structure, which is shown to be comparatively unfavorable on this surface. 74
- 4.3 Energy differences compared to the minimum energy structure the single layer reconstruction. The energies of structures 1 and 2 are essentially equivalent considering k_bT at room temperature. 76
- 4.4 Energy differences compared to the minimum energy structure the $(110)_{pc}$ single layer reconstruction. 80

4.5	Excess surface energies of the LnScO_3 surface reconstructions discussed in this chapter and the (110) double layer from Chapter 3, along with the areal density of excess scandium at the surface.	83
7.1	Comparison of CO_2 binding populations on LnScO_3	119
C.1	Average Au sizes (d_{avg} , given in nm), standard deviations (STD), and root mean square (RMS) disagreement of the post-catalysis samples	169

List of Figures

- 1.1 Pt nanoparticles supported on SrTiO₃ nanocuboids prepared via ALD. 34
- 1.2 Secondary electron images of different LnScO₃ supports demonstrating a faceted, cuboidal morphology. 36
- 1.3 . The structure of a typical LnScO₃ material (NdScO₃) is given in (a) viewed down the [110] axis. Pink octahedra are ScO₆ units and the orange atoms are Nd. There are two pseudocubic units per unit cell, stacked in the [001] direction. Pseudocubic lattice parameters are given in (b) along with lattice parameters of the noble metals Ag, Au, Pt, and Pd. 37
- 2.1 Schematic representation of the interaction between an electron beam and a specimen with the resulting signals that are generated. Figure adapted from [1]. 41
- 2.2 Spherical (a) and chromatic (b) lens aberrations. A spherical aberration more heavily focuses waves far from the center of the lens, and a chromatic aberration more heavily focuses waves of a higher energy. Figure adapted from [2]. 44

- 2.3 The high resolution electron microscopy (HREM) image of SmScO_3 in (a) demonstrates the variation in contrast as a function of sample thickness despite no changes to the crystal structure, exemplifying the difficulty of directly interpreting HREM images. The general process for multislice simulation is seen in (b), which is reproduced from [3]. 47
- 2.4 A gold nanoparticle changing shape under the electron beam over time due to electron beam irradiation. 48
- 3.1 Atomic force microscopy (AFM) (a-c) and surface sensitive electron diffraction (d-f) of the studied LnScO_3 materials. GdScO_3 (a,d), TbScO_3 (b,e), and DyScO_3 (c,f) all show similarly stepped surfaces and a (1x1) periodicity. Scale bars in (a)-(c) are 200 nm those in (d)-(f) are 2 nm^{-1} . 56
- 3.2 Angle resolved x-ray photoelectron spectroscopy (XPS) intensity ratios of the integrated scandium 2p and lanthanide 3d signals as a function of angle demonstrate a relative increase in the Sc signal as the angle of the detector with respect to the surface normal is increased, indicating a Sc rich surface. The signals were normalized such that the ratio at $\theta = 0$ was 1. 57
- 3.3 Modeled intensity ratios compared to the DyScO_3 experimental data. The data has the best match to the double layer, though the model is too coarse and experimental uncertainty too high to predict an exact layer chemistry. 60

- 3.4 Comparison of layer valence in a 242 (SrTiO_3) and a 332 (DyScO_3) perovskite. 62
- 3.5 DFT relaxed structure of the double layer termination on DyScO_3 (110). Considering the $Pbnm$ reference frame, the view directions are $[110]$ (a), $[\bar{1}10]$ (b), $[001]$ (c). Bulk ScO_6 octahedra are colored grey, surface ScO_5 are blue, and surface ScO_4 are red. Dy atoms are pictured as blue spheres. 63
- 3.6 Partial density of states (pDOS) of GdScO_3 (a) and DyScO_3 (b). The figure lines are colored to correspond with Figure 3.5, where red is associated with ScO_4 , blue with ScO_5 , and black are the bulkmost ScO_6 . The gray shaded region shows the pDOS from a separate, bulk calculation. The Fermi energy (0) is set at the highest occupied state of the O 2p. The occupied Sc and unoccupied O states have been scaled up by a factor of 10 for clarity. 64
- 4.1 HREM of a faceted NdScO_3 nanoparticle in (a), along with a corresponding power spectrum of the image in (b). The particles primarily expose the $\{100\}_{pc}$ surfaces, along with the $\{110\}_{pc}$ at the edges. Secondary electron images of the nanoparticles used as supports in the catalytic experiments in Chapter 7 are shown in (c). 67
- 4.2 Beam/sample interaction geometry when imaging down a $[100]_{pc}$ and $[110]_{pc}$ zone axis of a faceted, cuboidal particle with beveled edges, along with kinematically calculated diffraction patterns of the

potential zone axes. When imaging along a $[100]_{pc}$ direction, the sample is thick but the view direction is easily discernible between the different $[100]_{pc}$ directions, the $[110]$ and $[001]$. Conversely for the $[110]_{pc}$ zone axes, it is possible to image using a very thin region of sample, but it can be difficult to determine the specific zone axis as the diffraction patterns of two of the $[110]_{pc}$ directions are nearly identical.

68

4.3 Aberration corrected HREM of the Sc-rich double layer terminations on the LnScO_3 materials. Figures (a-e) are LaScO_3 , NdScO_3 , SmScO_3 , GdScO_3 , and DyScO_3 in order viewed along a $[110]_{pc}$ axis, where the small thickness and surface structure allow for a clear visualization of the double layer. Shown in (f) and (g) are the (001) LaScO_3 surface and (110) GdScO_3 surface respectively viewed along a $[100]_{pc}$ axis. In (f) and (g) the sample thickness and structure do not allow for a clear visualization of the double layer, but the overlaid multislice simulation, outlined in red, in 3g shows a good match at the surface. 3c also has an outlined multislice simulation overlaid.

70

4.4 DFT relaxed structures of the low energy solutions of the (001) double layer solution on GdScO_3 with (1x1) (Figs a/c) and (2x2) (Figs b/d) symmetries. (a) and (b) show plan views of the surfaces along the $[001]$ direction, while (c) and (d) are profile views along the $[010]$. Grey polyhedra are bulk ScO_6 units, pink are surface ScO_6 , blue are surface ScO_5 , and red are surface ScO_4 . Purple atoms are Gd.

71

- 4.5 Multislice simulations of selected (2x2) structures on the GdScO_3 (001) surface are shown above. As noted in Table 4.2, 2a is the low energy solution while 2b is very close in energy such that it likely coexists on the surface. Structure 2e is modeled after the (110) double layer reconstruction before relaxation. As shown in the simulations, variations to the specific polyhedral arrangements do not generate a significant change in the profile view images as the structures are two-dimensional projections. 72
- 4.6 pDOS of the Ln 4f, Sc 3d, and O 2p states of the double layer (001) structure on GdScO_3 (a) and NdScO_3 (b). In all cases, black lines represent the bulkmost unit cell. For the Ln 4f and O 2p, red lines are the surface-most atoms, and in the Sc 3d purple lines represent Sc in ScO_6 polyhedra, blue in ScO_5 [], and red in ScO_4 . The occupied Sc 3d and unoccupied O 2p states are magnified by a factor of 10 for visibility as noted in the figure. 73
- 4.7 Aberration corrected HREM of a single layer region on a $(100)_{pc}$ surface of LaScO_3 . Outlined in red is a multislice simulation based on the predicted low energy structure in Figure 4.8. The rapidly changing thickness of the nanoparticle moving away from the surface makes a larger multislice simulation unfeasible. 76
- 4.8 The DFT predicted structure for the single layer termination on the (110) surface is pictured in (a), with polyhedra colored as described

- in Figure 4.4. (b) The pDOS of the surface is shown in (b) with the same convention as Figure 4.6. 77
- 4.9 HREM of two $(110)_{pc}$ surfaces are shown on the right, along with corresponding low magnification images and diffraction patterns of the nanoparticles on the left. A multislice simulation based on the (010) predicted structure is overlaid on the LaScO_3 and shows an excellent match. 78
- 4.10 Predicted structure of the oxygen vacancy containing reconstruction on the (010) surface is shown in (a), with the pDOS in (b). Colors in (a) and (b) are similar to previous figures. 80
- 4.11 The terminating O_4^{8-} layer of GdScO_3 before creating the necessary two O vacancies is shown above. Here, and in the other $(110)_{pc}$ surfaces, the lowest energy configuration comes from removing the two O atoms that are farthest into the vacuum. In the diagram above that is the two rightmost O atoms. Red atoms are O, purple are Gd, and gray are Sc. 81
- 4.12 DFT predicted structures of the (100) and (112) surfaces. Though the polyhedral arrangements look quite different, the coordinating Sc atoms occupy similar sites. The polyhedral coloring convention is the same as in previous figures. 82
- 4.13 Calculated Wulff shapes of GdScO_3 for different values of $\Delta\mu_{\text{Sc}_2\text{O}_3}$. The value of $\Delta\mu_{\text{Sc}_2\text{O}_3}$ is printed under each construction in units of

eV/Sc₂O₃, and the orientation of the constructions is given by the axes on the left. Facets are colored by their pseudocubic designations, with the $\Delta\mu_{\text{Sc}_2\text{O}_3}$ single layer surfaces in green, the $\{100\}_{pc}$ double layer surfaces in blue, and the $\{110\}_{pc}$ single layer surface in red. As no specific calculation was performed for the (001) single layer termination, it was approximated using the energy of the (110) single layer.

84

5.1 The modified Winterbottom construction for a 5-fold multiply twinned particle (MTP) viewed along the [110] direction. Crystallite I is unaffected by the presence of the interface as a result of its orientation. The twin boundary energy is set to zero resulting in the boundaries intersecting with the Wulff center. Crystallites II and III are affected by the interface to form the morphology pictured.

88

5.2 Experimental images of supported 5-fold MTPs with (b) matching the orientation in Figure 5.1. These morphologies represent both possible orientations for a supported nanoparticle with this particular interfacial orientation.

90

5.3 The partial contribution of each crystallite towards the total area is calculated in (a) (note that A_{II} and A_{III} are double counted towards the total area since there are two of each crystallite type). The effective interfacial energy, γ_{eff} , is shown in (b), given the

- assumptions in the text. Overlaid on (b) are the particle heights for each orientation, and the marked intersections are where $\gamma_{eff}(h) = \gamma_h$. 92
- 5.4 ϵ_w plots for each orientation of the 5-fold MTP along with a schematic demonstrating the particles' morphology and truncation height. The minimum values (marked in red) can be compared with the experimental images in Figure 5.2. There is a local minima marked with a green triangle in (b). Also note the direction of the x axis in (b). 93
- 5.5 ϵ_w plots for different MTP geometries are given for a particle with isotropic surface energy (a/b) and with no reentrant surfaces (c/d). Absolute minima are marked in red and local minima with a green triangle. 95
- 5.6 ϵ_w plots for an MTP with adjusted interfacial energies. This results in more significant changes than those seen in Figure 5.5, introducing more local minima and changing the location of the global minimum to a greater degree than changing the external energies. 96
- 5.7 An aberration corrected HREM image of a supported icosahedral MTP of Au on GdScO₃. As highlighted in the image, the particle orients such that the (111) plane is at the interface. 97
- 5.8 Aberration corrected high angle annular dark field (HAADF) images of 5-fold MTPs of Pd on SrTiO₃. The yellow lines indicate the 5-fold axis. These morphologies are indicative of the particle axis tilting

into or out of the plane of the page [4, 5], and by doing so the (111) surface can make contact with the support. Scale bars are 1 nm. Reprinted with permission from [6]. Copyright (2018) American Chemical Society.

98

5.9 Bright field (a) and HAADF (b) of a twinned Au particle supported on NiO with a surface step indicated by the red arrow. The twin boundaries in the Au allow the (111) planes to maintain contact with the surface over the step. Reprinted with permission from [7]. Copyright (2018) American Chemical Society.

98

5.10 A lamellar twinned particle (LTP) of Pt on a rough surface of LaScO₃ is observed on the left, with two single crystal [111] type particles on the right. The twinning of the LTP owing to the surface step results in the (111) surface forming the majority of the interfacial area despite the rough LaScO₃ surface.

99

5.11 Aberration corrected HREM of supported Au nanoparticles showing a single crystal (left) and a MTP (right) at significantly different truncation heights. The Wulff center is marked on the right and the overall Wulff construction is overlaid on the left. The greater relative height of the MTP indicates a smaller adhesion energy, and there is suggestion of kinetic influence in the formation of the particles.

99

6.1 Au deposited on LaScO₃ via deposition precipitation.

103

- 6.2 The different orientations of single crystals observed on the $(100)_{pc}$ support surfaces are pictured above. The support material in (a) and (b) is NdScO_3 , while GdScO_3 is shown in (c). In (a) the particles on the left and right are $[110]$ type particles viewed along the $[100]$ direction and the central particle is a $[111]$ type particle viewed along the $[112]$ direction of the Au. The particles in (b) are $[110]$ type particle viewed along the $[110]$ direction, and the particle in (c) is a $[111]$ type particle viewed along the $[110]$ direction. 105
- 6.3 Proportions of the three major morphologies of Au observed on different LnScO_3 supports. Over 200 particles were counted on each support and error bars show the standard error of the proportion. 106
- 6.4 . Twinned Au supported on LaScO_3 . Many of the particles observed are hemispherical in shape rather than sharply faceted single crystals, and those with facets do not conform to expected single crystalline shapes. 107
- 6.5 A comparison of $[111]$ type au particles on LaScO_3 , NdScO_3 , SmScO_3 , and GdScO_3 (left to right). All particles have a similar degree of truncation as demonstrated by the overlaid Wulff shapes. 109
- 6.6 Au nanoparticles on NdScO_3 (110) pseudocubic surfaces (top) and a rough surface (bottom). No $[110]$ type particles are observed, though some single crystals are seen. A Wulff shape is outlined in the top left figure to demonstrate that, through the particle has a pointed top similar to the particles in Figure 6.2b, it is not a $[110]$ type particle. 112

- 7.1 A comparison between HAADF and moderate angle annular dark field (MAADF) imaging of Au on GdScO₃. 116
- 7.2 temperature programmed desorption with mass spectrometry (TPD-MS) results from the bare supports are shown in (a). The signal is normalized to the total integrated CO₂ desorption and is divided at 500 °C between low and high temperature regimes. Moles desorbed per m² of each sample are reported in (b). NdScO₃ both bonds CO₂ more strongly than the other supports and has the most CO₂ per m². 118
- 7.3 Average sizes of the as deposited (blue) and post-catalysis (orange) Au nanoparticles. As seen in the LaScO₃ and SmScO₃ data, very low loadings experienced runaway sintering. 120
- 7.4 Apparent activation energies for CO oxidation with the different support materials at each weight loading is given in (a) with error bars calculated from a linear least squares fit of the Arrhenius plots in (c). TOF data for each sample at 200 °C, along with error bars calculated from the particle size standard deviations are shown in (b). 122
- 7.5 Density of states of the LnScO₃ materials used in the catalytic experiments. Black lines represent the total DOS, red the Ln 4f, and blue the O 2p. As seen, the O₂p states sit at the valence band edge for all the materials. The 4f electrons of NdScO₃ are also at the valence band edge, indicating chemical activity, while in LaScO₃ (a), there are no 4f electrons and in SmScO₃ (c) they sit at deeper energies. 124

- 7.6 Proposed E-R reaction mechanism for CO oxidation over the Au/LnScO₃ catalyst materials. CO adsorbs to the Au nanoparticle in (A) then forms the intermediate O¹CO²O³ species in (B) following the adsorption of O₂. From here the intermediate can either decompose to (C) before CO₂ desorption or move directly to (D). In either case, the lowered energy of (B) on NdScO₃ due to the 4f inductive effect increases the energy barrier. The remaining O₃ at the interface readily reacts with gaseous CO to form CO₂ and refresh the catalyst active site in (E). 126
- 7.7 Preliminary results of CO oxidation over Pt/LnScO₃. In contrast to Au/LnScO₃, the energy barrier is smallest when the support material is NdScO₃. 127
- 8.1 Images of [110] type Pt particles on LaScO₃ (100)_{pc} surfaces. 130
- 8.2 Profile views of the (110) and (001) GdScO₃ surfaces in (a) and (b) respectively, with a profile view of the (110) surface of Pt shown in (c) viewed along the [1 $\bar{1}$ 0] direction. 132
- 8.3 Power spectrum of Figure 6.2b, which includes Au and GdScO₃ along [110] zone axes. Overlapping reciprocal lattice points are outlined in red, demonstrating the coincident nature of the two orientations. 133
- 8.4 The initial structural model for the (110) interface is shown in (a) and (b), along with the final, DFT relaxed structure in (c) and (d). The

- Pt and GdScO_3 directions are given by the axes to the right of each model. 134
- 8.5 Arrangement of the first layer of Pt atoms at the interface is shown in (a), along with the Bader charges overlaid on each atom. The average Bader charges at the topmost and an inner layer of the Pt are given in (b) and are close to zero as expected. 135
- 8.6 Comparison of the interfacial (bold lines) and bulk (thin lines) O 2p (red) and Sc 3d (blue) pDOS of GdScO_3 . Positive values are spin up and negative are spin down. 136
- 8.7 pDOS of the positive (red) and negative (blue) Pt atoms at the GdScO_3 interface compared to the pDOS of Pt from a separate, bulk calculation. 137
- 9.1 Schematic of the differential phase contrast (DPC) method and application to measure polarization of BaTiO_3 (a). Considering the detector geometry in (b), the direction and magnitude of the beam deflection can be measured via the difference in signal between opposing detector segments, as in (c) and (d). Explicitly, where (W-Y) is bright in Figure (d), the beam has deflected towards segment W. Figure reproduced by permission from Springer Nature, Nature Physics [8], Copyright 2012. 141
- 9.2 HREM Pt supported on SrTiO_3 and $(\text{Ba,Sr})\text{TiO}_3$ is shown in (a). The strain mismatch is greater on $(\text{Ba,Sr})\text{TiO}_3$, and the Pt particles have

a greater adhesion energy demonstrated by the decreased adhesion. Diffuse reflective infrared Fourier transform spectroscopy (DRIFTS) of CO on Pt/LnScO₃ is reported in (b). The signal above 2000 cm⁻¹ is associated with linearly bound CO, and the signal near 1800 cm⁻¹ with bridged CO [9,10]. The relative population of bridged compared to linearly bound CO (calculated via integrating the peak areas) as a function of strain mismatch is inset, though adding more datapoints is necessary to begin drawing conclusions related to trends in this behavior. (a) is reproduced by permission from Springer Nature, Topics in Catalysis [11], Copyright 2013.

143

- C.1 Surface density of Au nanoparticles both as deposited (left) and after catalytic testing (right). 168
- C.2 Au size distribution after catalytic testing on LaScO₃ with a loading of 0.45 mole %. Due to the runaway sintering in some of the particles, a bimodal distribution develops. 169
- D.1 TOF data from the samples at all measured temperatures using the particle sizes measured after catalysis. Error bars are calculated using the particle standard deviations. 171
- D.2 TOF data from the samples at all measured temperatures using the particle sizes measured before catalysis. As noted in the main text of Chapter 7, the particle sizes measured after catalysis are more representative of the experimental conditions, but these are reported

here for completeness and show no unexpected or unrealistic results.

Error bars are calculated using the particle standard deviations. 172

E.1

Layer resolved DOS of the interfacial layers of GdScO₃ and Pt near E_f . In both cases, red represents the layer at the interface, blue is the next nearest, and black is the third layer. As seen, the MIGS largely disappear after the first atomic layer of GdScO₃, and the Pt is mostly unaffected, though some differences exist at the interfacial layer. In the GdScO₃ DOS, the occupied regions are both O 2p and appear similar, while the unoccupied regions are Sc 3d in Subsurface 1 and Gd 4f in Subsurface 2. Positive values are spin up while negative are spin down. 173

CHAPTER 1

Introduction

1.1. Motivation

As global energy consumption continues to rise amid grim outlooks for the future of the environment, the need to increase the efficiency of industrial chemical reactions and reduce emissions has never been more urgent. One of the many ways to begin addressing this problem is the design and development of more efficient catalysts. Catalysts are materials that promote chemical reactions by providing an alternate reaction pathway with smaller energy barriers, and catalysis plays a significant role in many aspects of society. It is estimated that 80-90 % of products made in chemical industry utilize catalytic processes in their production [12].

Many types of catalysts exist, and this thesis focuses on supported metal nanoparticles [13–15], which are small metal nanoparticles (diameters typically under 5 nm) on substrates as in Figure 1.1. Chemical reactions catalyzed by metal particles occur at the surface of the metal, and utilizing nanoparticles rather than large crystals increases the surface area to volume ratio of the metal, providing more potential reaction sites for a given amount of catalyst. Furthermore, some metals such as Au that are largely inert at larger crystal sizes have been found to be catalytically active as nanoparticles [16]. Unfortunately, freestanding nanoparticles are prone to sintering together, reducing the

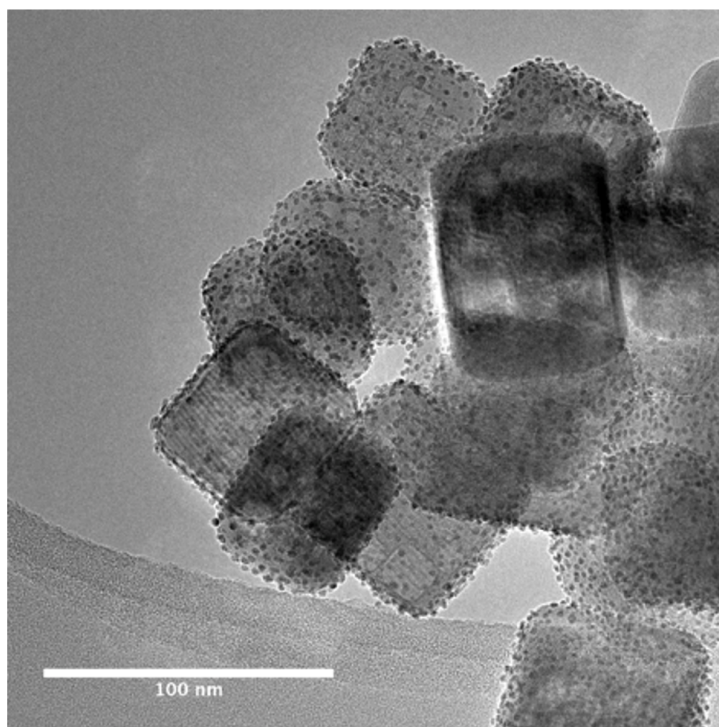


Figure 1.1. Pt nanoparticles supported on SrTiO₃ nanocuboids prepared via ALD.

surface area to volume ratio, and as a result the catalyst nanoparticles are often dispersed on substrates to stabilize them in reaction conditions.

A catalytic reaction over a supported metal nanoparticle will follow this general path: reactants adsorb on the catalyst surface (either on the surface of the metal, the support, or at the interface), react to form the product, then desorb leaving the active site on the catalyst open for the next reaction. The support material, while sometimes viewed as a spectator only present to prevent sintering, can significantly affect the reaction [17, 18] and finding the optimal pairing of a metal and support material will lead to the best catalyst system for a given chemical reaction. In pursuit of this goal, researchers are trying to move away from the historical method of trial-and-error, and rather look to

rationally design new, more efficient catalysts using knowledge of material science and catalytic theory.

A common method to study support effects in catalysis is, for a given metal and chemical reaction (e.g. CO oxidation using Au nanoparticles), to select a variety of commonly used support materials such as titania, zirconia, and alumina and test each catalyst system's performance in reaction. Metrics such as the activation barriers and selectivity towards different products are measured and conclusions are drawn linking the performance of these catalysts to various changing support properties; however, when comparing different supports a significant number of chemical and physical properties can be different. These include, but are not limited to: chemical composition, band gap, lattice mismatch, and adsorbate binding behavior. Consequently, it is often very difficult to determine exactly which of the many variable properties is the most significant, and therefore difficult to form predictive theories for the design of new, optimized catalysts.

This is further complicated by the surface of the material, it is well known that the surface structure and chemistry of an oxide material can be different than the bulk. When considering catalytic reactions with oxide supported nanoparticles, knowledge of the chemistry and structure of the support surface is vital towards understanding both the behavior of the support in reaction [18–20] as well as the interaction with the metal with the surface of the support [18, 21–24]. While both experimental and theoretical surface studies are commonplace for well-defined single crystals, they do not adequately describe the surface structures and properties of many nanoparticle supports used in catalysis, which are often rough and poorly defined. This disconnect between highly controlled

single crystal studies and high surface area nanoparticles is commonly referred to as the “materials gap”.

This thesis focuses on using a series of support materials deliberately synthesized to minimize this gap in understanding, with the goal of identifying the key support material properties that affect catalytic performance. By identifying which of the many variable properties of the support matter most towards facilitating efficient catalytic reactions, predictive theories towards designing future catalysts can be formed and applied.

1.2. Faceted Lanthanide Scandate Supports

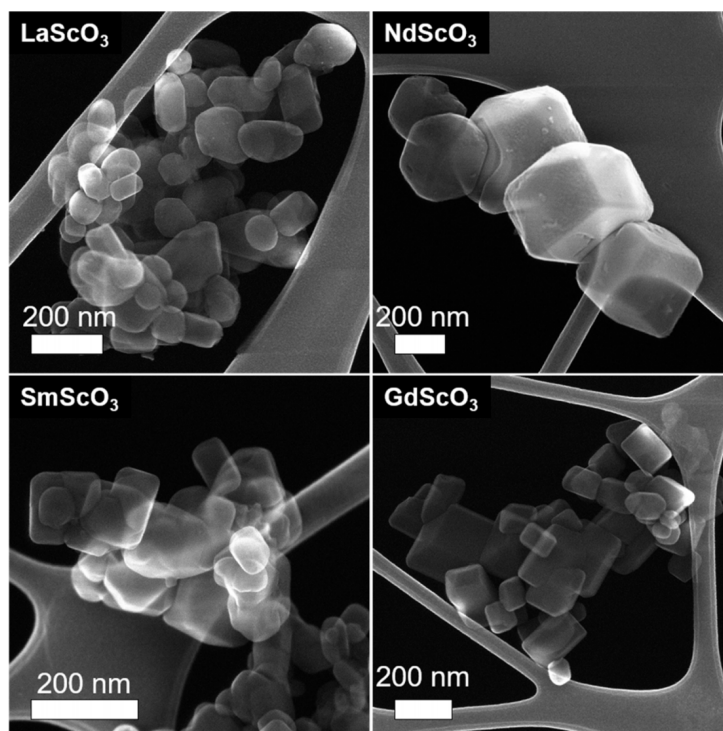


Figure 1.2. Secondary electron images of different LnScO_3 supports demonstrating a faceted, cuboidal morphology.

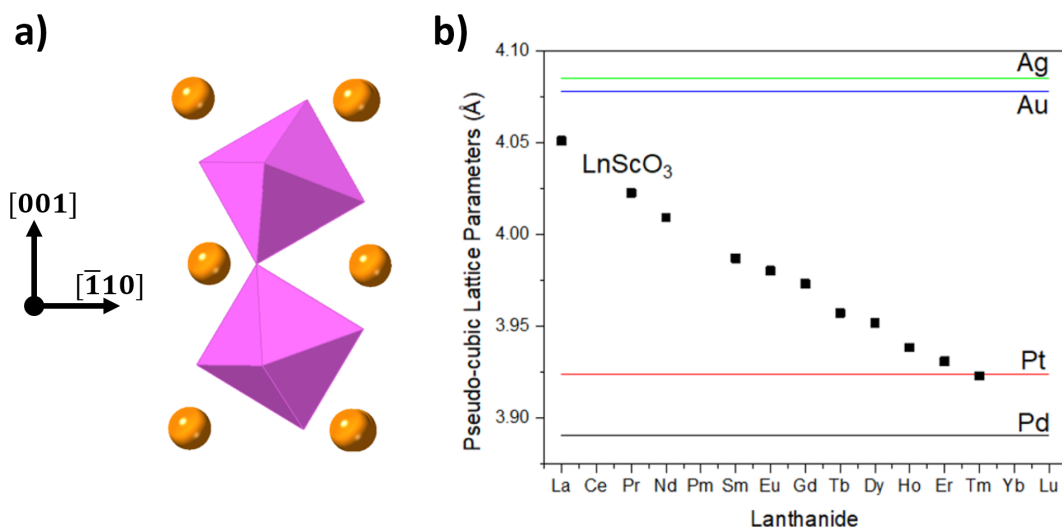


Figure 1.3. . The structure of a typical LnScO_3 material (NdScO_3) is given in (a) viewed down the $[110]$ axis. Pink octahedra are ScO_6 units and the orange atoms are Nd. There are two pseudocubic units per unit cell, stacked in the $[001]$ direction. Pseudocubic lattice parameters are given in (b) along with lattice parameters of the noble metals Ag, Au, Pt, and Pd.

In order to both (1) minimize the number of variable properties between different support materials and (2) bridge the materials gap between controlled single crystals and high surface area nanoparticles, a series of lanthanide scandate nanoparticles (LnScO_3 , Ln = La, Nd, Sm, Gd) were synthesized by collaborators (R. J. Paull and E. P. Greenstein) with a faceted geometry as depicted in Figure 1.2 [25, 26]. These materials are distorted orthorhombic perovskites with the $Pbnm$ structure consisting of two pseudocubic units stacked in the $\langle 001 \rangle$ direction, which are visible when viewed along the $\langle 110 \rangle$ direction as in Figure 1.3a (it is often convenient to refer to the pseudocubic reference frame, and pseudocubic units will be written as $(hkl)_{pc}$ herein). As synthesized, they form cuboidal shapes principally exposing the $\{100\}_{pc}$ surfaces, with facets of the $\{110\}_{pc}$ type forming at the edges. The LnScO_3 materials have pseudocubic lattice parameters close to

many catalytically relevant noble metals (Figure 1.3b) and, as described in later chapters, similar structures and chemistries at the surface. By reducing the number of changing properties between the studied support materials and forming well defined surfaces on the nanoparticles, the faceted LnScO_3 supports allow for controlled studies of support effects in catalysis.

1.3. Organization

This thesis, “Identifying Support Effects in Nanoparticle Catalysis”, is organized into 9 chapters. Chapter 2 provides an overview of the experimental and theoretical methods used to study the catalyst materials throughout the following chapters. In Chapter 3, single crystal (110) surfaces of GdScO_3 , TbScO_3 and DyScO_3 are studied and a double layer, scandium rich surface reconstruction is solved. In Chapter 4, similar scandium rich, double layer reconstructions are identified on a majority of the exposed $\{100\}_{pc}$ surface area of the prepared LnScO_3 nanoparticle supports. Additionally, Chapter 4 contains the structures of the $\{110\}_{pc}$ surfaces and a single layer termination which is found on a small (approx. 10%) area of the $\{100\}_{pc}$ surfaces. Calculated energies from these surfaces, as well as their chemistries, are then used to generate theoretical, thermodynamic Wulff constructions [27–29] of the LnScO_3 materials.

Metal nanoparticles are desposited on the surfaces of the LnScO_3 materials for the purpose of catalytic testing, and many form MTP geometries [30]. To fully understand the thermodynamics of supported MTPs a modified Winterbottom construction [31] is derived in Chapter 5. Chapter 6 describes the deposition of Au nanoparticles on the

LnScO_3 supports and discusses the various morphologies, orientations, and thermodynamics of the Au. Chapter 7 contains results of CO oxidation experiments using Au supported on LnScO_3 coupled with desorption experiments and DFT investigation of the bare support materials. Here, changes in the surface basicity owing to a 4f inductive effect are identified as the driver of varied catalytic performance between the materials. In Chapter 8, the (110) type interface formed between the noble metal nanoparticles and support surfaces is modeled and discussed. Lastly, Chapter 9 is used to suggest areas and directions for future research on these materials and their use in catalysis.

CHAPTER 2

Experimental and Theoretical Methods**2.1. Transmission Electron Microscopy**

Transmission electron microscopy (TEM) is a versatile characterization technique for gaining structural and chemical information from a sample and is the principal experimental technique used throughout this thesis. In addition to conventional imaging techniques which can reveal details on length scales from microns to nanometers, aberration correction and image processing have allowed for sub-Ångstrom resolution with a current “resolution record” of 0.39 Å achieved at Cornell University [32]. Beyond imaging, diffraction patterns containing crystallographic data can be collected and spectroscopy of X-rays and inelastically scattered post-specimen electrons allows for chemical and electronic fingerprinting of a sample. Here the basics of the electron beam’s interaction with the specimen will be described along with overviews of the relevant techniques used in this thesis, and further detail is found in the references [1, 33–36].

2.1.1. Electron Specimen Interaction and S/TEM Basics

There are two major ways to operate a TEM: (1) with parallel beam illumination where the electron beam is spread over the relevant area of the sample or (2) by scanning a focused probe across the image area and sequentially collecting the signal generated at each point. Regardless of the beam geometry, when a high energy electron beam interacts

with a sample (that is thin enough to allow transmission), many different signals are generated which are outlined in Figure 2.1. Each of these signals is important and can be utilized.

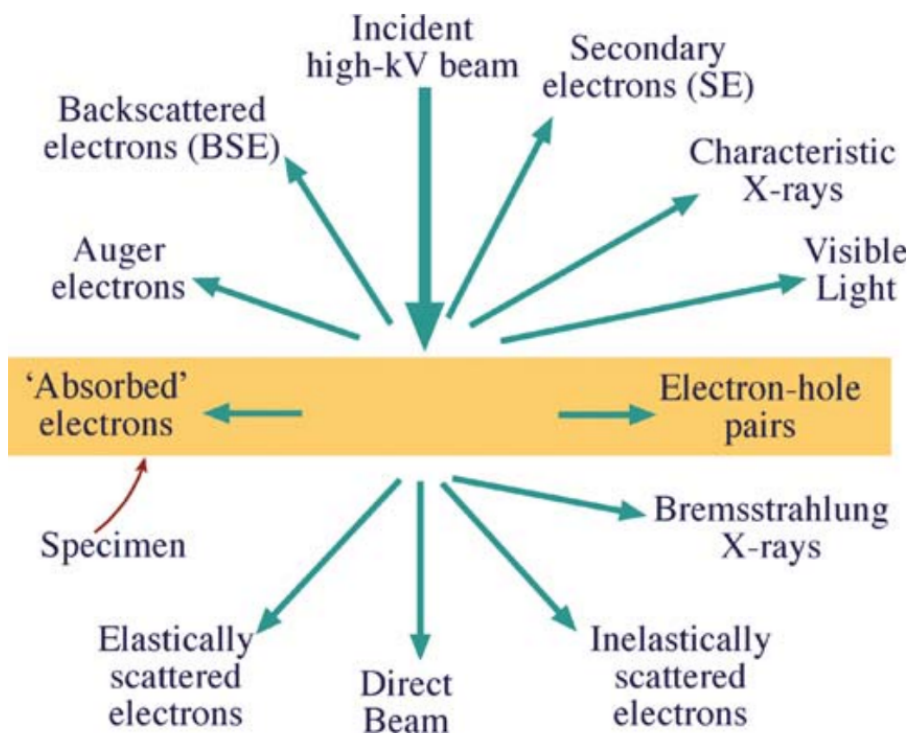


Figure 2.1. Schematic representation of the interaction between an electron beam and a specimen with the resulting signals that are generated. Figure adapted from [1].

First considering parallel beam illumination, images are formed in parallel where signal at all points of the detector is acquired simultaneously over a certain amount of time. When using electrons from the direct beam, which primarily consists of transmitted electrons that have not been diffracted along with some that have been dynamically scattered back to the central diffraction spot, a bright field image is formed. Using the elastically scattered electrons that do not dynamically scatter back to the origin will give dark field

images, and an objective aperture is used to select which these electrons are included in a particular image. At lower magnification, image contrast is determined by the amplitude of the electron beam, and that amplitude is affected both by diffraction and by the mass/thickness of the sample. At higher magnification, with a degree of coherent illumination, one can generate phase contrast images which will be discussed in the next section. Viewing the diffracted electrons in reciprocal space at the back focal plane gives a diffraction pattern, which contains crystallographic information about the sample.

In contrast to parallel illumination, image formation in scanning transmission electron microscopy (STEM) is a serial technique. The transmitted beam is collected by a detector centered under the beam to form bright field images and/or the diffracted beams are collected with an annular detector centered *around* the transmitted beam in a technique known as annular dark field (ADF) as the probe scans across the sample. The signal in each detector is then binned and correlated to the probe position at the time of acquisition in a sequential fashion. Additionally, incoherently scattered electrons can be collected from high angles by a wider annular detector (or by changing the effective distance from the sample to the detector known as the camera length) to form HAADF images which have easily interpretable mass/thickness contrast.

Inelastic collisions between the electron beam and sample are also useful where the resulting characteristic X-rays and inelastically scattered electrons can be collected as energy dispersive x-ray spectroscopy (EDX) or electron energy loss spectroscopy (EELS) respectively. EDX signals are dependent on the chemical composition of the material and are used to identify and quantify the elements present in a sample. EELS signals also contain this information, as well as information about the physical and electronic

structure of the sample. (EELS is not featured in this thesis work so further discussion is not warranted here, however EELS spectra contain a plethora of information that can be used to analyze a material [1]). In parallel beam illumination the spectroscopic signals are not localized to any one point due to the size of the beam interaction with the sample, but owing to the serial nature and small probe size of STEM these signals can be correlated to the beam's position at a given time and used to generate spatially resolved spectroscopic information.

2.1.2. High Resolution Electron Microscopy (HREM), Aberration Correction, and Image Simulation

HREM is found in most chapters of this thesis and allows for the indirect visualization of atomic planes or columns. In contrast to HAADF, where contrast in atomic resolution images is readily interpretable (imaging a single atomic column in HAADF will give signal at the spatial coordinate directly corresponding to that column and will be proportional to the mass/thickness of that column), HREM contrast is formed “indirectly” where contrast is due to interference between the different diffracted beams. In HREM, the phase of the electrons is affected by channeling along atomic columns and by distortions from imperfections in the electromagnetic lenses. These phase changes result in interference and therefore contrast in the image plane. Of course, this is a dramatic oversimplification of phase contrast in the TEM and more specific details including channeling, contrast transfer theory, dynamical diffraction, and the weak phase object approximation can be found in many published texts [33–36].

Electromagnetic lenses in the TEM are far from perfect and generate aberrations that limit the attainable resolution of a microscope. To combat this and increase the resolution limit of the TEM, aberration correctors were developed to correct for both the spherical and chromatic aberrations in the lenses, and schematics of these aberrations can be seen in Figure 2.2. The first aberration corrected TEM images were published in 1998 [37], though this date is largely linked to advancements in computational technology rather than theory. Aberrations in the TEM were identified as early as 1936 by Otto Scherzer [38], who also proposed they could be corrected 1949 [39]. The first prototypical correctors were developed in the mid 20th century [40]; however, manual alignment of the numerous multipole lenses without computation was an insurmountable hurdle. The aberration corrected imaging in this thesis was carried out using the Argonne Chromatic Aberration-corrected TEM (ACAT), which is a FEI Titan 80-300 with a combined chromatic and spherical aberration image corrector.

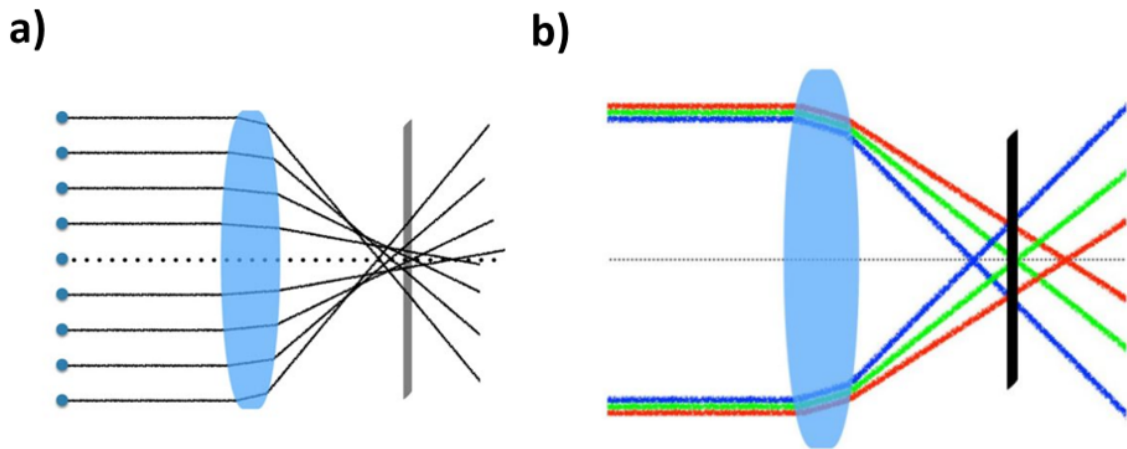


Figure 2.2. Spherical (a) and chromatic (b) lens aberrations. A spherical aberration more heavily focuses waves far from the center of the lens, and a chromatic aberration more heavily focuses waves of a higher energy. Figure adapted from [2].

As mentioned, specific features HREM images cannot be directly interpreted as structural features of the sample as they are closer to interference patterns than direct images, and the contrast generated by an atomic column is a function of microscope, sample, and imaging conditions. This difficulty of interpretation is demonstrated in Figure 2.3a, a HREM image of a SmScO_3 particle with a thickness gradient. Despite no changes to the intrinsic crystal structure or symmetry, the contrast changes significantly moving across the image. As a result, HREM is often paired with image simulation for comprehensive understanding of an image. The electron in the TEM column, its interaction with the sample, and the aberrations introduced by the electromagnetic lenses can be described quantum mechanically and, given proper input parameters concerning the specific sample and microscope, HREM images can be calculated.

One of the most common methods of HREM image simulation is the multislice method [41], where the material is modeled in finite slices that act as phase gratings. An electron beam with a wavelength of λ is stepped through the model material, first by transmitting the electron wavefunction, $\phi(x, y, z)$, through the phase grating using a transmission function, $t(x, y, z)$, dependent on the crystal potential, $V(x, y, z)$ in a slice of with thickness Δz

$$(2.1) \quad t(x, y, z) = \exp(i\phi \int_z^{z+\Delta z} V(x, y, z') dz)$$

with σ being an interaction constant dependent on the electron accelerating voltage. The beam is then moved forward to the next slice with a propagation function. This can be approximated as a Fresnel Propagator, as in Equation 2.2, but is more rigorously

described using the Green's function in Equation 2.3.

$$(2.2) \quad p(x, y, \Delta z) = \frac{1}{i\lambda\Delta z} \exp\left(\frac{i\pi}{\lambda\Delta z}(x^2 + y^2)\right)$$

$$(2.3) \quad G(\vec{r} - \vec{r}') = \frac{\exp(2\pi ik(z - z'))}{4\pi(z - z')} \exp\left(\frac{-i\pi k(x - x')^2 + (y - y')^2}{z - z'}\right)$$

These equations form the basis of multislice imaging theory given mathematically in Equation 2.4 as a convolution and Equation 2.5 in terms of Fourier Transforms (which are easily handled by computers) and the multislice simulation process is pictured schematically in Figure 2.3b.

$$(2.4) \quad \phi(x, y, z + \Delta z) = p(x, y, \Delta z) * (t(x, y, z)\phi(x, y, z))$$

$$(2.5) \quad \phi(x, y, z + \Delta z) = \mathcal{F}^{-1}[P(k_x, k_y, \Delta k_z)\mathcal{F}(t(x, y, z)\phi(x, y, z))]$$

The previously mentioned input parameters regarding the instrumentation and aberrations are not explicitly present in these equations as presented, rather are folded into the electron wavefunction in the form of an aberration function $\chi(\vec{k})$. For a more rigorous description, please see the references [33–36, 41]. All multislice simulations in this thesis were performed using the software package MacTempasX.

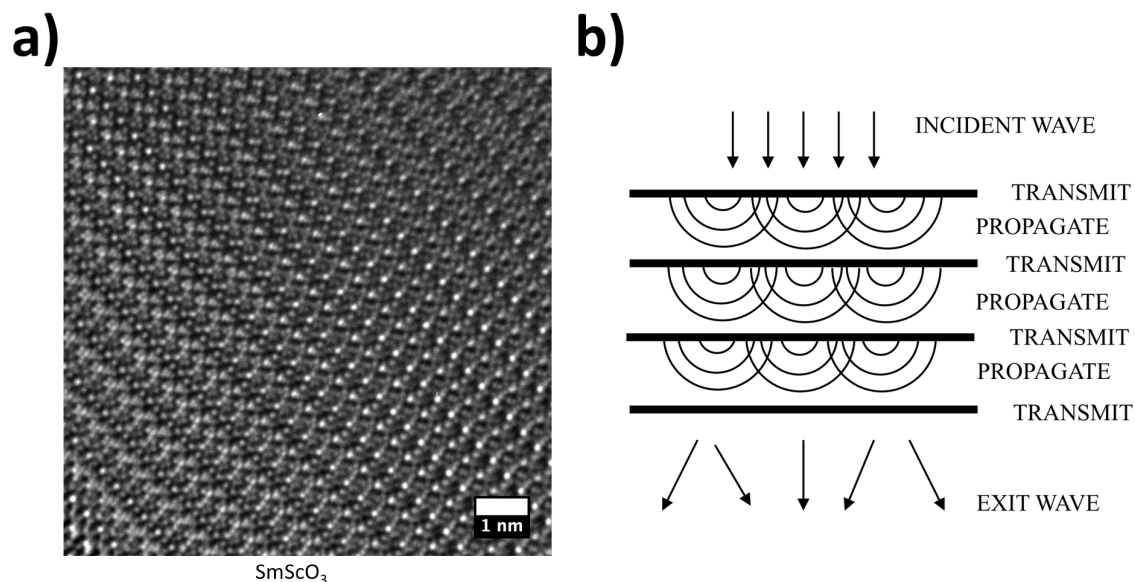


Figure 2.3. The HREM image of SmScO_3 in (a) demonstrates the variation in contrast as a function of sample thickness despite no changes to the crystal structure, exemplifying the difficulty of directly interpreting HREM images. The general process for multislice simulation is seen in (b), which is reproduced from [3].

2.1.3. Beam Dose and Sample Cleaning

The materials studied in this thesis had two major, specific experimental considerations that were necessary to ensure the data obtained via TEM was representative of the samples prior to measurement. The first of these is the beam dose when viewing small Au particles. These nanoparticles are quite sensitive to the beam, where their shape and size (due to agglomeration) are affected by high electron doses. To prevent this from occurring, the beam dose was reduced to the point where the nanoparticles appeared static under the beam, then the beam was moved to a new area of the sample for imaging to ensure no morphological changes occurred as a result of the beam interaction. This instability can be seen in Figure 2.4.

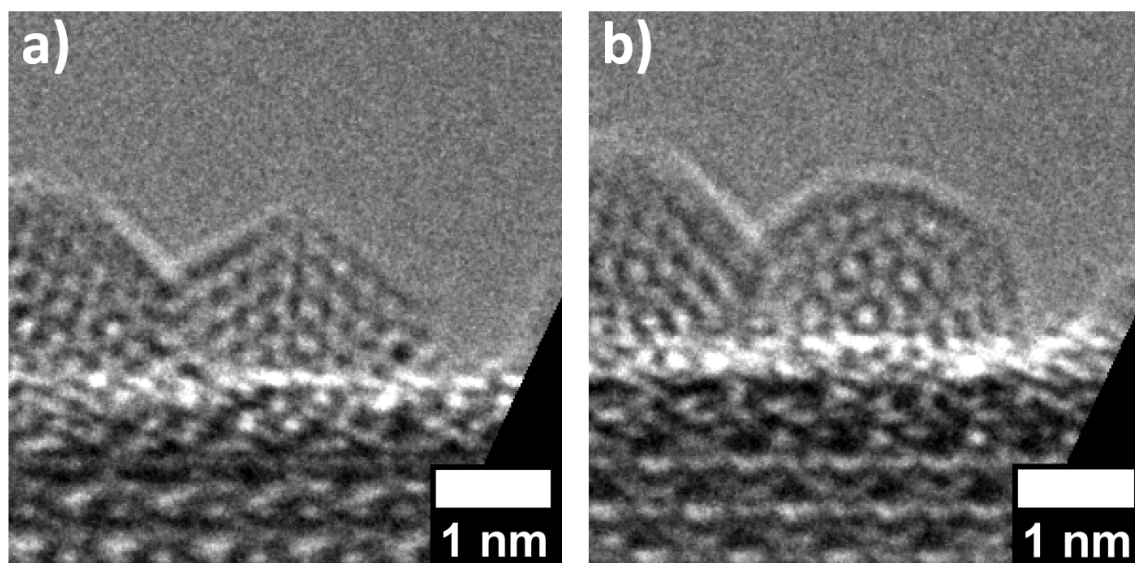


Figure 2.4. A gold nanoparticle changing shape under the electron beam over time due to electron beam irradiation.

This particle instability also needed to be accounted for in the selection of sample cleaning techniques, the second major consideration. Catalyst samples (and TEM samples in general that have been exposed to the air) often have adsorbates and hydrocarbons on the surface, which can contaminate the sample and lead to carbon buildup under the beam. As a result, they must be carefully cleaned in a fashion that removes the contaminants while maintaining the original structure of the sample in order to obtain high quality, clean images. The samples in this work used to determine the size and morphology of the Au were cleaned using an ozone cleaner, as other techniques such as low temperature vacuum heating or plasma cleaning resulted in unacceptable particle sintering.

2.2. Density Functional Theory

Electrons and atoms are accurately described quantum mechanically using the Schrödinger Equation, which has the time-dependent form:

$$(2.6) \quad i\hbar \frac{\partial}{\partial t} \phi(\vec{r}, t) = \hat{H} \phi(\vec{r}, t)$$

Where \hbar is the reduced Planck constant, $\phi(\vec{r}, t)$ is the time-dependent wavefunction, and \hat{H} is the Hamiltonian that defines the total energy of that wavefunction and includes kinetic energy, interaction between electrons and the nucleus, and electron-electron interaction. This represents a many-body problem that scales as N^3 for a N -electron system, making an analytical solution for a real material system unfeasible.

This challenge was circumvented by Hohenberg and Kohn’s theorem that the ground state energy of a system can be uniquely obtained from the system’s electron density [42], reducing this many body Schrödinger Equation to multiple, single-body equations that can be computationally solved [43]. Even so, solving the exchange and correlation terms between electrons is a challenge, and a number of functionals have been developed to attempt to approximate them, though they are imperfect. For some materials, particularly transition metals and the lanthanide scandates studied herein, the accuracy of these calculations can be improved by including a fraction of the exact exchange calculated in this work using the ”exact exchange for correlated electrons” (EECE) method [44, 45], referred to herein as a hybrid fraction.

The DFT calculations in this work were done using WIEN2k, an all-electron augmented plane wave + local orbitals code [46]. This package treats the orbitals inside of a defined “muffin tin” radius as spherical harmonics, and those outside of the radius as plane

waves, with appropriate boundary condition matching at the muffin tin edges. The functional used throughout is PBEsol [47], a revised version of the Perdew-Burke-Ernzerhof (PBE) functional [48] for solids and surfaces.

DFT is applied in two major ways throughout this work: to determine exact atomic positions of surface reconstructions and to calculate electronic structure details of the lanthanide scandate materials. The lanthanide scandate materials are electronically complex, and previous work has demonstrated that careful selection of hybrid fractions (Ln 4f: 0.38, Ln 5d: 0.50, Sc 3d: 0.80) and muffin tin radii (Ln: 2.02, Sc: 1.82, O: 1.68) are necessary for accurate calculation of their energies and properties [49]. These values minimize the forces on the atoms using known bulk positions from experimental data [50].

2.3. X-ray Photoelectron Spectroscopy

XPS is a technique in which a sample surface is bombarded by X-rays and electrons generated via the photoelectron effect are collected and energetically fingerprinted using a hemispherical detector. When an electron is ejected by an incident X-ray with energy $h\nu$, the kinetic energy of the electron is equal to:

$$(2.7) \quad KE = h\nu - BE - V_c$$

Where BE is the binding energy of the electron and V_c is the potential in the sample that may be present due to charging in insulators. These photoelectrons have specific binding energies depending on their origin and can be used to gain information about a sample's composition and the valence state of the atoms. In insulators that charge and have a

non-zero V_c , known binding energies of certain species such as the carbon 1s signal at 285 eV are used to charge-correct the overall spectra.

The inelastic mean free path of the escaping photoelectrons is rather short, generally under 10 nanometers or smaller for most laboratory X-ray sources, making this a surface sensitive technique. Of particular use is the relationship between the escape angle of the photoelectrons and their intensity. As the trajectory of the photoelectrons angles away from the surface normal, the effective escape depth is decreased and the signal intensity from a depth normal to the surface d is attenuated as in Equation 2.8, where λ is the inelastic mean free path of the electron, and θ is the angle measured away from the surface normal:

$$(2.8) \quad I = I_0 \exp\left(-\frac{d}{\lambda \cos(\theta)}\right)$$

By changing the angle of the sample normal with respect to the detector, this relationship can be leveraged to adjust the surface sensitivity of the measurement. At high angles, only photoelectrons generated very close to the surface will escape towards the detector. This technique, known as angle-resolved XPS, is used in Chapter 3 to approximate the surface chemistry of LnScO_3 single crystals.

2.4. ICP-MS/OES

Inductively coupled plasma mass spectrometry/optical emission spectroscopy (ICP-MS/OES), is a method to gain precise information about the concentration of metal ions in solution. In this work, ICP-MS/OES is used to determine the weight loading of Au on the LnScO_3 supports. After digesting the solid catalyst samples in either HF or

HCl, the resulting solution is ignited by a plasma and either the characteristic optical emissions or masses of the resulting ions are measured. To determine the exact quantities of the relevant species, these signals are then compared to prepared standards of known concentration. In this thesis the metal weight loadings on the LnScO_3 supports are determined by taking the ratio of Au to Sc.

CHAPTER 3

Surfaces of (110) LnScO₃ (Ln = Gd, Tb, Dy) Single Crystals**3.1. Introduction**

Schlier and Farnsworth observed diffraction peaks indicating a Si surface lattice 7 times larger than the bulk unit cell over 60 years ago using the relatively new technique of low energy electron diffraction – the first observation of the now famous (7x7) reconstruction of the Si (111) surface [51, 52]. Surface reconstructions have since been identified on crystalline materials ranging from pure metals [53–56], to semiconductors [57, 58], to oxides [19, 59–64], and these reconstructions can be quite different than the bulk of the material. Surface reconstructions can have both structural and chemical differences from the bulk with unique properties that dictate the behavior of that surface. Despite this established research, oxide surfaces are often modeled as simple bulk truncations, or bulk truncations with a few oxygen vacancies, without evidence to support these assumptions.

Chemical reactions in heterogeneous catalysis occur at a material’s surface, and precise knowledge of the surface is necessary when attempting to identify the chemistry of active sites. Assuming a bulk truncation for the LnScO₃ support materials would be naïve when trying to unravel structure-property-performance relationships in catalytic testing, especially since other well studied perovskite materials such as SrTiO₃ [59] (and references therein), LaAlO₃ [62, 63], and KTaO₃ [65] are known to either form surface reconstructions or entirely different surface phases. Furthermore, the lack of a valence neutral bulk

termination (discussed later) for the LnScO_3 surface indicates that some reconstruction is necessary [66].

As a first step towards understanding the surfaces of the LnScO_3 nanoparticles, surface studies of commercially available, (110) oriented single crystals of GdScO_3 , TbScO_3 , and DyScO_3 were performed to identify any surface reconstructions or chemical differences from the bulk. As mentioned in Chapter 1, this surface is one of the pseudocubic $\{100\}$ surfaces ($\{100\}_{pc}$) and represents a significant portion of the exposed surface area of the synthesized LnScO_3 nanoparticles used in subsequent chapters. While it is not necessary for single crystals and nanoparticles to share a surface termination, single crystal studies yield useful insights and provide a starting point for considering surface reconstructions on nanoparticles, which are not suitable for experimental techniques such as angle-resolved XPS of a single surface. While this thesis is framed around applications in nanoparticle catalysis, this is not the only reason to study the surfaces of these materials - lanthanide scandate single crystals are widely used as thin film growth substrates [67–70], and changes to the substrate surface structure and chemistry are known to affect film growth [20, 22, 71, 72].

3.2. Methods

A combination of experimental and theoretical techniques were used to solve the reconstruction on the (110) surfaces of LnScO_3 ($\text{Ln} = \text{Gd}, \text{Tb}, \text{Dy}$) single crystals; the technical specifics of these techniques were discussed in Chapter 2. Specific calculations in this chapter were done using a RKmax (which is the product of the smallest atomic sphere radius, 1.68 here, and the largest K-vector) of 6.0, a 1 x 4 x 4 k-point mesh, and

slabs with 92 unique atoms and P121/m1 symmetry. Approximately 14 Å of vacuum separated the slab surfaces, and slab lattice parameters were 70.3 x 8.0 x 8.0 Å .

The surface reconstructions herein are solved using a three step process:

- (1) Establish constraints on the potential surface reconstructions using experimental data and chemical theory
- (2) Use those constraints to generate potential models for the reconstruction that are assessed using DFT
- (3) Compare the predicted solution to experimental to ensure agreement

While it is possible to avoid the first step and move straight to the generation of surface models, the number of potential structures would be staggering when considering variations to chemistry, periodicity, and structure with no external information. By using electron diffraction and angle-resolved XPS of the single crystal samples to determine the surface chemistry and periodicity, that number is significantly reduced. Furthermore, in a system that lacks valence neutral layers in the [110] direction (discussed in Section 3.5), there exist rather strict constraints on the potential chemistries at the surface and assessing these structures with DFT becomes a manageable endeavor.

To prepare the single crystal samples for study in XPS and electron diffraction, [110] oriented single crystals of GdScO₃, TbScO₃, and DyScO₃ were obtained from the MTI Corporation. 3 mm discs were extracted from the crystals and thinned with SiC sandpaper to approximately 120 μm, then dimpled using a Gatan 656 Dimple Grinder until 20 μm thick at the center. The dimpled samples were then thinned using ion-beam milling in a Gatan Precision Ion Polishing System operated between 2.5 and 5.5 keV until electron transparent. Ion beam thinning introduces disorder at the surface, so the samples were

then annealed at 1050 °C in air for 12 hours to reorder the surface. The annealing step was carried out immediately before characterization experiments to minimize surface contamination from the environment. After XPS, AFM experiments were performed on the samples using a Bruker FastScan AFM operated in tapping mode. XPS and AFM measurements were carried out with assistance from C. A. Mizzi.

3.3. Experimental Results

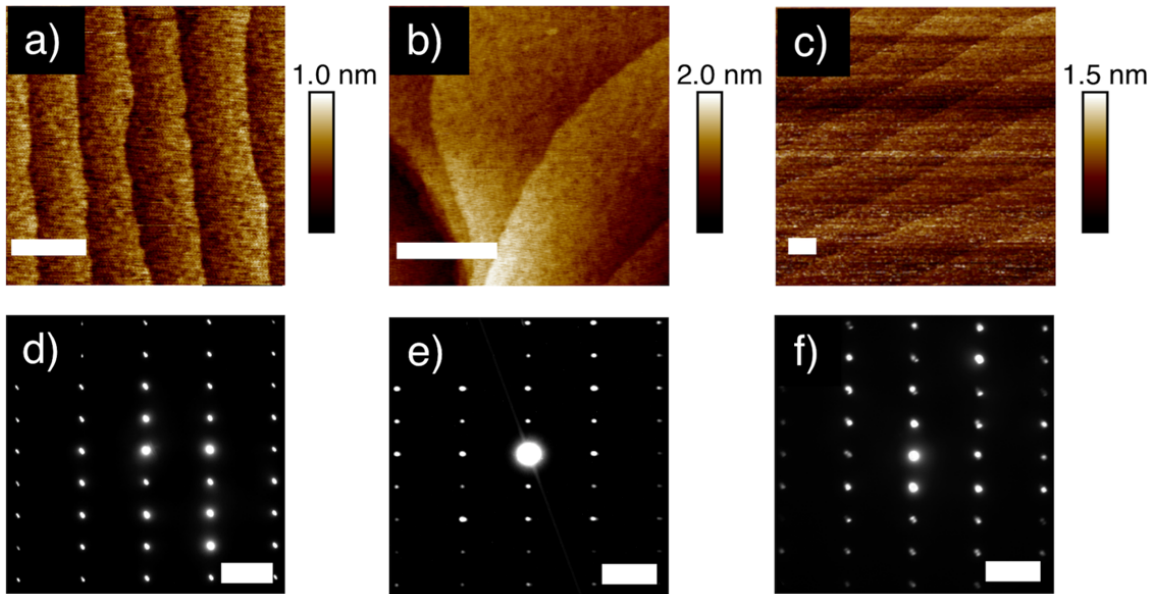


Figure 3.1. AFM (a-c) and surface sensitive electron diffraction (d-f) of the studied LnScO_3 materials. GdScO_3 (a,d), TbScO_3 (b,e), and DyScO_3 (c,f) all show similarly stepped surfaces and a (1x1) periodicity. Scale bars in (a)-(c) are 200 nm those in (d)-(f) are 2 nm^{-1} .

Following thinning and annealing, the surface of each sample demonstrated steps of unit cell height observed by AFM as in Figure 3.1(a-c), akin to surfaces of similar oxide materials after comparable processing [73, 74]. Surface sensitive electron diffraction, which involves an electron beam in nanodiffraction geometry positioned at a very thin/edge

region of the sample, was performed on these samples and did not indicate any larger cell reconstruction as seen in Figure 3.1(d-f). This indicates a (1x1) periodicity. Additionally, there is no amorphous surface scattering typical of ion polished samples prior to annealing, indicating that the surface is ordered.

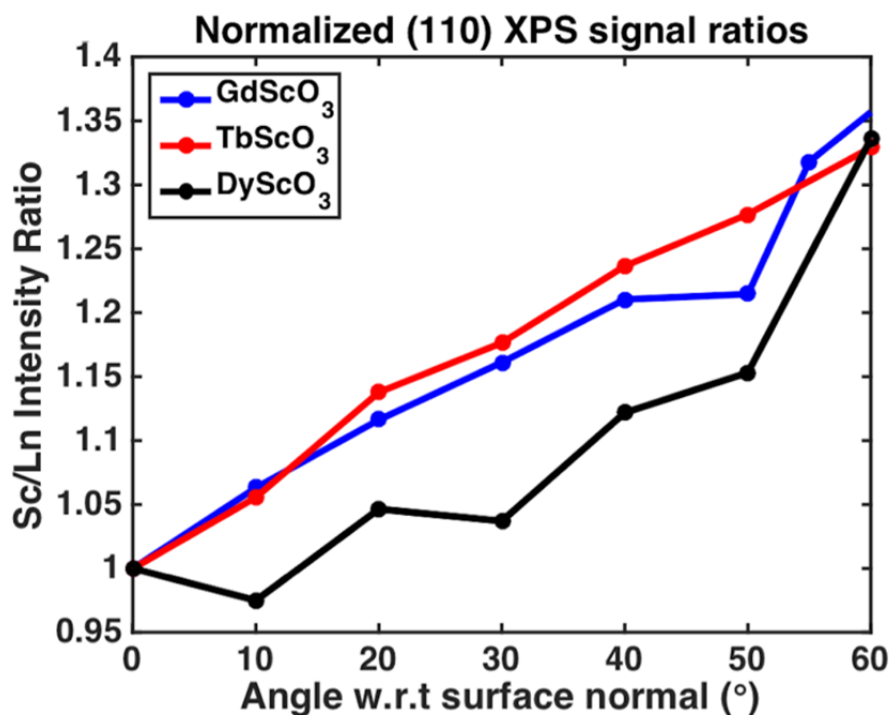


Figure 3.2. Angle resolved XPS intensity ratios of the integrated scandium 2p and lanthanide 3d signals as a function of angle demonstrate a relative increase in the Sc signal as the angle of the detector with respect to the surface normal is increased, indicating a Sc rich surface. The signals were normalized such that the ratio at $\theta = 0$ was 1.

The surface chemistry was probed with angle-resolved XPS and the results are given in Figure 3.2 for each of the studied materials. By taking the ratio of the Sc 2p and the Ln 3d signals as a function of the detector angle, it is evident that both (1) the ratio shifts in favor of Sc at higher angles and (2) it does so in a similar fashion for

all 3 materials within the error of the experimental method. As discussed in Chaptr 2, increasing the detector angle, θ , with respect to the surface normal causes the surface to contribute more to the measured signal as the effective escape depth of the electrons, d , decreases with the relationship $d = \lambda \cos(\theta)$, where λ is the inelastic mean free path of the generated photoelectron with a specific kinetic energy in the material. Therefore, these results indicate that all of the studied materials have a similarly Sc rich surface.

3.4. XPS Model

Beyond knowing that the surface reconstruction on the LnScO₃ materials is Sc rich, one can go further to quantify the chemistry of the surface by modeling the XPS signals and considering the important constraint of valence neutrality. The quantification of XPS signals is discussed first in this section.

Using calculated photoionization cross sections of the relevant core states [75], the planar density of the atoms, and the inelastic mean free paths of the photoelectrons generated in the material, one can generate a model for the relative signal between two different atomic orbitals as a function of detector angle. (As an aside, the calculated values of the photoionization cross sections may differ from experimental values and the sensitivity of the model to this potential error will be discussed later; furthermore, there are various methods for calculating these values, and interested readers are directed to the references [76–78]) With the use of additional constants one can also model the absolute signals, but in this case we are concerned with the relative difference between the Sc 3p and Ln 4d signals, and those constants are inconsequential. A full discussion of how to model these absolute signals can be found in the references [79–81].

The bulk signal ratio between the aforementioned states is modeled using the following equation:

$$(3.1) \quad \frac{I_{Sc2p,bulk}}{I_{Ln3d,bulk}} = \frac{\alpha_{Sc2p}\rho_{Sc} \sum_{m=1}^{\infty} A_{Sc2p}^{2m-2}}{\alpha_{Ln3d}\rho_{Ln} \sum_{m=1}^{\infty} A_{Ln3d}^{2m-1}} = \frac{\alpha_{Sc2p}\rho_{Sc}}{\alpha_{Ln3d}\rho_{Ln}} \frac{1}{A_{Sc2p}^2 - 1} \frac{A_{Ln3d}^2 - 1}{A_{Ln3d}}$$

where α_i is the photoionization cross section, ρ_i is the areal density of the relevant atom, m is the number of unit cells generating signal (with respect to penetration/escape depth, not in-plane width), and A_i is an attenuation function dependent on the layer thickness, t , inelastic mean free path of the electron λ_i , and the angle of the detector with respect to the surface normal θ , such that $A_i = \exp(-\frac{t}{\cos\theta\lambda_i})$. Simply put, the $\alpha_i\rho_i$ term represents signal generation and A_i attenuates that signal as it moves through the solid. The sum converges to the expression on the right side of the equation, and this represents a slab that is thicker than the inelastic mean free path of the relevant electrons.

This equation is formulated such that the topmost layer of the LnScO_3 bulk unit cell is a ScO_2^- layer, though this can be changed by swapping the exponents of the attenuation function in the summation term between the Ln and Sc. To add more surface layers to the model, for example another Sc rich layer, one would apply the attenuation function to the bulk signals and then add another layer of unattenuated Sc signal, as demonstrated here:

$$(3.2) \quad \frac{I_{Sc2p}}{I_{Ln3d}} = \frac{\alpha_{Sc2p}\rho_{Sc2p} + A_{Sc2p}I_{Sc2p,bulk}}{A_{Ln3d}I_{Ln3d,bulk}}$$

Figure 3.3 compares the experimental DyScO_3 data against the model both for different numbers of excess Sc layers and for Sc layers of different chemistry (i.e. different Sc areal density). As seen, there is a significant change in the predicted signal when the

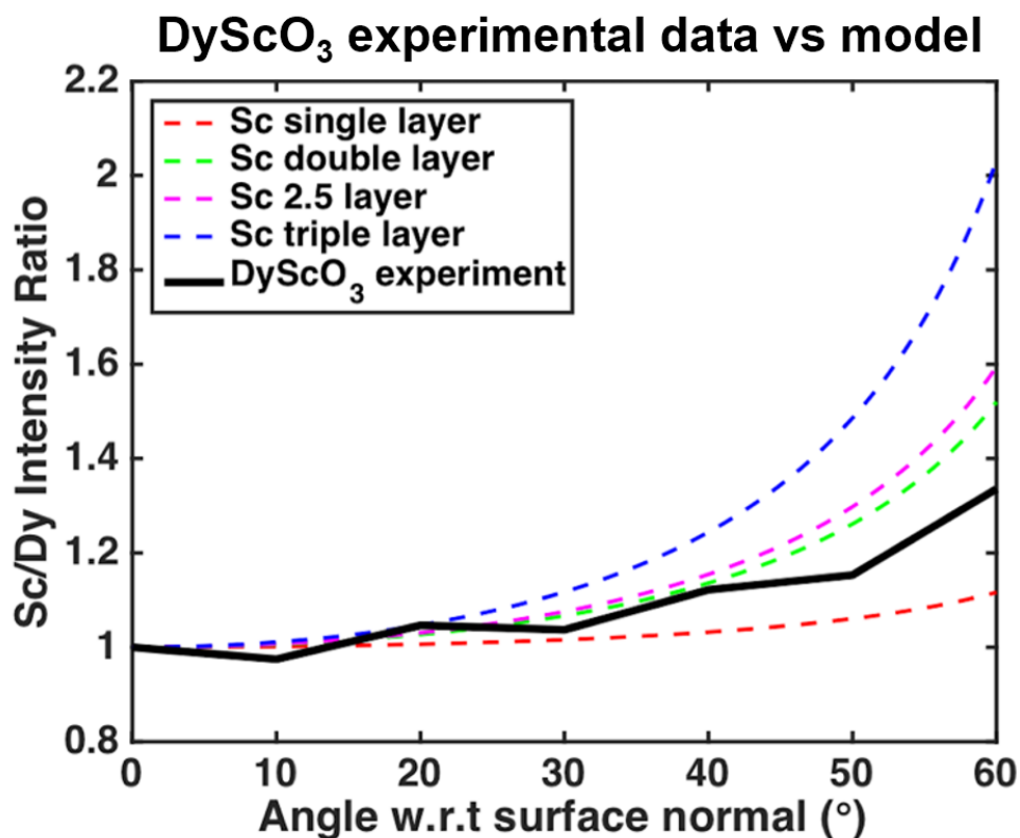


Figure 3.3. Modeled intensity ratios compared to the DyScO₃ experimental data. The data has the best match to the double layer, though the model is too coarse and experimental uncertainty too high to predict an exact layer chemistry.

number of surface layers is changed; however, changing the chemistry of each layer yields little change (the difference between the double and 2.5 layer in Figure 3.3 is a 50% increase in the Sc density of the outer layer). It should be noted that the model assumes a perfect, clean surface while in experiment there will always be a small amount of adsorbed species on the surface from the environment. This would introduce some damping on the overall signal; however the magnitude would be quite small. The data was found to have the closest match to the double layer termination, though the error associated with the

experiment from sources such as photoelectron channeling, inherent error in the model, and the small magnitude of the changes associated with different chemistries makes it impossible to predict an exact stoichiometry.

Returning to address any error associated with calculated values of α_i , the impact of changing this term will be similar to changing the layer chemistry, ρ_i . This is relatively minor for a change of 50% comparing the double layer and 2.5 layer ρ_i in Figure 3.3, indicating that uncertainty in these values is not a significant source of error in the model.

3.5. Valence Neutrality of the Double Layer

While the aforementioned data and model are too coarse to ascertain the stoichiometry of the double layer, chemical constraints reduce the number of allowable stoichiometries significantly due to the condition of valence neutrality at the surface. While valence neutrality is relatively straightforward to achieve in a 242 perovskite such as SrTiO_3 , this is not the case in LnScO_3 , a 332 perovskite. As outlined in Figure 3.4, each atomic layer in LnScO_3 has a 1^+ or 1^- valence, compared to neutral layers in SrTiO_3 . As a result, the outermost layer of the surface reconstruction must balance the non-zero valence of the layer below.

Pauling's Rules [82] and their application to surface structures [59] will be discussed in greater detail in Chapter 4, though one important consequence of these rules here is that atoms will conform to bulk-like structures if possible. This implies that the subsurface Sc layer of the Sc rich double layer will be as bulk-like as possible, adopting the ScO_2^- layer structure to achieve the lowest energy configuration. As a result, the outermost layer will need an overall valence of 0.5^+ to balance. (A convenient way to consider valence

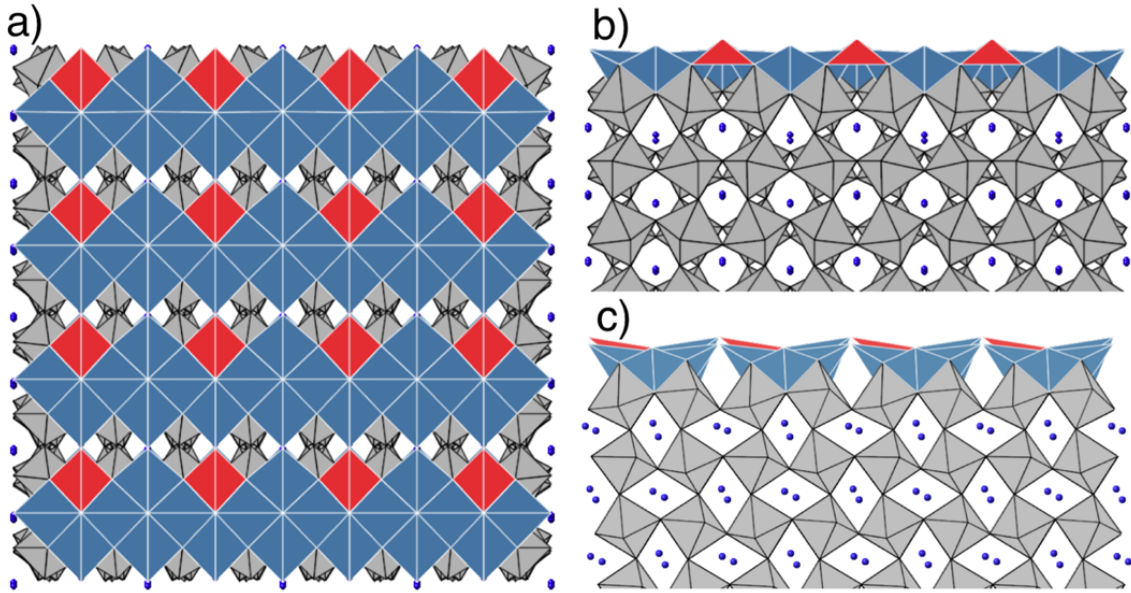


Figure 3.5. DFT relaxed structure of the double layer termination on DyScO_3 (110). Considering the $Pbnm$ reference frame, the view directions are $[110]$ (a), $[\bar{1}10]$ (b), $[001]$ (c). Bulk ScO_6 octahedra are colored grey, surface ScO_5 are blue, and surface ScO_4 are red. Dy atoms are pictured as blue spheres.

3.6. Double Layer Solution and Electronic Structure

In the previous sections, constraints were established through experiment and chemical theory that the surface is a double layer with (1×1) periodicity and a stoichiometry of Sc_3O_4 in the outermost layer. Of 8 available sites for Sc, 6 of them are filled to give a valence neutral structure and all of these permutations were explored using DFT. The resulting low-energy solution is given in Figure 3.5 for DyScO_3 and is largely the same on GdScO_3 with some minor variations in the exact positions of the surface atoms owing to the differences in lattice parameter and octahedral tilts of the materials. The surface of TbScO_3 is likely very similar to this as well, however there are ambiguities with respect

to the single, minority Tb 4f electron that preclude calculating an exact DFT minimized structure [49].

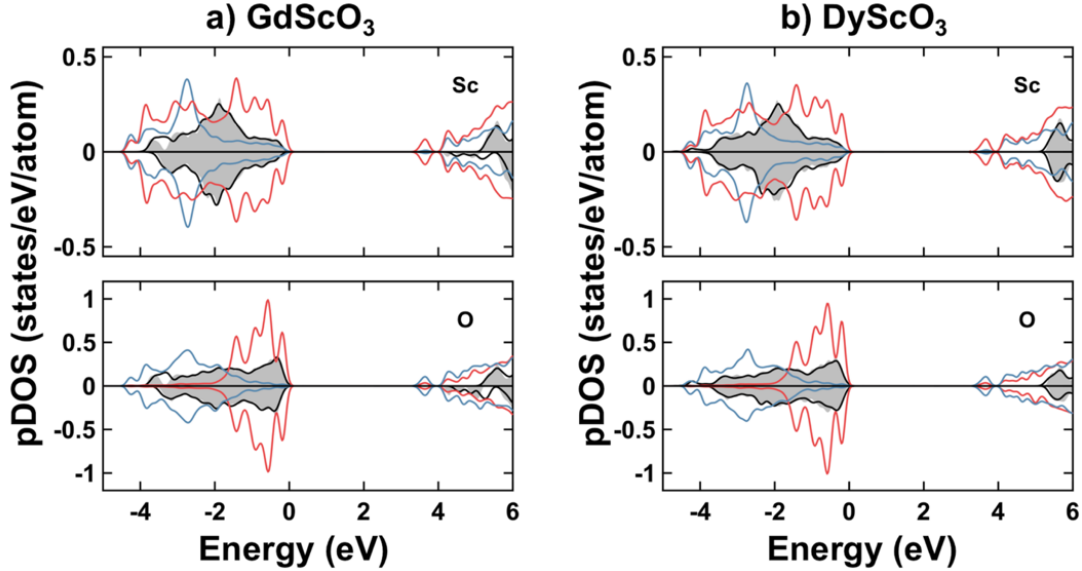


Figure 3.6. PDOS of GdScO_3 (a) and DyScO_3 (b). The figure lines are colored to correspond with Figure 3.5, where red is associated with ScO_4 , blue with ScO_5 , and black are the bulkmost ScO_6 . The gray shaded region shows the pDOS from a separate, bulk calculation. The Fermi energy (0) is set at the highest occupied state of the O 2p. The occupied Sc and unoccupied O states have been scaled up by a factor of 10 for clarity.

This structure consists of ScO_5 (the \square denotes a vacancy site) and ScO_4 units colored blue and red respectively. The pDOS of each of these units is plotted in Figure 3.6, and as demonstrated the surface states extend below the bulk conduction band edge and an in-gap state is created which is largely attributed to the ScO_4 units. This in-gap state has been observed experimentally via EELS and ultraviolet photoelectron spectroscopy measurements [83], verifying the presence of these underbonded Sc atoms.

3.7. Conclusions

As a result of the polarity of each atomic layer, the (110) surface of LnScO_3 must undergo reconstruction to attain a valence neutrality. Here a Sc rich double layer termination was identified as one such reconstruction, though importantly it is not the only possible surface structure for this material. Additionally, surface structures containing adsorbates were not explored here and are a candidate for future experimental and theoretical studies.

This valence balancing is not unique to LnScO_3 : the non-zero valence of each (110) layer is universal to all 332 perovskites. As a result of this non-zero valence, the limited number of accessible surface chemistries at the surface of these materials significantly narrows the window of potential reconstructions. Therefore, it is likely that this reconstruction sits on or near the convex hull for most, if not all, $\{100\}_{pc}$ surfaces of 332 perovskite materials with double layer, B-site terminations provided the chemistry can be controlled. This can be seen in the LnScO_3 materials here and in the upcoming chapter, where a similar double layer is present regardless of the A site cation and synthesis method.

The work in this chapter has been published in [84].

CHAPTER 4

LnScO₃ Nanoparticle Surfaces**4.1. Introduction**

The (110) surfaces of GdScO₃, TbScO₃, and DyScO₃ single crystals were studied in Chapter 3, and in this chapter I transition to the hydro-sauna synthesized LnScO₃ (Ln = La, Nd, Sm, Gd, Dy) nanoparticles used throughout the remainder of this thesis [25, 26]. In addition to (110) surfaces, these nanoparticles expose facets of the (001), (100), (010), and (112) surfaces. Like the (110), the (001) of LnScO₃ is a (100)_{pc} surface, and together the (110) and (001) facets represent a significant majority of the exposed surface area. The other 3 surfaces mentioned above constitute the {110}_{pc} family of planes and appear at the particle edges, as shown in Figure 4.1.

Knowledge of the structure and chemistry of the exposed nanoparticle surfaces will be important when attempting to understand the behavior of these materials both in catalysis (Chapter 7) and when interacting with supported metal nanoparticles (Chapter 6 and Chapter 8); however, the experimental techniques used in Chapter 3 to study single crystal surfaces such as surface sensitive electron diffraction or angle resolved XPS are not applicable here due to the sample morphology. Instead, aberration corrected profile view imaging [54, 85–93], along with the chemical constraints mentioned in Chapter 3, are used to inform potential surface models that are assessed via DFT. Multislice simulations of these predicted structures are then compared to the images to verify those models.

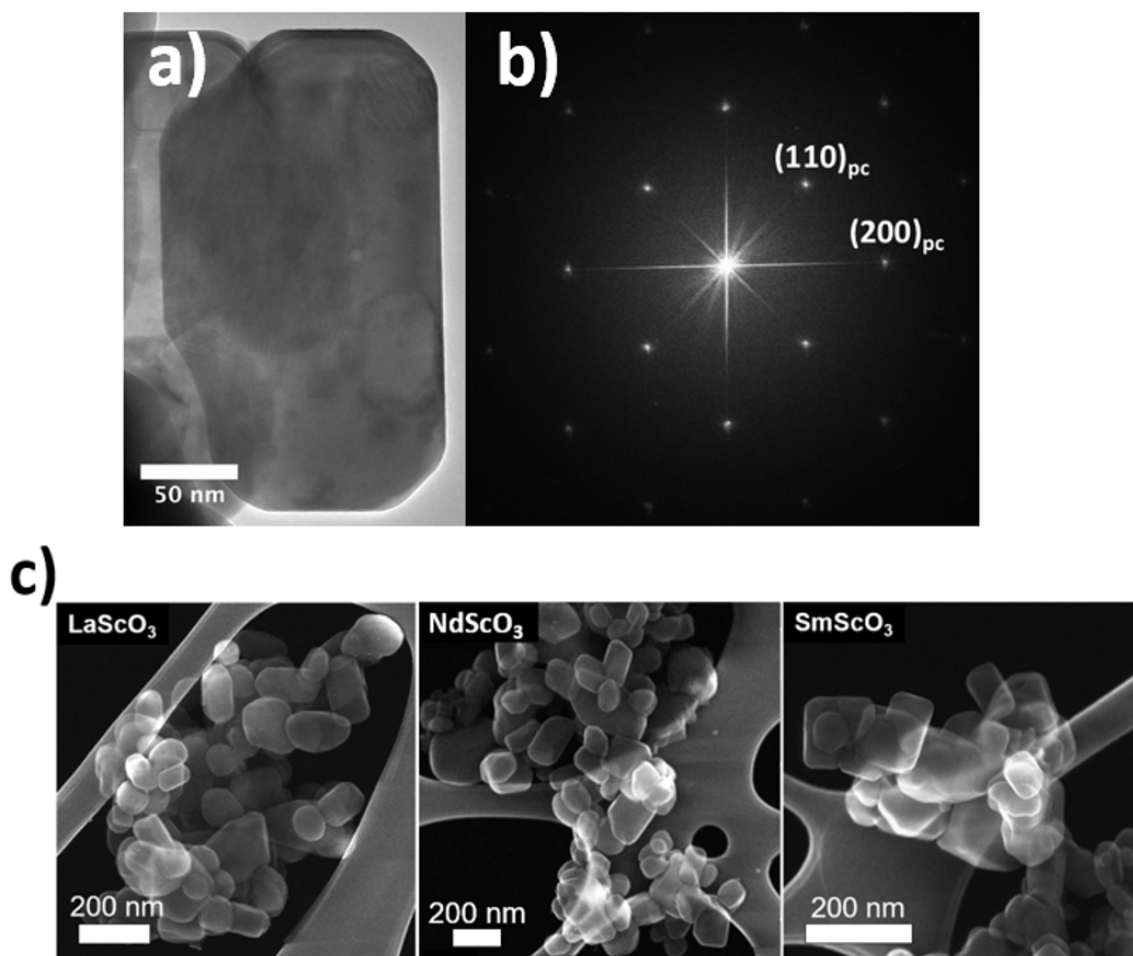


Figure 4.1. HREM of a faceted NdScO_3 nanoparticle in (a), along with a corresponding power spectrum of the image in (b). The particles primarily expose the $\{100\}_{pc}$ surfaces, along with the $\{110\}_{pc}$ at the edges. Secondary electron images of the nanoparticles used as supports in the catalytic experiments in Chapter 7 are shown in (c).

Using this approach, Sc-rich surfaces are observed on all facets of the nanoparticle supports. The $\{100\}_{pc}$ surfaces have a double layer, Sc-rich surface termination on a majority of the exposed area, and a small fraction of the exposed surface is terminated

with a single layer reconstruction. Turning to the $\{110\}_{pc}$ surfaces, they are all found to contain single layer, Sc-rich reconstructions with oxygen vacancies.

4.2. Methods

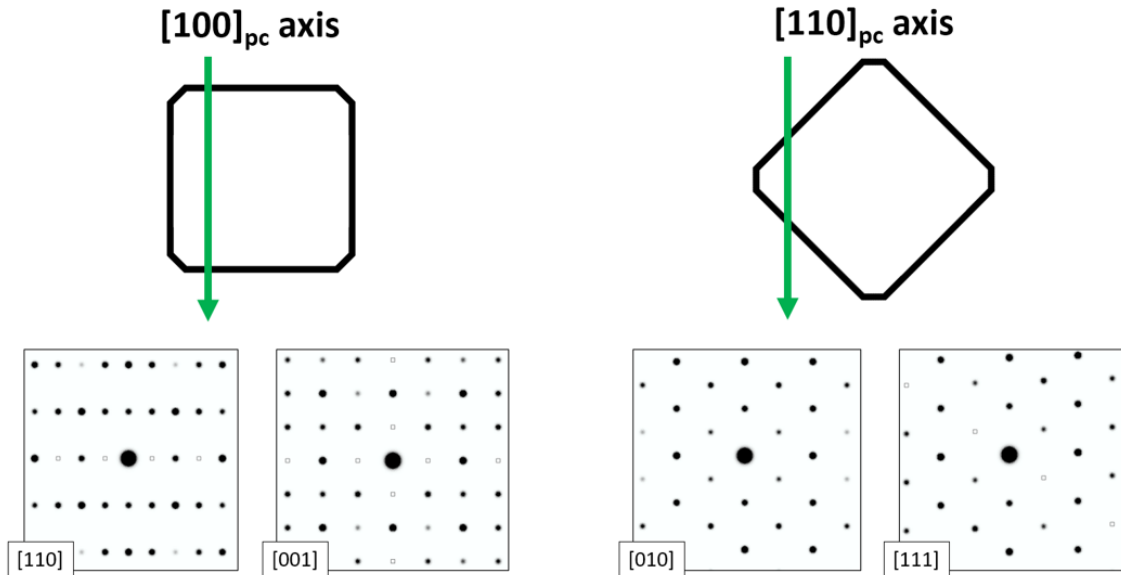


Figure 4.2. Beam/sample interaction geometry when imaging down a $[100]_{pc}$ and $[110]_{pc}$ zone axis of a faceted, cuboidal particle with beveled edges, along with kinematically calculated diffraction patterns of the potential zone axes. When imaging along a $[100]_{pc}$ direction, the sample is thick but the view direction is easily discernible between the different $[100]_{pc}$ directions, the $[110]$ and $[001]$. Conversely for the $[110]_{pc}$ zone axes, it is possible to image using a very thin region of sample, but it can be difficult to determine the specific zone axis as the diffraction patterns of two of the $[110]_{pc}$ directions are nearly identical.

Aberration corrected TEM was performed using the ACAT operated at 200 kV at Argonne National Laboratory. To obtain profile view images of the surface structures, the nanoparticles were oriented such that the surface normal of the imaged surface is perpendicular to the beam direction. For the faceted LnScO_3 particles studied here,

this involves imaging down either a $[100]_{pc}$ or $[110]_{pc}$ zone axis. Both of these imaging geometries have benefits and drawbacks which are highlighted in Figure 4.2.

Table 4.1. Number of atoms and k-point meshes used in DFT calculations. With the exception of the “(001) double layer (1x1)” and the “(010) Ln_2O vacant” structures, all k-point densities are the same. Those exceptions were not converged to higher densities as it quickly became apparent they were not realistic solutions.

Slab Type	Atoms (total)	k-point mesh
(001) double layer (1x1)	102	4x4x1
(001) double layer (2x2)	400	4x4x1
(110) single layer	230	1x4x4
(010) Ln_2O vacant	122	3x1x2
(010) O_2 vacant	132	6x1x4
(100) O_2 vacant	132	1x6x4
(112) O_2 vacant	260	1x3x4

DFT calculations were performed using parameters described in Chapter 2. All calculations were performed with $P\bar{1}$ symmetry and the number of atoms and k-point mesh density of each slab are found in Table 4.1. In all cases, atomic positions were allowed to relax. Most of the calculations are performed using GdScO_3 , though the low energy solution for the (001) double layer reconstruction was also calculated on NdScO_3 for comparison. Multislice simulation was performed with the MacTempasX software package using typical working conditions of the ACAT ($C_s < 10 \mu\text{m}$, 40 nm focal spread).

4.3. $\{100\}_{pc}$ Surfaces

4.3.1. (110) Double Layer

Figure 4.3 contains images of $\{100\}_{pc}$ double layer surface terminations on the LnScO_3 nanoparticles. While it is difficult to determine if the images in 4.3(a-e) are the (110)

or (001) surfaces as discussed in the previous section (see Figure 4.2), Figure 4.3f is definitively the (001) while 4.3g is the (110). Figures 4.3c and 4.3g contain multislice simulations based on the (110) structure presented in Chapter 3 overlaid and demonstrate a good match, confirming the double layer reconstruction on both the nanoparticle and single crystal (110) surfaces.

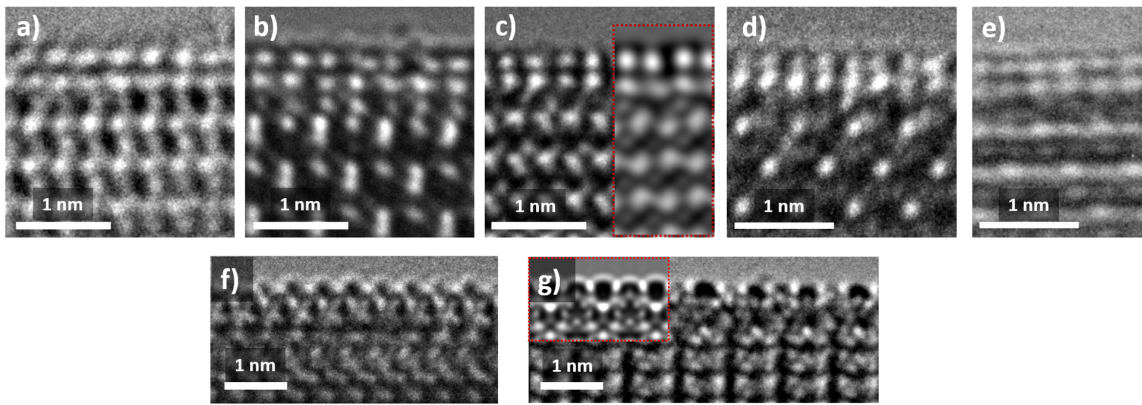


Figure 4.3. Aberration corrected HREM of the Sc-rich double layer terminations on the LnScO_3 materials. Figures (a-e) are LaScO_3 , NdScO_3 , SmScO_3 , GdScO_3 , and DyScO_3 in order viewed along a $[110]_{pc}$ axis, where the small thickness and surface structure allow for a clear visualization of the double layer. Shown in (f) and (g) are the (001) LaScO_3 surface and (110) GdScO_3 surface respectively viewed along a $[100]_{pc}$ axis. In (f) and (g) the sample thickness and structure do not allow for a clear visualization of the double layer, but the overlaid multislice simulation, outlined in red, in 3g shows a good match at the surface. 3c also has an outlined multislice simulation overlaid.

4.3.2. (001) Double Layer

The (001) surface in Figure 4.3f has a similar surface motif as the (110) in 4.3g, indicating the surface reconstruction is comparable. This is not surprising as both constitute $(100)_{pc}$ type surfaces, however they are symmetrically distinct and the (001) surface must be

considered independently to explore any potential differences. As discussed in Chapter 3, a valence neutral $(100)_{pc}$ surface will have 6/8 potential Sc sites of the outer layer occupied, and it is these specific site occupancies and the resulting atomic relaxations that may vary between the (110) and (001). To explore the potential surface reconstructions, (1x1) and (2x2) structures were considered that both maintained valence neutral stoichiometry and adhered well to Pauling's Rules – the impact of Pauling's Rules on surface structures and energies [59] will be discussed in the next section.

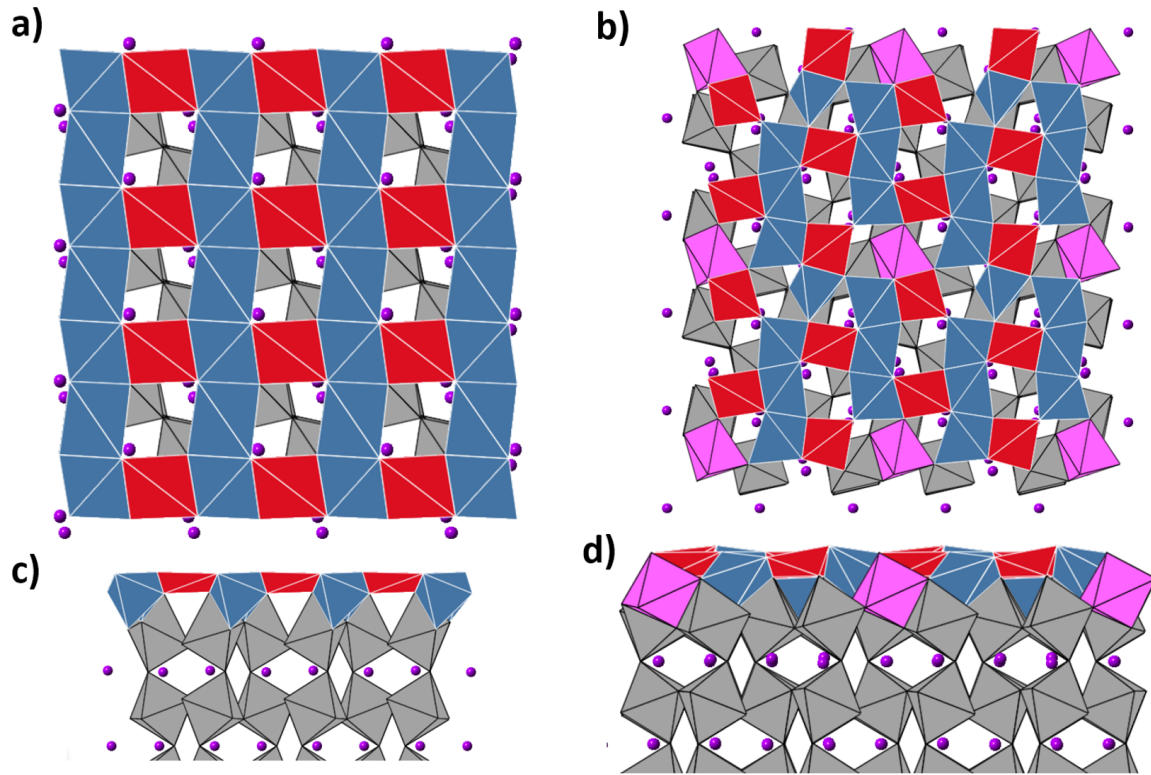


Figure 4.4. DFT relaxed structures of the low energy solutions of the (001) double layer solution on $GdScO_3$ with (1x1) (Figs a/c) and (2x2) (Figs b/d) symmetries. (a) and (b) show plan views of the surfaces along the [001] direction, while (c) and (d) are profile views along the [010]. Grey polyhedra are bulk ScO_6 units, pink are surface ScO_6 , blue are surface ScO_5 , and red are surface ScO_4 . Purple atoms are Gd.

The low energy solutions for both the (1x1) and (2x2) structures are shown in Figure 4.4. These structures are stoichiometrically identical and only differ in the which of the potential Sc sites are occupied. The polyhedral units at the surface are either ScO_4 , ScO_5 , or ScO_6 which are red, blue, and pink respectively in Figure 4.4. While the specific site occupancies and relaxations are different than the (110) surface, the approximate positions of each Sc site are similar. As a result, they are comparable in profile imaging, as demonstrated in Figure 4.5.

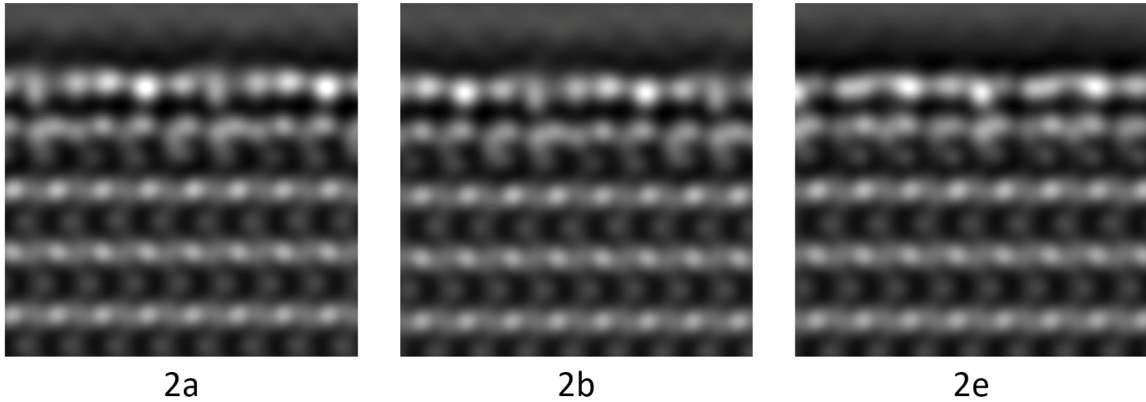


Figure 4.5. Multislice simulations of selected (2x2) structures on the GdScO_3 (001) surface are shown above. As noted in Table 4.2, 2a is the low energy solution while 2b is very close in energy such that it likely coexists on the surface. Structure 2e is modeled after the (110) double layer reconstruction before relaxation. As shown in the simulations, variations to the specific polyhedral arrangements do not generate a significant change in the profile view images as the structures are two-dimensional projections.

The (2x2) is the lowest energy structure, with an excess surface energy of 2.15 J/m^2 on GdScO_3 . For comparison, this structure was also calculated on NdScO_3 and the pDOS of the (2x2) structure on both GdScO_3 and NdScO_3 are found in Figure 4.6. In light of the similarities in the surface states between the two (the surface states on the two

materials are more similar to each other than to their respective bulk states), I expect that calculations of the other LnScO_3 materials would yield very similar results.

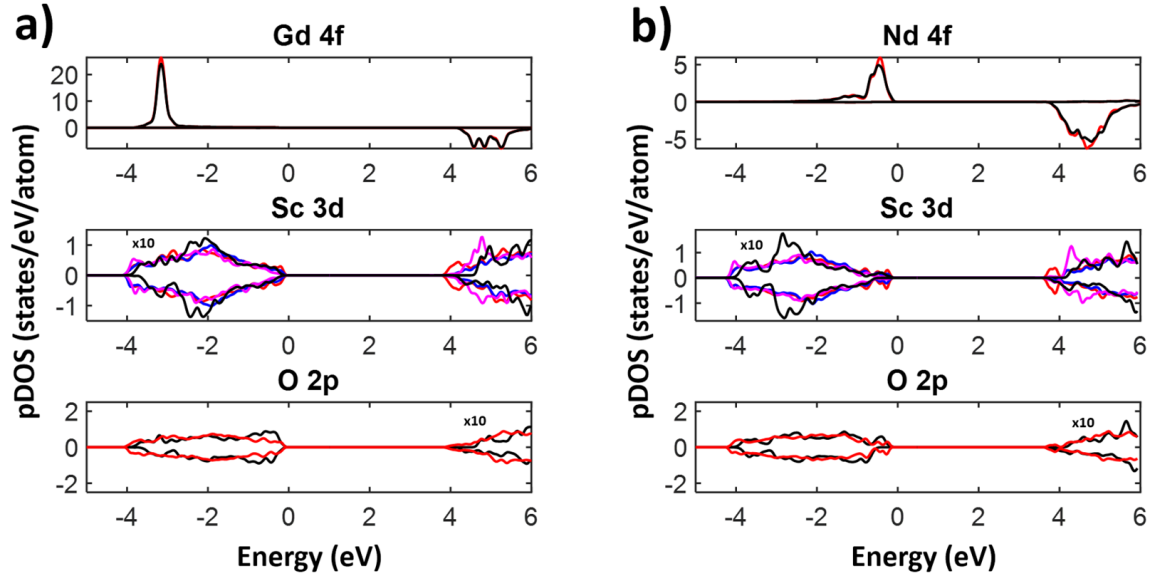


Figure 4.6. pDOS of the Ln 4f, Sc 3d, and O 2p states of the double layer (001) structure on GdScO_3 (a) and NdScO_3 (b). In all cases, black lines represent the bulkmost unit cell. For the Ln 4f and O 2p, red lines are the surface-most atoms, and in the Sc 3d purple lines represent Sc in ScO_6 polyhedra, blue in ScO_5 , and red in ScO_4 . The occupied Sc 3d and unoccupied O 2p states are magnified by a factor of 10 for visibility as noted in the figure.

The relative energies of other potential surface structures that were assessed via DFT are given in Table 4.2. Considering that k_bT at room temperature is approximately 25 meV, along with the added enthalpy and entropy of the hydro-sauna synthesis, I hypothesize that the surface is either (1) a mixture of domains of structure 2a and 2b or (2) disordered with respect to which specific sites are vacant while still maintaining valence neutrality (this is discussed in the next section).

Table 4.2. Relative energy of each (1x1) and (2x2) structure compared to the minimum energy solution, 2a. Structures 2a-2g represent the (2x2) structures and 1a/1b are (1x1). Structures 2a-2d are translations of the low energy solution in Figure 4.3(b/d), while 2e-2g are based on the solved (110) structure, which is shown to be comparatively unfavorable on this surface.

(001) structure	Energy difference (meV/PC unit)
2a	0
2b	84
2c	191
2d	204
2e	3169
2f	3921
2g	5935
1a	549
1b	908

4.3.3. Pauling's Rules in Surface Structures

Although the (1x1) solution has a higher energy than the (2x2) by 549 meV per pseudocubic unit and almost certainly is not present on the nanoparticles, it is worth discussing in comparison to the (2x2) as an example of how Pauling's Rules [82] apply to surfaces [59].

Considering Pauling's rules when generating hypothetical surface structures, a structure should (1) maximize symmetry, (2) prefer corner sharing to edge or face sharing polyhedra, and (3) attempt to mimic the bulk structural units if possible. These follow directly from the first, third, and fifth rules for bulk crystals. When considering the (1x1), the symmetry constraints lead to neat, grid-like rows of edge sharing ScO_x polyhedra, with the polyhedral unit at the intersections of the gridlines sharing 4 edges. In the (2x2), the polyhedral units are staggered, which both allows corner sharing and a relaxation of some Sc atoms away from the vacuum far enough to coordinate with 6 O atoms, as Sc does in the bulk. Furthermore, the (1x1) reconstruction results in a vertical elongation of the

subsurface ScO_6 polyhedra that is noticeable upon visual inspection of Figure 4.4c, and this is not present in the (2x2).

Despite the lower overall symmetry, the favorable corner sharing and presence of bulk-like polyhedra in the (2x2) results in a lower energy. A similar effect is also attainable through disorder in the occupied Sc sites. For clarity, this is not a completely random arrangement of Sc on the surface, rather disorder in which 6 of the 8 possible Sc sites are occupied in a given surface unit, avoiding the grid-like rows of the (1x1) that lead to higher energy structures. The fact that other (2x2) polyhedral arrangements of the surface are very close in energy (Structures 2a-2d) support this hypothesis.

4.3.4. Single Layer Termination

As seen in Figure 4.7, a single layer reconstruction was observed alongside the double layer. This half-unit cell step is infrequently observed. From imaging I estimate <10% of the surface contains this reconstruction. Comparing the image to the neighboring atomic layers and the bulk, the structure appears bulk-like; however, a bulk single layer termination at an ScO_2^- layer is not valence neutral. To achieve valence neutrality in this layer without the addition of adsorbates, 0.25 O atoms must be removed per ScO_2^- , which corresponds to removing 1 O atom per $\text{Sc}_4\text{O}_8^{4-}$ to yield a surface chemistry of $\text{ScO}_{1.75}^{0.5-}$ per pseudocubic unit. This gives valence neutrality when balanced with the subsurface LnO^+ layer.

In a similar method to that described for the double layer terminations, permutations of the single layer surface that maintain a bulk-like ordering (as informed by the images) with the required oxygen vacancy were assessed with DFT. The resulting energies are

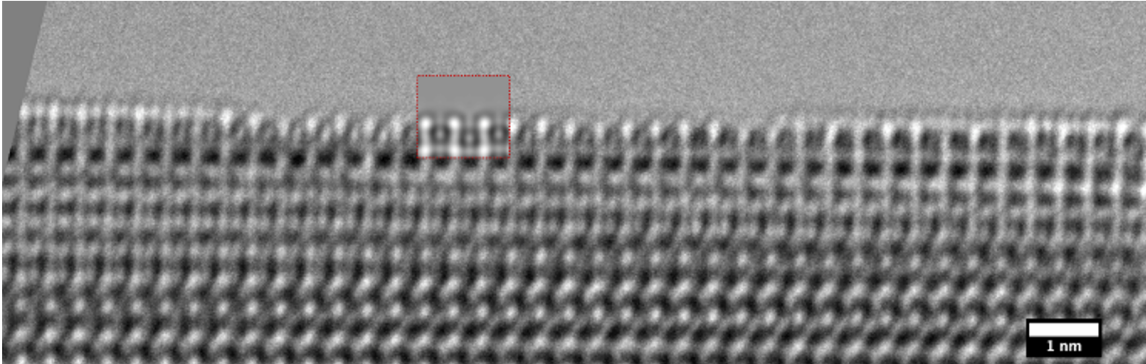


Figure 4.7. Aberration corrected HREM of a single layer region on a $(100)_{pc}$ surface of LaScO_3 . Outlined in red is a multislice simulation based on the predicted low energy structure in Figure 4.8. The rapidly changing thickness of the nanoparticle moving away from the surface makes a larger multislice simulation unfeasible.

reported in Table 4.3, and the low energy solution is pictured in Figure 4.8 along with the corresponding pDOS. Structures 1 and 2 only varied by 15 meV per pseudocubic unit, which is below k_bT at room temperature and nominally equivalent. As a result, both terminations are equally likely (probably coexisting in small domains). This calculation was performed on a (110) surface, and an analysis of the (001) would be very similar, though perhaps with a different preferred vacant site as with the double layer terminations.

Table 4.3. Energy differences compared to the minimum energy structure the single layer reconstruction. The energies of structures 1 and 2 are essentially equivalent considering k_bT at room temperature.

Single layer structure	Energy difference (meV/PC unit)
1	0
2	15
3	143
4	225
5	2478
6	2481

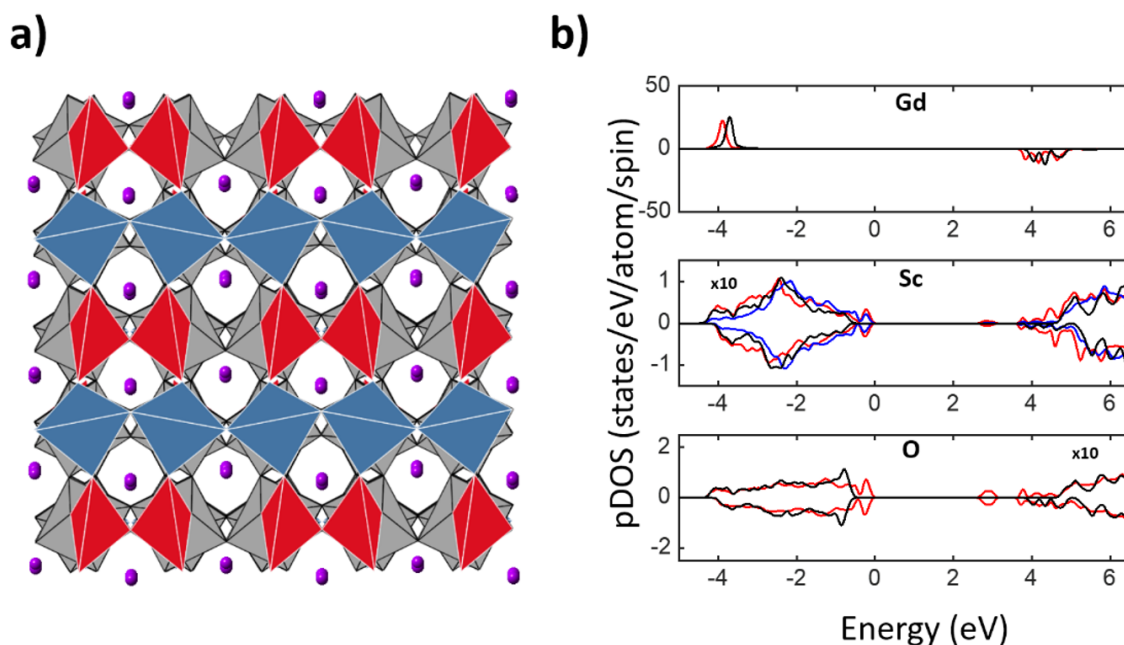


Figure 4.8. The DFT predicted structure for the single layer termination on the (110) surface is pictured in (a), with polyhedra colored as described in Figure 4.4. (b) The pDOS of the surface is shown in (b) with the same convention as Figure 4.6.

Mixed terminations are known to occur on complex oxides (such as SrTiO_3), and the presence of a single layer mixed in with the double layer is not particularly surprising. It should be noted that the single and double layer surfaces have a different stoichiometry and can therefore coexist without issue; additionally, they are not directly comparable via DFT calculated energy alone. This single layer reconstruction was observed infrequently, and not seen at all on the single crystal samples examined in Chapter 3 (there were no half-unit cell steps in the AFM). The synthesis conditions of the nanoparticles (moderate temperatures in humidified Ar) and preparation of the single crystals (high temperature anneal in air) are quite different and varied processing environments are known to affect surface reconstructions. Evidently, the hydro-sauna synthesis environment is favorable

towards the single layer termination – the double layer is still preferred overall on the nanoparticles, but the single layer is favorable enough during synthesis to coexist on a small portion of the surface.

4.4. $\{110\}_{pc}$ Surfaces

Figure 4.9 contains aberration corrected profile view images of two $(110)_{pc}$ surfaces, the (010) on LaScO_3 and (100) of GdScO_3 , with a multislice simulation of the predicted low energy solution overlaid on the LaScO_3 . Both surfaces appear the same, indicating the reconstruction is similar on the different $\{110\}_{pc}$ surfaces and on the different materials. This result is consistent with the similarity of the $\{100\}_{pc}$ double layer surfaces across the LnScO_3 series.

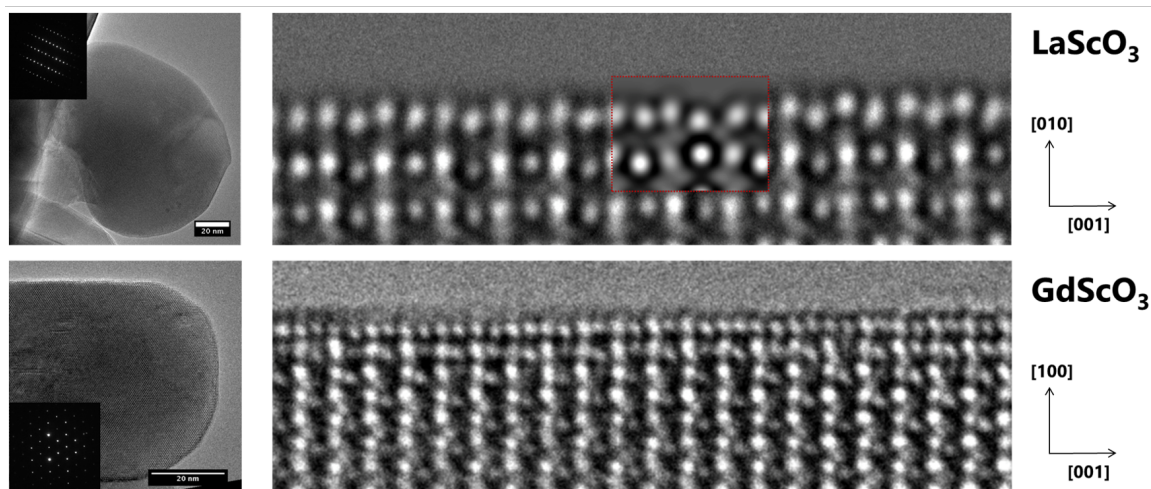


Figure 4.9. HREM of two $(110)_{pc}$ surfaces are shown on the right, along with corresponding low magnification images and diffraction patterns of the nanoparticles on the left. A multislice simulation based on the (010) predicted structure is overlaid on the LaScO_3 and shows an excellent match.

The close similarity between the surface and bulk ordering is immediately evident; however, the intensity at the surface is relatively constant at the cation columns where the bulk alternates between light columns, or “type 1”, and columns with a light center and dark outer ring, “type 2”. Considering the bulk portion of the multislice simulation on LaScO_3 in Figure 4.9, the type 1 and type 2 columns correspond to Sc and Gd columns respectively, and the surface of the image matches well with the Sc columns. This suggests that the surface is Sc rich, similar to the $\{100\}_{pc}$ surfaces, and maintains a bulk-like ordering.

Candidate structures of Sc-rich surface terminations were compared using DFT. In LnScO_3 , the $(110)_{pc}$ atomic planes consist either of $\text{Ln}_2\text{Sc}_2\text{O}_2^{8+}$ or O_4^{8-} , and require reconstruction to achieve valence neutrality. This can happen in two ways, either removing two O atoms in a terminating O_4^{8-} layer (and replacing the Ln cations with Sc in the surfacemost LnScO_3 layer as informed by the imaging), or by removing Ln_2O^{4+} from a terminating $\text{Ln}_2\text{Sc}_2\text{O}_2^{8+}$ layer.

Permutations of both structure types on the (010) surface were assessed in DFT (denoted in Table 4.1 as “(010) Ln_2O vacant” or “(010) O_2 vacant”), and in all cases removing the Ln_2O^{4+} yielded a relaxed structure was far from bulk-like, eliminating these as potential solutions. When creating two O vacancies, the remaining O atoms relax towards the bulk resulting in a bulk-like termination consistent with the imaging, the lowest energy of which is used for multislice in Figure 8. The structure of the low energy solution, along with the pDOS, is found in Figure 4.10. Table 4.4 contains the relative energies of the other O_2 vacant structures.

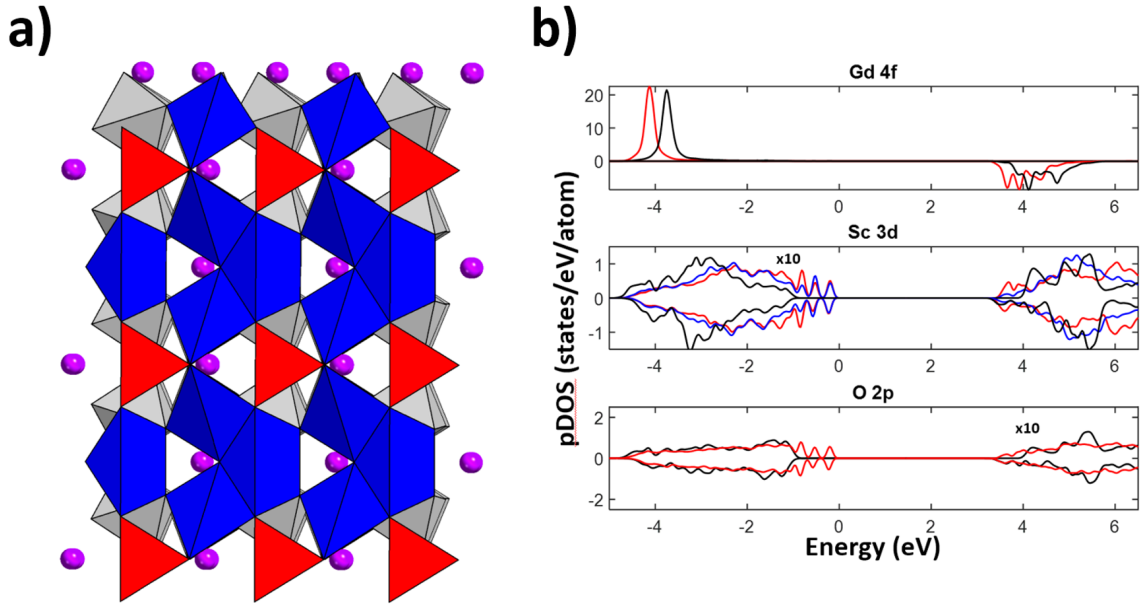


Figure 4.10. Predicted structure of the oxygen vacancy containing reconstruction on the (010) surface is shown in (a), with the pDOS in (b). Colors in (a) and (b) are similar to previous figures.

Table 4.4. Energy differences compared to the minimum energy structure the $(110)_{pc}$ single layer reconstruction.

(010) Structure	Energy difference (meV/PC unit)
1	0
2	234
3	279
4	281
5	391
6	892

Considering the O_4^{8-} layer in the $(110)_{pc}$ planes of the $LnScO_3$ structure, the octahedral tilts result in half of the O atoms in the O_4^{8-} layer sitting slightly higher and the other slightly lower as depicted in Figure 4.11 for the (010) surface. As expected, the lowest energy solution corresponds to removing the two O atoms that were farthest away from the surface and extended into the vacuum, or the two top O atoms in the layer. Comparing

the relative energies in Table 4.4 with respect to the specific O vacancies created in each structure, Structure 1 removes both top atoms, Structures 2-5 remove 1 top and 1 bottom, and Structure 6 removes both bottom atoms.

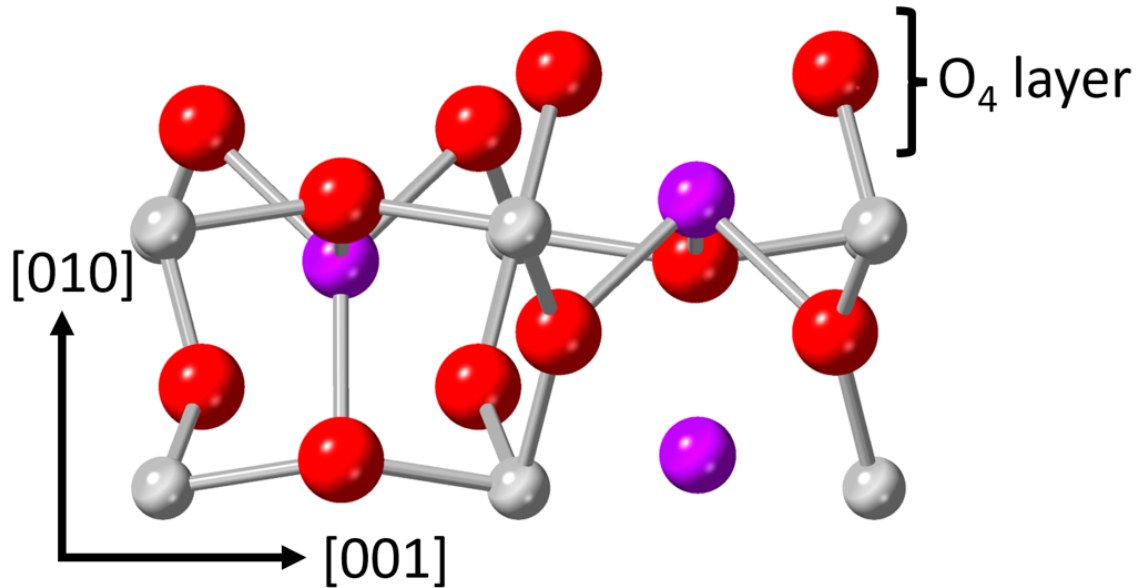


Figure 4.11. The terminating O_4^{8-} layer of $GdScO_3$ before creating the necessary two O vacancies is shown above. Here, and in the other $(110)_{pc}$ surfaces, the lowest energy configuration comes from removing the two O atoms that are farthest into the vacuum. In the diagram above that is the two rightmost O atoms. Red atoms are O, purple are Gd, and gray are Sc.

This structural search was repeated for the other $(110)_{pc}$ surfaces (the (100) and (112)) and the low energy solutions are shown in Figure 4.12. Similar to the (010) surface, removing the upper O atoms of the O_4 layer resulted in the low energy solution. Of the $(110)_{pc}$ surfaces, the (100) surface contains the most ScO_4 surface units upon relaxation. Correspondingly, the (100) has the highest excess energy of the three $(110)_{pc}$ surfaces (see Table 4.5), another demonstration of Pauling's rules.

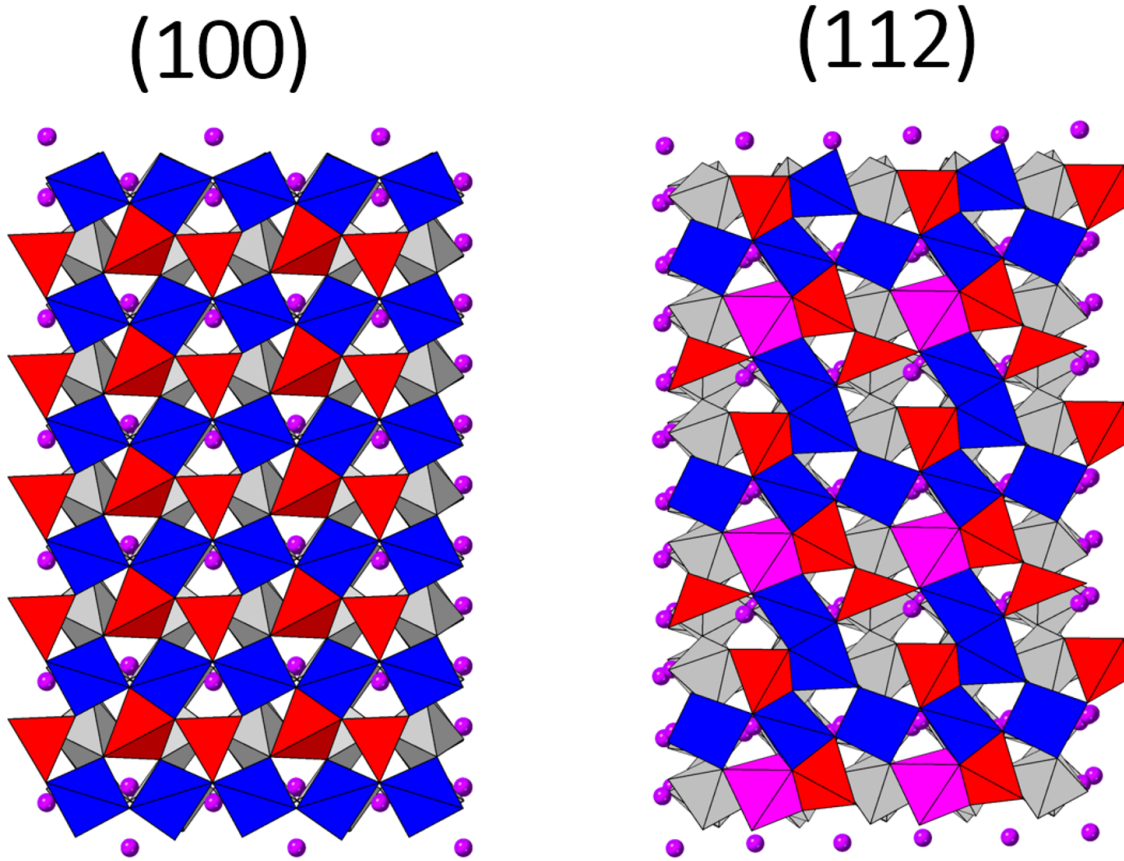


Figure 4.12. DFT predicted structures of the (100) and (112) surfaces. Though the polyhedral arrangements look quite different, the coordinating Sc atoms occupy similar sites. The polyhedral coloring convention is the same as in previous figures.

4.5. Summary of Surface Energies and Theoretical Wulff Shapes

Excess surface energies, E_{surf} , for the reconstructions presented above can be calculated using the following formula:

$$(4.1) \quad E_{surf} = \frac{E_{slab} - n_{LnScO_3} E_{LnScO_3} - m_{Sc_2O_3} E_{Sc_2O_3}}{2A}$$

Each slab used in the DFT calculations herein has a total energy of E_{slab} and a stoichiometry that can be represented as $n\text{GdScO}_3 + m\text{Sc}_2\text{O}_3$. For example, the (010) slabs have a stoichiometry of $\text{Gd}_{11}\text{Sc}_{15}\text{O}_{39}$, giving $n = 11$ and $m = 2$. Using separate, bulk calculations for the energies of the bulk unit cells (E_{LnScO_3} and $E_{Sc_2O_3}$ in Equation 4.2), and the surface area of the reconstruction as A , the excess energy is obtained. Table 4.5 contains the tabulated energies of each low energy surface on GdScO_3 , with separations between the $(100)_{pc}$ double layers, $(100)_{pc}$ single layer, and $(110)_{pc}$ reconstructions as they are not directly comparable due to their differing chemistries via calculated energy alone. The density of excess Sc_2O_3 is also given.

Table 4.5. Excess surface energies of the LnScO_3 surface reconstructions discussed in this chapter and the (110) double layer from Chapter 3, along with the areal density of excess scandium at the surface.

Structure	Excess energy (J/m ²)	Excess Sc_2O_3 units per nm ²
(110) double layer	2.40	6.25
(001) double layer	2.15	6.26
(110) single layer	1.92	1.56
(010)	1.91	4.32
(100)	2.14	4.33
(112)	1.92	4.42

$$(4.2) \quad E_{surf} = \frac{E_{slab} - n_{LnScO_3} E_{LnScO_3} - m_{Sc_2O_3} E_{Sc_2O_3} + m_{Sc_2O_3} \Delta\mu_{Sc_2O_3}}{2A}$$

In order to generate theoretical Wulff shapes for GdScO_3 (the material used in the calculations) using surfaces with varying amounts of excess Sc_2O_3 , a chemical potential term is added to Equation 4.2 as in Equation 4.1. The value of $\Delta\mu_{Sc_2O_3}$ is not directly

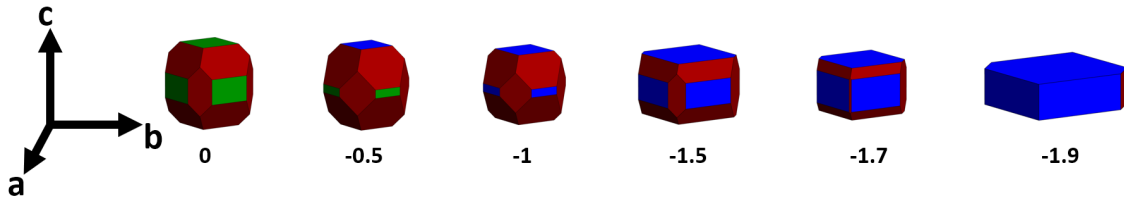


Figure 4.13. Calculated Wulff shapes of GdScO_3 for different values of $\Delta\mu_{\text{Sc}_2\text{O}_3}$. The value of $\Delta\mu_{\text{Sc}_2\text{O}_3}$ is printed under each construction in units of $\text{eV}/\text{Sc}_2\text{O}_3$, and the orientation of the constructions is given by the axes on the left. Facets are colored by their pseudocubic designations, with the $\Delta\mu_{\text{Sc}_2\text{O}_3}$ single layer surfaces in green, the $\{100\}_{pc}$ double layer surfaces in blue, and the $\{110\}_{pc}$ single layer surface in red. As no specific calculation was performed for the (001) single layer termination, it was approximated using the energy of the (110) single layer.

attainable from these calculations and is largely dependent on synthesis conditions; therefore, theoretical Wulff shapes for GdScO_3 are plotted in Figure 4.13 for a range of chemical potentials. As seen, the particles become more rectangular than rhombohedral as $\Delta\mu_{\text{Sc}_2\text{O}_3}$ increases, and at very low values of $\Delta\mu_{\text{Sc}_2\text{O}_3}$ the single layer termination on the $\{100\}_{pc}$ surfaces is preferred to the double layer. These shapes can be compared to imaging of the synthesized particles to determine the value of $\Delta\mu_{\text{Sc}_2\text{O}_3}$ during synthesis, and this is discussed in Chapter 9 Section 9.5.

4.6. Conclusions

Sc-rich surface terminations were found on all exposed facets of the hydro-sauna synthesized LnScO_3 nanoparticles. A majority of the exposed surface area consists of a double layer termination on $\{100\}_{pc}$ planes. Single layer terminations with O vacancies are also present both in small areas of the $\{100\}_{pc}$ surfaces as well as at the particle edges on $\{110\}_{pc}$ surfaces.

CHAPTER 5

Thermodynamics of Supported Polycrystals - a Modified Winterbottom Construction

5.1. Introduction

The Wulff construction [27–29], and by extension the Winterbottom construction [31], are indispensable tools for the analysis of nanoparticle shapes and thermodynamic energies. To briefly summarize, the thermodynamic Wulff construction describes the shape that a single crystal particle of a given material will take to minimize its overall surface energy considering the differing surface energies of various facets. This is described by the following expression [94–96]:

$$(5.1) \quad S = x : x \cdot \hat{n} \leq \lambda\gamma(\hat{n})$$

stating the thermodynamic shape of a nanoparticle is all points x within $\hat{n} \leq \lambda\gamma(\hat{n})$, where \hat{n} is the unit vector defined by a given crystallographic orientation, $\gamma(\hat{n})$ is the surface free energy in that orientation, and λ is a constant related to the particle volume. In practice this construction is generated by plotting the surface free energies in all directions and taking the inner envelope of the radially normal planes.

This thermodynamic model forms the backbone of many related models for nanoparticle energetics and growth shapes. For example, if one moves away from the thermodynamic limit towards a kinetic regime, the surface free energies are replaced with the

growth velocities of the respective surfaces. Similar to the way that high energy facets will fall outside of the inner envelope of the solution, surfaces with rapid growth velocities will annihilate during growth. It is worth noting that the original work by George Wulff [27] falls into the category of kinetically controlled growth, though the thermodynamic variant of the model is often simply called the “Wulff construction” today.

Nanoparticles are not always freestanding, so a variation to this model was introduced by Winterbottom in 1967 in which a nanoparticle is supported on a foreign substrate [31]. In this construction, the free energy of the interface is treated similarly to the free energy of a surface in the thermodynamic Wulff construction. The distance from the Wulff center to the interface is therefore determined by the energy of that interface, and experimentally measuring these distances is a common method for assessing these thermodynamic energy of an interface.

Nanoparticles are also not necessarily single crystals, and another variant is the modified Wulff Construction formulated by Marks [97–99], where twin boundaries are introduced to the Wulff construction to model the shapes of both lamellar and multiply twinned particles. This is somewhat similar to the Winterbottom construction in that the surface energy in a given direction is replaced with the energy of the interface that is formed, however it also considers the crystallographic constraints of twin formation as well as multiple constituent crystallites. Put simply, the modified Wulff construction can be considered the sum of the Wulff constructions of the different crystallites forming the nanoparticle, each bound by external surfaces and twin boundaries. An example of such a constituent crystallite for a 5-fold MTP can be found in Figure 5.1, crystallite I.

In addition to twin structures, nanoparticles can adopt core-shell [100], Janus-type [101, 102], and many more geometries; in fact there is a significant body of papers devoted to synthesizing various nanoparticle morphologies and attempting to apply these new shapes, some of which are cited here [103–114]. The thermodynamics of these various morphologies are well-studied for freestanding nanoparticles [30, 96–99, 115], but many practical applications of nanoparticles require stabilization with a supporting substrate [11, 116–121]. While the Winterbottom construction adequately describes supported single crystals, there is a notable gap in established theory considering the thermodynamics of polycrystalline morphologies adhered to a support.

In this chapter, I will describe a theoretical model that can be applied to describe the thermodynamics of a supported polycrystalline nanoparticle using an example of a 5-fold decahedral MTP. I will then discuss the sensitivity of the overall results to changing parameters. Finally, I show experimental cases from my research and already published results that serve to exemplify various aspects of this model.

5.2. Theory

This model expands upon its predecessors through the introduction of the term γ_{eff} , the effective interfacial energy of the polycrystalline particle. Each of the constituent crystallites has a different orientation, and therefore the local interfacial energy will vary. γ_{eff} is introduced as the area weighted average of the energies of n crystallites such that $\gamma_{eff}(h) = \sum_{i=1}^n f_i(h)\gamma_i$, where f_i is the areal fraction of that crystallite at the interface ($f_i(h) = \frac{A_i(h)}{\sum_{i=1}^n A_i(h)}$, A_i is the interfacial area of crystallite i). The height dependence, (h) , is introduced owing to the changing interfacial area as a function of the particle

height. Because the interface consists of multiple crystallites at different orientations, the adhesion energy of the polycrystal will be greater than that of an equivalent single crystal, provided that multiple unique crystallites in the polycrystal contribute to the interface. While a single crystal can pick the absolute best orientation to minimize the energy, the presence of at least one more contributing orientation in the polycrystal makes that absolute minimization impossible.

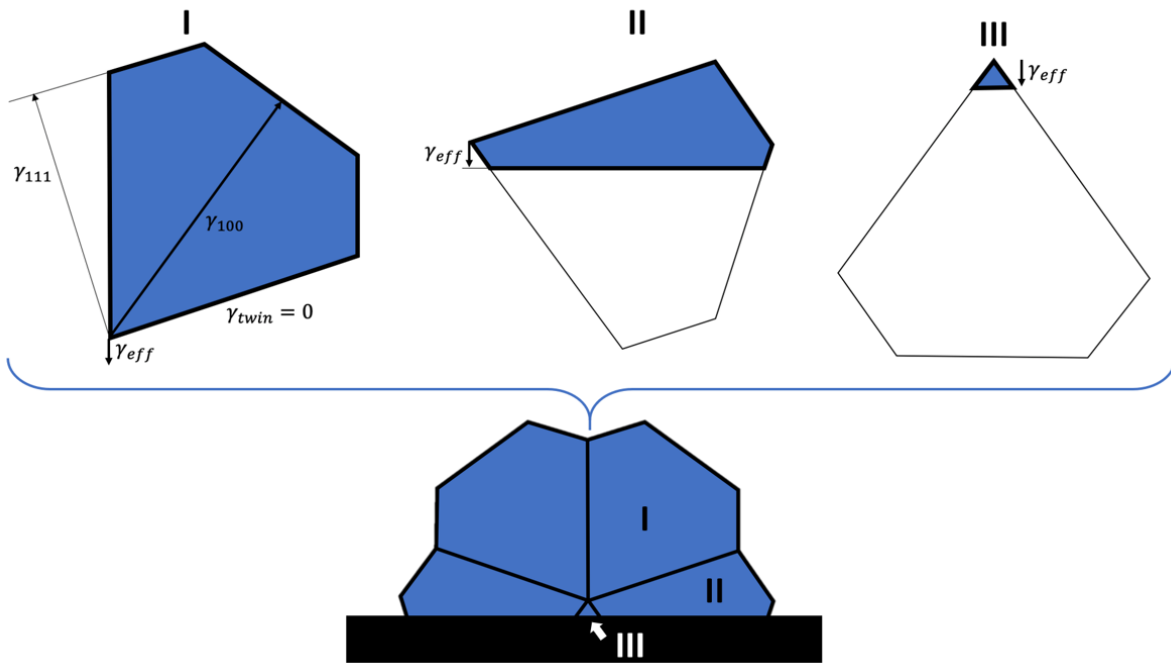


Figure 5.1. The modified Winterbottom construction for a 5-fold MTP viewed along the $[110]$ direction. Crystallite I is unaffected by the presence of the interface as a result of its orientation. The twin boundary energy is set to zero resulting in the boundaries intersecting with the Wulff center. Crystallites II and III are affected by the interface to form the morphology pictured.

The model is generated through the combination of the Winterbottom [31] and Modified Wulff [97–99] constructions, as highlighted in Figure 5.1. Using a 5-fold geometry, a

freestanding MTP would be modeled using 5 copies of crystallite I appropriately rotated and combined. When a support is introduced with an interfacial energy of γ_{eff} , the Wulff shapes of the different crystallites are changed. Though the crystallites are initially identical in shape, they have different orientations relative to the substrate and will therefore be affected by the interfacial energy as demonstrated. In the example in Figure 5.1, this generates 3 unique crystallite shapes (I, II, and III).

The single crystal Winterbottom construction dictates that a particle's energy is minimized when the truncation height of that particle in the construction is coincident with the interfacial energy. To clarify, consider the term γ_h as the distance from the Wulff center to the interface; the total energy is minimized when $\gamma(\hat{n}) = \gamma_h$ (this is the sole solution of the single crystalline Winterbottom construction). This condition also holds in the polycrystalline model, where $\gamma_{eff}(h) = \gamma_h$ represents a sufficient condition for a minima in the overall free energy of the particle. However this not the only sufficient condition for polycrystals, and other minima will arise in the 5-fold example. The use of γ_{eff} in each crystallite in lieu of γ_i is mathematically justified and demonstrated as a condition for a minima in Appendices A and B.

As another consideration, two inverted orientations of the nanoparticle need to be calculated for each possible interfacial orientation. For the interfacial orientation in Figure 5.1, the particle can form as drawn or with crystallite type III above the interface and type I below. These geometries are seen experimentally in Au nanoparticles in Figure 5.2. This consideration is not necessary in a single crystal Winterbottom construction provided the material contains inversion symmetry, but the anisotropy of the MTP requires it. To

determine the low energy configuration for any given interface, both orientations are assessed and their relative energies are compared.

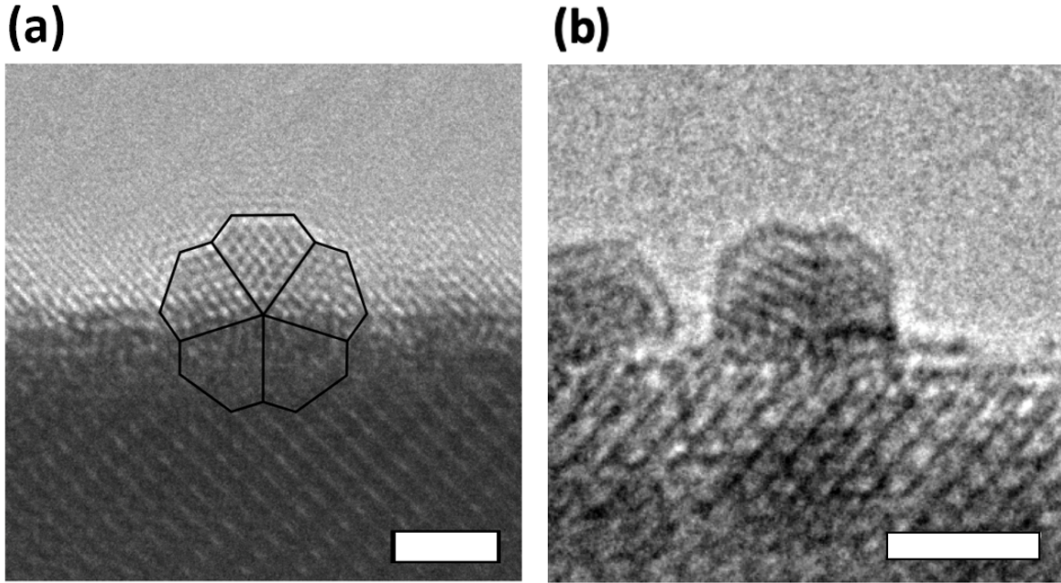


Figure 5.2. Experimental images of supported 5-fold MTPs with (b) matching the orientation in Figure 5.1. These morphologies represent both possible orientations for a supported nanoparticle with this particular interfacial orientation.

A metric is needed to evaluate the relative energies of different morphologies or particle heights, and I will now introduce the term ϵ_w from the original Modified Wulff construction [97–99]. This volume-independent parameter is a measure of the excess surface energy of a particle and can be used to compare the energetics of the supported particles at different heights or orientations. This term is written as:

$$(5.2) \quad \epsilon_w(h) = \frac{1}{\gamma_{111}} \frac{\int \gamma(\hat{n}) dA(h)}{(\int dV(h))^{2/3}}$$

where V is the particle volume, A is the area of the surface or interface in direction \hat{n} , and γ_{111} is the surface energy of the (111) surface of the material and serves as a normalization constant. Adding an interface here results in $\gamma(\hat{n}) = \gamma_{eff}(h)$ (importantly, $\gamma_{eff}(h)$ does not necessarily equal γ_h) in the direction of said interface representing the interfacial energy rather than the surface energy. The full equation for ϵ_w includes terms for the twin boundary energies as well as a coupling term, but specific calculations show these contributions to be small and in most FCC metals the twin boundary energy is negligible.

By calculating ϵ_w as a function of height, one can assess the excess energy of the nanoparticle and determine the geometry of the thermodynamic minimum. Furthermore, the shape of the $\epsilon_w(h)$ curve can yield insights to the overall energetic landscape of the particle revealing possible metastable states or local minima that can arise. I will walk through the application of this model to the 5-fold MTP geometry in Figure 5.1 in the following sections to exemplify these concepts.

5.3. 5-fold Example

The calculation of ϵ_w for any supported polycrystal requires knowledge of the volume, the surface area and energy of each facet, and γ_{eff} as a function of height. For this example, I use a broken bond model for the surface energies such that $\gamma_{100} = \frac{2}{\sqrt{3}\gamma_{111}}$ and assume a strong faceting limit where only the (100) and (111) planes are exposed as in Figure 5.1. This condition results in reentrant surfaces at the twin boundaries and this morphology is commonly called the Marks decahedron. These parameters determine the external shape of the particle which in turn determines the exposed surface areas and volume. The geometric analysis was performed using the Mathematica software package

for determination of the interfacial areas, surface areas, and volumes of the crystallites as they change with height. Finally I choose arbitrary interfacial energies for crystallites I, II and III (as defined in Figure 5.1) of 0.1, 0.2, and 0.3 times γ_{111} respectively. I will return to discuss these arbitrary values in Section 5.4.

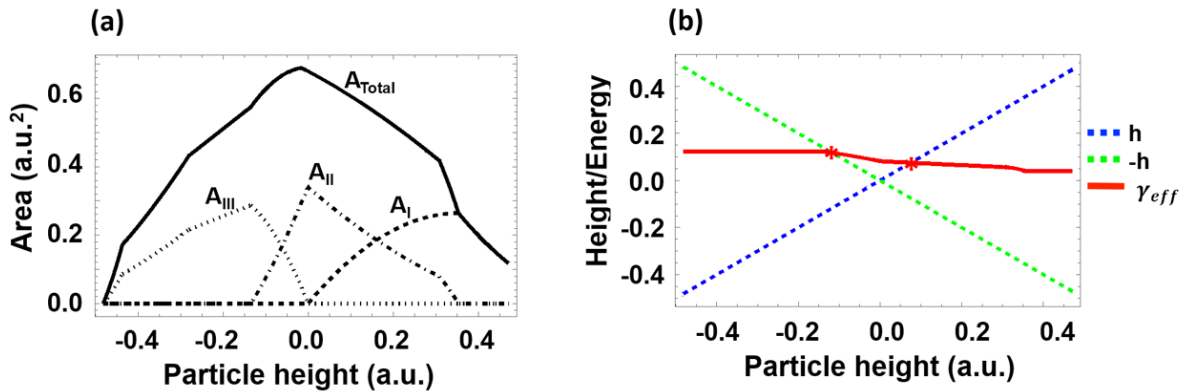


Figure 5.3. The partial contribution of each crystallite towards the total area is calculated in (a) (note that A_{II} and A_{III} are double counted towards the total area since there are two of each crystallite type). The effective interfacial energy, γ_{eff} , is shown in (b), given the assumptions in the text. Overlaid on (b) are the particle heights for each orientation, and the marked intersections are where $\gamma_{eff}(h) = \gamma_h$.

The calculation of γ_{eff} is demonstrated in Figure 5.3, where 5.3a shows the areal contribution of each crystallite to the total interfacial area, and 5.3b has the resulting energy given the parameters listed in the previous paragraph. The heights of the two competing orientations of the nanoparticle are plotted against γ_{eff} . The dotted lines are representative of the condition where the interfacial energy is exactly proportional to the height (discussed earlier as γ_h), and the intersections of these with γ_{eff} are minima in the energy of these particle morphologies.

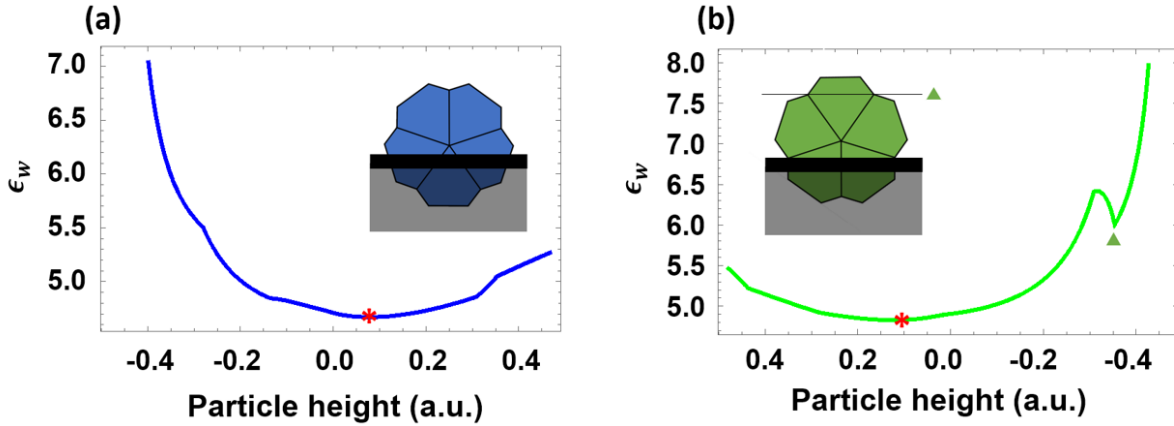


Figure 5.4. ϵ_w plots for each orientation of the 5-fold MTP along with a schematic demonstrating the particles' morphology and truncation height. The minimum values (marked in red) can be compared with the experimental images in Figure 5.2. There is a local minima marked with a green triangle in (b). Also note the direction of the x axis in (b).

Calculating the volume independent excess surface energy, ϵ_w , for these morphologies yields the results in Figure 5.4, with the absolute minimum values marked in red. These minima coincide with the intersections of γ_{eff} and γ_h in Figure 5.3b as expected from the theory. Comparing the ϵ_w values at each point gives a value of 4.67 and 4.83 for (a) and (b) respectively, indicating that the orientation in (a) is the low energy solution for the system. In addition to these global minima, a local minima is observed in (b) as indicated by the green triangle. This occurs at a discontinuity in the geometry where the interface moves from existing in one crystallite to 3. In a purely thermodynamic system only the solution in Figure 5.4a would exist, however most experimental systems are formed, to some degree, by a combination of thermodynamic and kinetic processes such that the geometries at local minima and the orientation in (b) may be observed.

5.4. Sensitivity to Changing Parameters and Kinetics

Here I return to the assumptions made in the previous model for the surface energies (and therefore particle shape) as well as the arbitrary selections for the interfacial energies to explore the sensitivity of adjusting these parameters. To begin with the surface energies and particle shape, Figure 5.5 shows the results of ϵ_w calculations for particles where $\gamma(\hat{n}) = 1$ and where $\gamma_{100} = \frac{\sqrt{3}}{2}\gamma_{111}$. The former is a spherical, isotropic particle with internal twin boundaries, and the latter is the condition in which the notches disappear at the ends of the twin boundaries in the Marks decahedron used in the previous section. Both morphologies are pictured in Figure 5.5. For crystallites I, II, and III, the interfacial energies for the spherical particle are 0.1, 0.2, and 0.3 and the faceted particle has those energies adjusted to 0.3, 0.4, and 0.5 times γ_{100} since this is now the lowest energy surface.

As seen, the overall shapes of the curves and positions of the minima are similar to the results presented in Figure 5.4 with a few differences arising from the shape changes. Most notable is the disappearance of the local minima near -0.4 in Figure 5.4b, since this feature arose from the discontinuity introduced by the reentrant surfaces. In these examples, the transition from 1 to 3 crystallites at the interface is either smooth (isotropic particle, Figure 5.5b), or does not exist (pentagonal particle, Figure 5.5d). Another difference appears in Figure 5.5d, where another minima appears at the origin in addition to the one near 0.2 (where $\gamma_{eff}(h) = \gamma_h$) and has a smaller excess energy, making it the overall solution for this orientation. As with the local minima in Figure 5.4b, this occurs at a transition between crystallites. The fact that this minima is lower in energy than the minima near 0.2 is a result of the arbitrary selection of interfacial energies. At the local

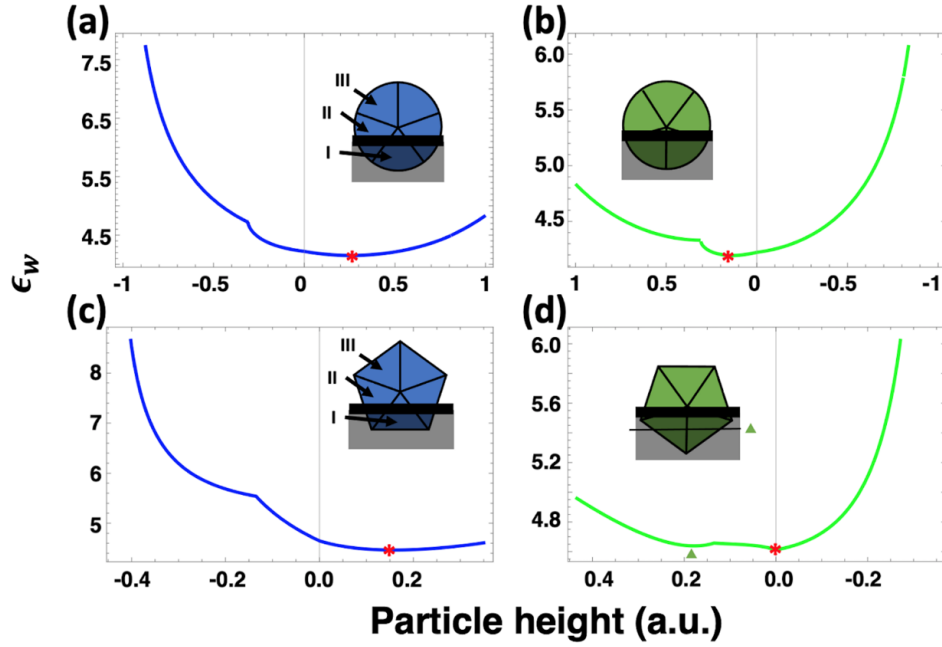


Figure 5.5. ϵ_w plots for different MTP geometries are given for a particle with isotropic surface energy (a/b) and with no reentrant surfaces (c/d). Absolute minima are marked in red and local minima with a green triangle.

minima near 0.2, the interface is purely formed with crystallite type III, which I assigned the highest interfacial energy to ($0.5\gamma_{100}$). This is in contrast to the interface at the origin which is comprised of crystallite II which has a lower interfacial energy.

To explore the sensitivity of the model to changing these interfacial energy values, I return to the original particle shape (Figures 5.1, 5.3, and 5.4) and now adjust the interfacial energies. If the interfacial energies are changed to -0.2, 0.4, and 0.7 times γ_{111} for crystallites I, II, and III respectively, the ϵ_w curves change significantly as shown in Figure 5.6. This change results in a greater impact to the energy landscape and the resulting degree of truncation of these particles compared to changing the surface energies. This indicates that minimizing the interfacial energies is thermodynamically

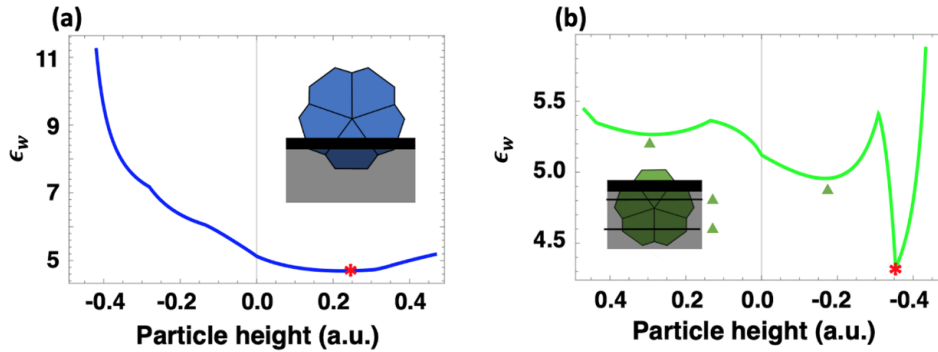


Figure 5.6. ϵ_w plots for an MTP with adjusted interfacial energies. This results in more significant changes than those seen in Figure 5.5, introducing more local minima and changing the location of the global minimum to a greater degree than changing the external energies.

more significant in determining adhesion and, in order to minimize their total energies, supported nanoparticles will tend to form morphologies that minimize the energy of the interface.

As a brief, but important, aside I will discuss kinetics. This thermodynamic model can be considered in the kinetic regime, where surface/interfacial free energies are replaced with growth velocities in each direction [27,96]. In a purely kinetic limit, the Wulff center of the particle will always be coincident with the interface because the growth velocity of the interface is necessarily zero. However this is rarely the case, instead a mix of both kinetic and thermodynamic factors tends to be present in experiment. This will instead result in particles potentially occupying local minima in the energy landscape and/or moving the Wulff center closer to the interface than pure thermodynamics would predict.

5.5. Experimental Observation

The minimization of the interfacial energy, along with other predictions from the model such as local minima, can be observed in experimentally prepared nanoparticles in both

the materials studied in this dissertation as well as in external literature. Beyond the examples in Figure 5.2, which have degrees of truncation similar to those predicted by the model in Figure 5.4, the subsequent figures exemplify different mechanisms by which nanoparticles can minimize their interfacial energy.

In the absence of a strong epitaxial relationship, the lowest energy interface between an FCC metal and an arbitrary substrate is generated using the (111) plane of the metal, as it has the lowest surface energy (this is discussed further in Chapters 6 and 8). Therefore one would expect to see the (111) plane of the metal particle forming the interface. Figures 5.7 through 5.10 all show examples of this behavior, with specifics discussed in the figure captions.

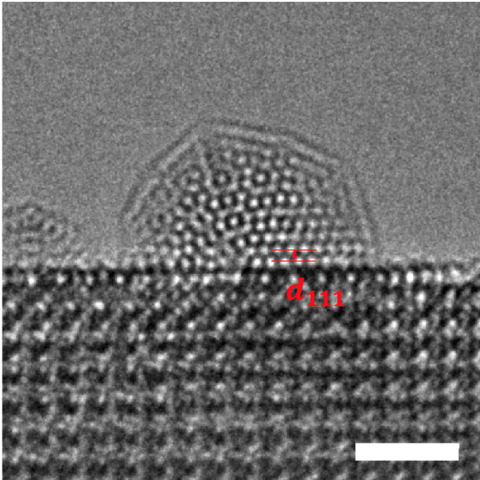


Figure 5.7. An aberration corrected HREM image of a supported icosahedral MTP of Au on GdScO₃. As highlighted in the image, the particle orients such that the (111) plane is at the interface.

Kinetic influences and local minima are also observed experimentally, and this is demonstrated by Figure 5.11. Both particles sit at significantly different heights with respect to their degree of truncation, where the Wulff center is highlighted by a red star

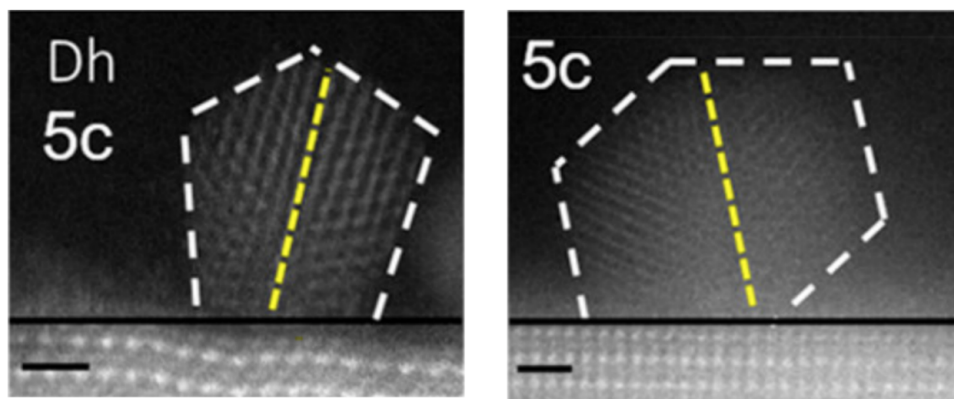


Figure 5.8. Aberration corrected HAADF images of 5-fold MTPs of Pd on SrTiO₃. The yellow lines indicate the 5-fold axis. These morphologies are indicative of the particle axis tilting into or out of the plane of the page [4,5], and by doing so the (111) surface can make contact with the support. Scale bars are 1 nm. Reprinted with permission from [6]. Copyright (2018) American Chemical Society.

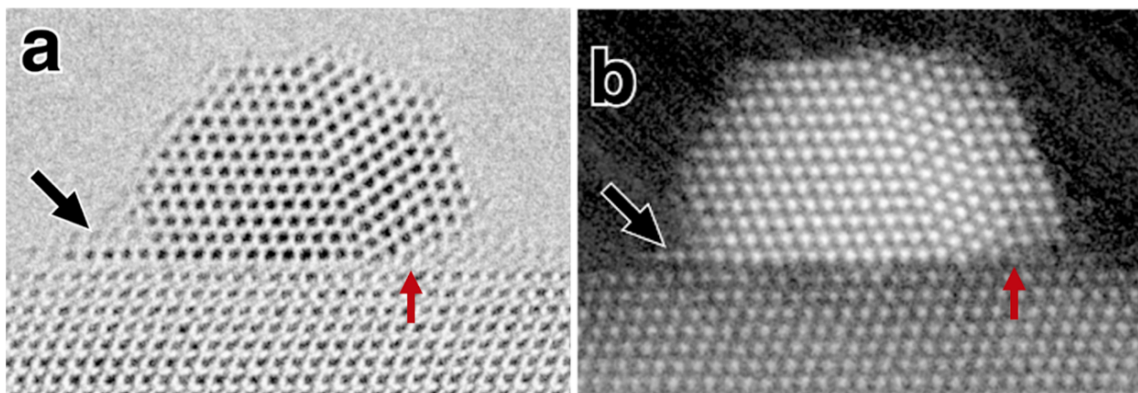


Figure 5.9. Bright field (a) and HAADF (b) of a twinned Au particle supported on NiO with a surface step indicated by the red arrow. The twin boundaries in the Au allow the (111) planes to maintain contact with the surface over the step. Reprinted with permission from [7]. Copyright (2018) American Chemical Society.

on the particle on the right and the Wulff construction of a particle with the [111] orientation is overlaid on the left. The left particle sits exactly at a discontinuity in the faceting

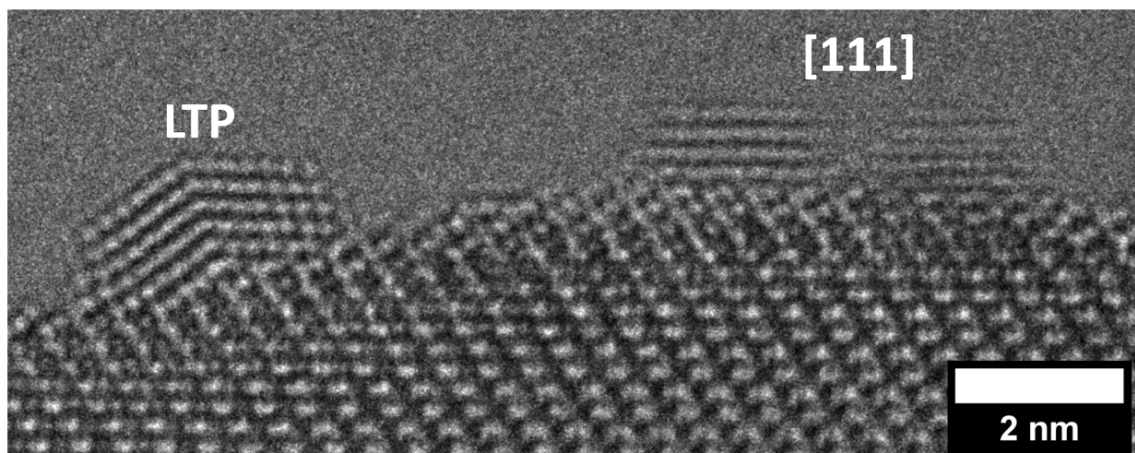


Figure 5.10. A LTP of Pt on a rough surface of LaScO_3 is observed on the left, with two single crystal $[111]$ type particles on the right. The twinning of the LTP owing to the surface step results in the (111) surface forming the majority of the interfacial area despite the rough LaScO_3 surface.

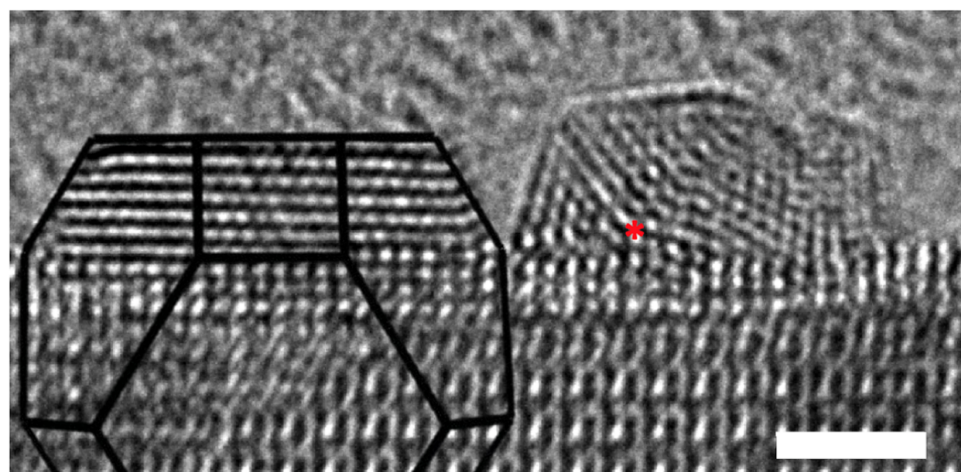


Figure 5.11. Aberration corrected HRTEM of supported Au nanoparticles showing a single crystal (left) and a MTP (right) at significantly different truncation heights. The Wulff center is marked on the right and the overall Wulff construction is overlaid on the left. The greater relative height of the MTP indicates a smaller adhesion energy, and there is suggestion of kinetic influence in the formation of the particles.

where the right has the Wulff center very close to the interface, where it would be in a kinetic particle as discussed in the previous section.

5.6. Conclusions

A thermodynamic model to predict the shape of supported polycrystalline particles has been described, combining the Winterbottom and Modified Wulff constructions. This model can be extrapolated to any supported polycrystal provided knowledge of the surface and interfacial energies, and conclusions drawn from the presented examples can be observed experimentally.

The material in this chapter has been published in [122].

CHAPTER 6

Au Morphologies and Interfaces on LnScO₃**6.1. Introduction**

In Chapter 7, the Au/LnScO₃ materials are used to catalyze CO oxidation, but to understand the behavior of Au in that catalytic reaction we first need knowledge of the Au nanoparticle shapes and the thermodynamic properties on the supports. Previous work studying Pt on SrTiO₃ and (Ba,Sr)TiO₃ found that changes to the adhesion energy of the Pt nanoparticles owing to the strain mismatch between the metal and the substrate affected the Pt truncation height, and suggested that this change influenced the geometry of the active site, changing the selectivity of acrolein hydrogenation [11]. To identify the origins of any differences in catalytic performance stemming from the different supports in the Au/LnScO₃ system, it is relevant that Au nanoparticles are characterized in detail to confirm the presence, or absence, of changes to their thermodynamic properties on the LnScO₃ supports.

In this chapter, I discuss the deposition and morphologies of Au on the support materials. The interfacial strain mismatch is found to drive changes to the distribution of Au nanoparticle morphologies and orientations; however, the adhesion energy of the Au is relatively constant leading to interfacial sites of similar geometry on each support.

6.2. Methods

Au nanoparticles were deposited on the LnScO_3 supports using a deposition precipitation reaction performed by A. Gosavi and based upon the procedure outlined by Zanella *et al.* [123]. The Au precursor used was chloroauric acid (HAuCl_4) in solution with urea in a 10:1 molar ratio of urea to Au. Bare LnScO_3 nanoparticles were added and the solution was held at 80 °C for 16 hours. During this time the urea decomposes which drives the pH of the solution up, causing $\text{Au}(\text{OH})_3$ to precipitate and deposit on the LnScO_3 surfaces. The solid product was collected via centrifugation and washed with deionized water before being dried at 80 °C in flowing N_2 , resulting in metallic Au nanoparticles decorating the LnScO_3 . The result of a typical deposition of Au on LnScO_3 is pictured in Figure 6.1.

The crystallinity and morphology of the supported Au nanoparticles were determined using HREM with either a JEOL ARM300F at Northwestern University operated at 300 kV, the ACAT operated at 200 kV, a JEOL 2100 at Northwestern University operated at 200 kV, or a FEI Talos at Argonne National Laboratory operated at 200 kV. At the time of these characterization experiments, the available support materials were primarily LaScO_3 , NdScO_3 , and GdScO_3 . As the synthesis method was refined by collaborators, SmScO_3 replaced GdScO_3 as one of the major products and was used for the future catalytic experiments. While the particle adhesion energy on SmScO_3 was assessed, a detailed study of the morphological distribution was not performed.

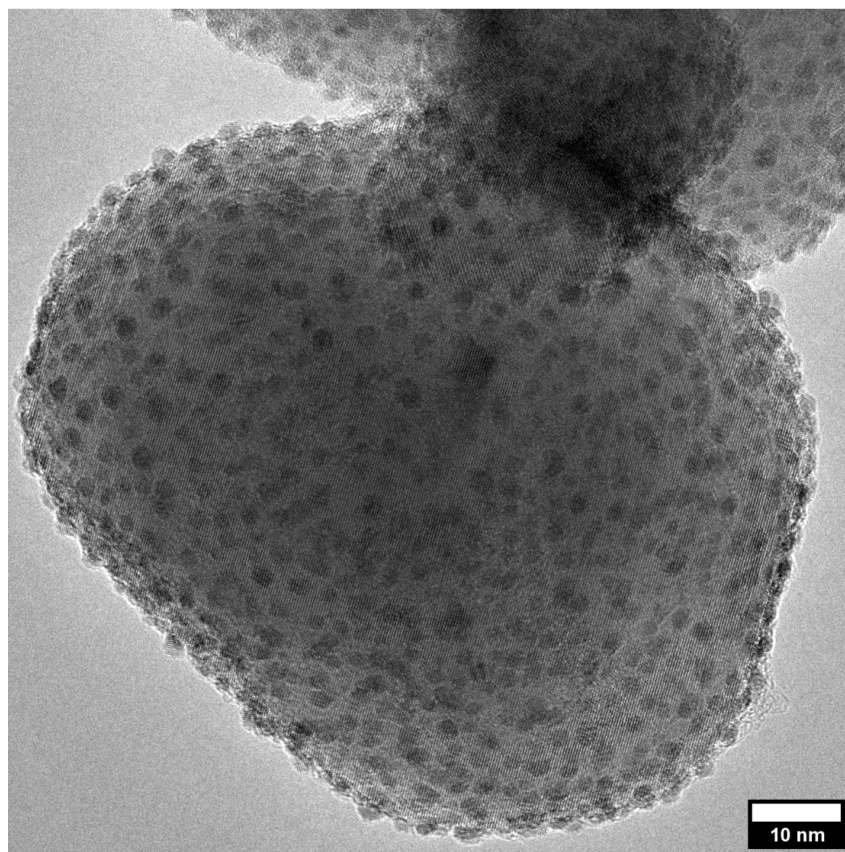


Figure 6.1. Au deposited on LaScO_3 via deposition precipitation.

6.3. Results

Following deposition of Au on the LnScO_3 supports, three principal types of Au nanoparticles were observed: single crystals with the $[110]$ direction normal to the support, single crystals with the $[111]$ direction normal to the support, and twinned particles. These different morphologies coexist on a given support following synthesis, albeit in different proportions on the different LnScO_3 materials. I hypothesize that the presence of these particle morphologies, and their relative population of on each support, can be

rationalized by strain mismatch, the lattice contraction of small metal nanoparticles, and interfacial energies.

6.3.1. Single Crystal Particles - [110] and [111] type

A vast majority of the single crystal Au particles adopt one of two orientations on the faceted support surfaces; defining the particles by the crystallographic direction normal to the support surface, the single crystal particles are typically either [110] or [111] type. Additionally, these particles have preferred orientations on the support $(100)_{pc}$ surfaces with respect to their rotation about the surface normal. The [111] type particles have the Au [110] and [112] directions aligning with the pseudocubic [100] direction on the support, and for the [110] type particles the [100] and [110] Au directions align. Figure 6.2 contains HREM of supported Au single crystals viewed along a $[100]_{pc}$ direction of the support, and this preferred orientation is clearly observed in the outlined particles.

6.3.2. Twinned Particles

Twinned nanoparticles can either be multiply twinned particles (MTPs) or lamellar twinned particles (LTPs). At small sizes, forming MTPs is energetically favorable for many FCC metals owing to the reduction in overall surface energy [96, 124, 125]. These particles are energetically favorable at smaller sizes because MTP geometries minimize the excess surface energy of the nanoparticles, however internal tensile strain causes MTPs to become less energetically favorable at larger volumes. This strain is present because the constituent crystallites of both icosahedral and decahedral MTPs are not completely space filling and require either strain or structural modification to form closed

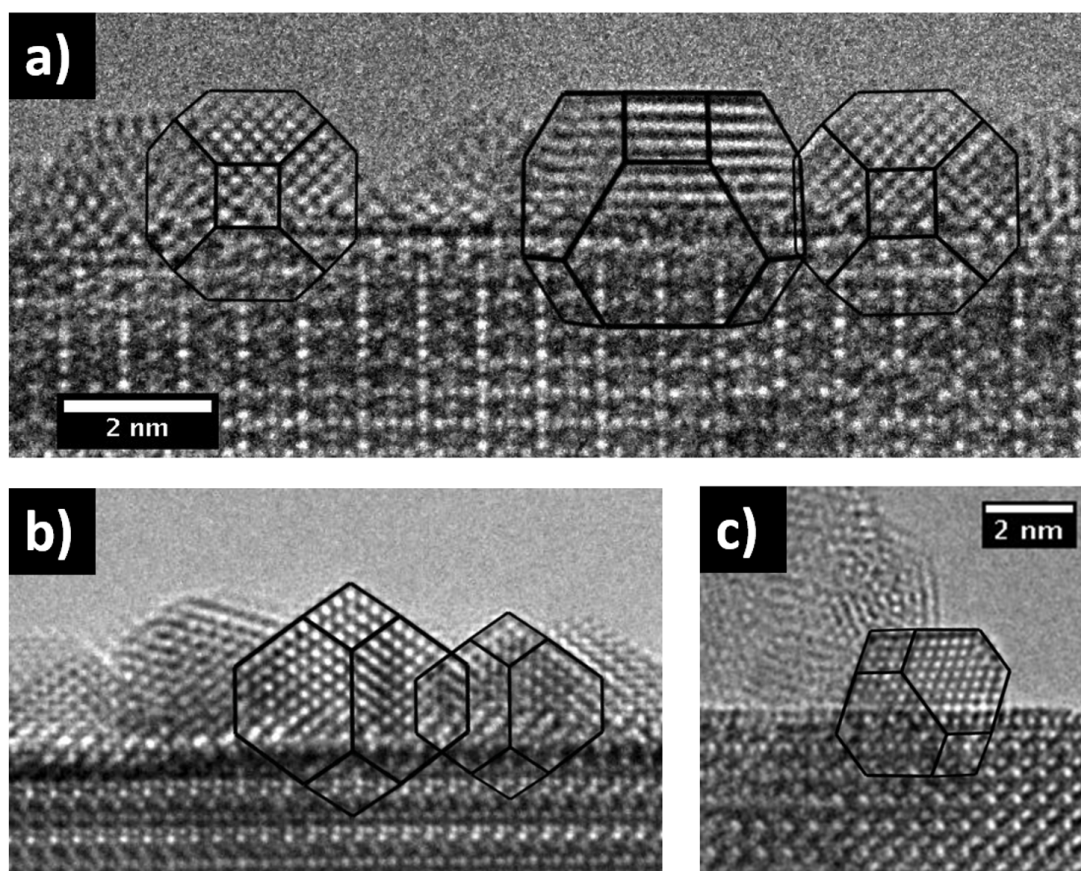


Figure 6.2. The different orientations of single crystals observed on the $(100)_{pc}$ support surfaces are pictured above. The support material in (a) and (b) is NdScO_3 , while GdScO_3 is shown in (c). In (a) the particles on the left and right are $[110]$ type particles viewed along the $[100]$ direction and the central particle is a $[111]$ type particle viewed along the $[112]$ direction of the Au. The particles in (b) are $[110]$ type particle viewed along the $[110]$ direction, and the particle in (c) is a $[111]$ type particle viewed along the $[110]$ direction.

shapes [96, 99, 124, 126–130]. The supported MTPs observed herein come in multiple geometries including truncated icosahedra and decahedra as pictured in the previous chapter (Chapter 5, Figure 5.7 and Figure 5.2 for icosahedra and decahedra respectively).

Turning to LTPs, these particles are energetically more like single crystals with stacking faults than they are to MTPs as the twin boundaries do not introduce internal strain or significantly affect the excess surface energy of the particle. Though energetically similar to single crystals when freestanding, supported LTP geometries on substrate steps can reduce their interfacial by allowing a larger area of the (111) plane (the close-packed plane in an FCC material) to be in contact with a stepped or curved surface, as discussed in Chapter 5, Section 5.5 Figures 5.9 and 5.10. Despite this potential for energetic minimization, I hypothesize that the LTPs represent a small fraction of the twinned particles counted for three reasons: 1) MTPs are energetically favored at small sizes, (2) the supports are well-faceted, and (3) most of the twinned particles observed were hemispherical in shape, which are indicative of icosahedral MTPs.

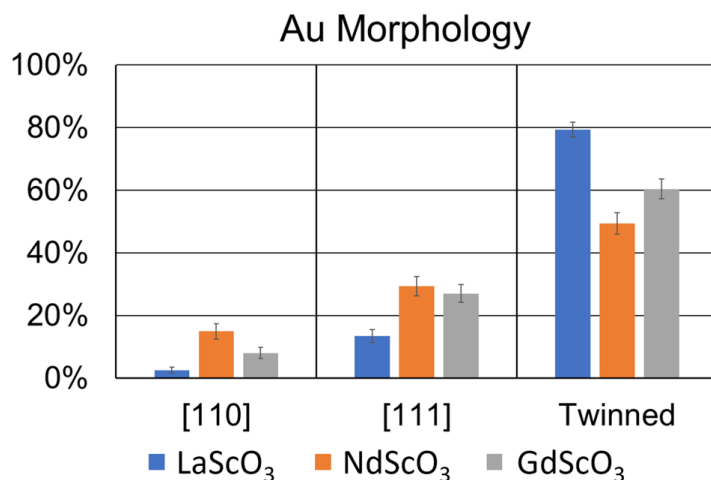


Figure 6.3. Proportions of the three major morphologies of Au observed on different LnScO₃ supports. Over 200 particles were counted on each support and error bars show the standard error of the proportion.

Figure 6.3 shows the relative populations of each Au morphology on the LnScO₃ supports, and it should be noted that the twinned particles are not delineated between

MTPs and LTPs. This is due to the difficulty in confidently determining the exact twin geometry in many of the nanoparticle images, though it is rather straightforward to identify particles that do not adopt a single crystal Wulff shape, as demonstrated in Figure 6.4.

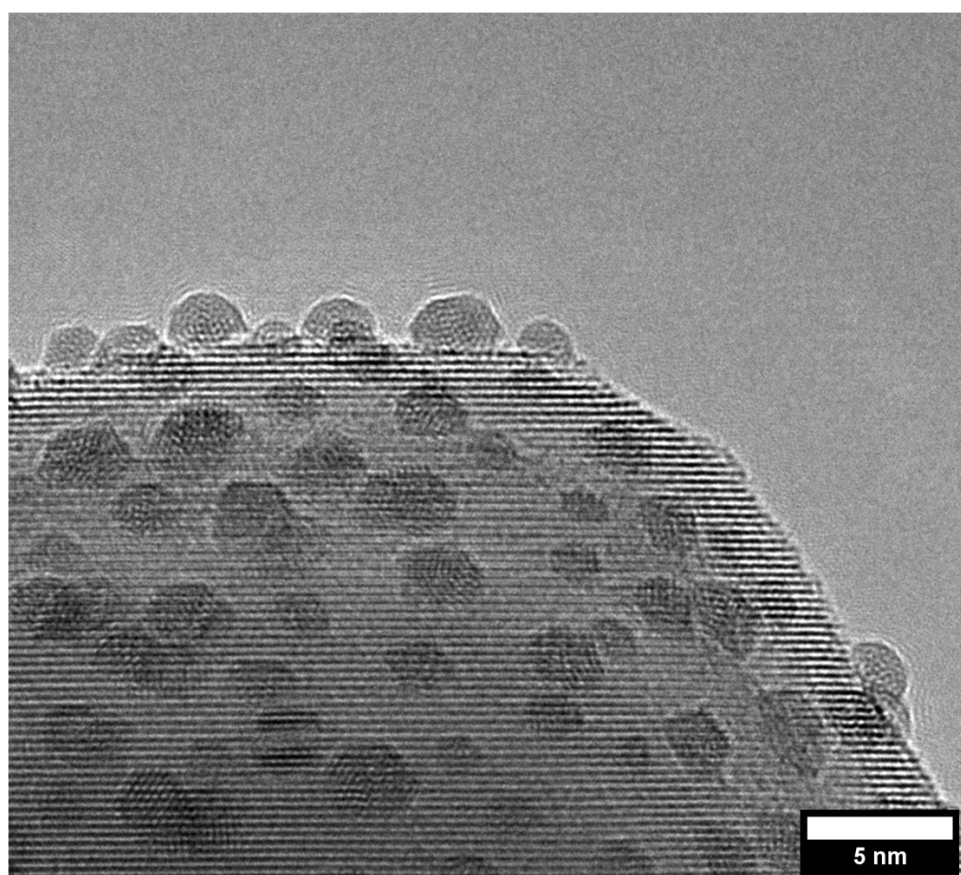


Figure 6.4. . Twinned Au supported on LaScO_3 . Many of the particles observed are hemispherical in shape rather than sharply faceted single crystals, and those with facets do not conform to expected single crystalline shapes.

6.3.3. Dependence of Au Adhesion Energy and Morphology on the Support Material

The Winterbottom construction was introduced in Chapter 5 as a tool to assess the total interfacial energy of a nanoparticle on a surface, and Equation 6.1 is a convenient way to break that overall interfacial energy down into its individual components in the Au/LnScO₃ system:

$$(6.1) \quad \gamma_I = \gamma_{Au} + \gamma_{LnScO_3} + \gamma_{bond}$$

where γ_I is the total interfacial energy, γ_{Au} is the energy of the Au surface forming the interface, γ_{LnScO_3} is the surface energy of the support, and γ_{bond} is a negative bonding term resulting from the formation of bonds between the two surfaces. This bonding term is affected by factors such as epitaxy, strain mismatch, and the ability of neighboring atoms at the interface to form chemical bonds.

In Figure 6.2a, [110] and [111] type particles sit next to each other on the same NdScO₃ surface and have a similar height to width ratio, implying a similar interfacial free energy from the Winterbottom construction [31]. Considering the γ_{Au} term, calculated surface energies of the (110) and (111) surfaces [131] differ by a factor of 1.29 ($\gamma_{110} = 1.29\gamma_{111}$) necessitating a larger negative contribution from the bonding term for the [110] type particles to have equal interfacial energies. Though each of these particles has a similar overall interfacial energy, γ_I , the mechanisms by which each are stabilized are different: the [111] type is stabilized by the lower energy of the (111) surface while the [110] type is stabilized by a larger negative γ_{bond} term. For a direct comparison of interfacial energies

across the various LnScO_3 supports, including SmScO_3 , [111] type particles are shown in Figure 6.5 and demonstrate no significant change in Au adhesion energy. The γ_{bond} term for the [111] type particles remains relatively constant despite changes to the strain mismatch.

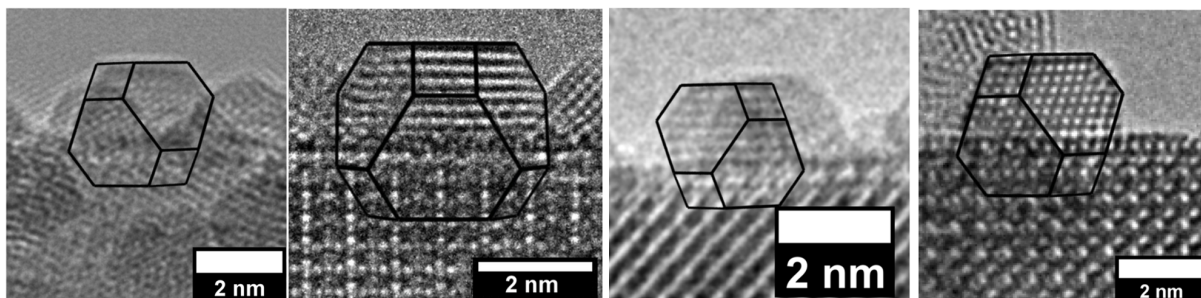


Figure 6.5. A comparison of [111] type Au particles on LaScO_3 , NdScO_3 , SmScO_3 , and GdScO_3 (left to right). All particles have a similar degree of truncation as demonstrated by the overlaid Wulff shapes.

Before discussing the trends in Au morphologies on the different supports (Figure 6.3), the nanoparticle lattice contraction must first be discussed. Due to the high surface-to-volume ratio in nanoparticles, the intrinsic surface stress (i.e. the derivative of the surface free energy with respect to strain in the plane of the surface) causes a contraction of the lattice parameter of a nanoparticle as the diameter of the nanoparticle decreases [132–136]. The degree of contraction is material dependent and can also be affected by chemisorption, and for clean, freestanding Au nanoparticles with diameters of 1-3 nm that contraction is between 1-3% [134, 135].

Though the nanoparticles studied here are not freestanding and potentially have a different degree of contraction due to the interface, some contraction is expected and studies of Pt nanoparticles supported on carbon show good agreement with calculated values for freestanding particles [136]. The Au particles studied herein do not have significantly

reconstructed surfaces and should not be strongly influenced by chemisorption during synthesis (they are reduced in flowing N_2 , see Section 6.2); therefore, I hypothesize that their contraction is similar to the reported values. Assuming the Au lattice parameter undergoes a 1-3% contraction due to their sizes and comparing that lattice parameter to the pseudocubic lattice parameters of the $LnScO_3$ materials studied in Figure 6.3, the Au lattice is smaller than $LaScO_3$, comparable to $NdScO_3$, and larger than $GdScO_3$. These relationships likely play a significant role stabilizing the different populations of each Au morphology.

While γ_{bond} for the [111] type particles was demonstrated to be constant despite changes to the support, that is evidently not the case for the [110] type particles. Instead, the γ_{bond} term appears to have a notable dependence on strain mismatch between the metal and support demonstrated by the changes to the relative populations of [111] and [110] type particles. With the Au lattice contraction hypothesized to be 1-3%, the nanoparticles likely have the smallest strain mismatch on $NdScO_3$, and the increased strain mismatch on $GdScO_3$ and $LaScO_3$ makes the γ_{bond} term for the [110] type particles less negative, driving the overall energy of the particles up. Comparing $NdScO_3$ and $GdScO_3$, they host similar populations of [111] type particles with similar adhesion energies, but $GdScO_3$ has a much smaller fraction of [110] type particles. The increased energy of the [110] type particles owing to the strain mismatch reduces the number of [110] type particles on $GdScO_3$ with respect to the [111] type particles. $LaScO_3$ is similar to $GdScO_3$ regarding *relative* single crystal populations, as there are more [111] type particles compared to [110] type particles due to the increased strain mismatch compared

to NdScO₃; however, there are fewer total single crystals due to an increased selectivity towards MTPs which is discussed later.

Along with the strain mismatch, the bonding term for the [110] type particles is affected by the surface structure – the [110] type particles have a strong preference for flat, well defined (100)_{pc} support surfaces. This concept is illustrated in Figure 6.6, which contains images of Au nanoparticles supported on either ill-defined, rough surfaces or the minority exposed facets of the support, the (110)_{pc} surfaces. On these surfaces, no [110] type particles were observed; rather, they are localized to the (100)_{pc} surfaces. The exact structure of this interface is studied in detail in Chapter 8.

The increased population of MTPs on LaScO₃ compared to the other supports can be understood considering the lattice contraction in small metal nanoparticles and mismatch with the support, where the Au nanoparticles have a smaller lattice parameter than the pseudocubic LaScO₃ lattice. As discussed earlier in Section 6.3.2, the constituent crystallites in an MTP do not form a closed shape without either strain or structural modification [96, 99, 124, 126–130], and the increased tensile strain on LaScO₃ naturally accommodates this. The surface of an MTP requires expansion to close the gaps, and the tensile strain from LaScO₃ results in a greater population of MTPs on that support.

6.4. Conclusions

Au was deposited on the various LnScO₃ materials using a deposition precipitation reaction. Tensile strain at the LaScO₃ interface owing to the Au nanoparticle lattice contraction preferentially stabilizes MTPs, while the close lattice match on NdScO₃ promotes [110] type single crystals. Neither are particularly stabilized on GdScO₃, leading

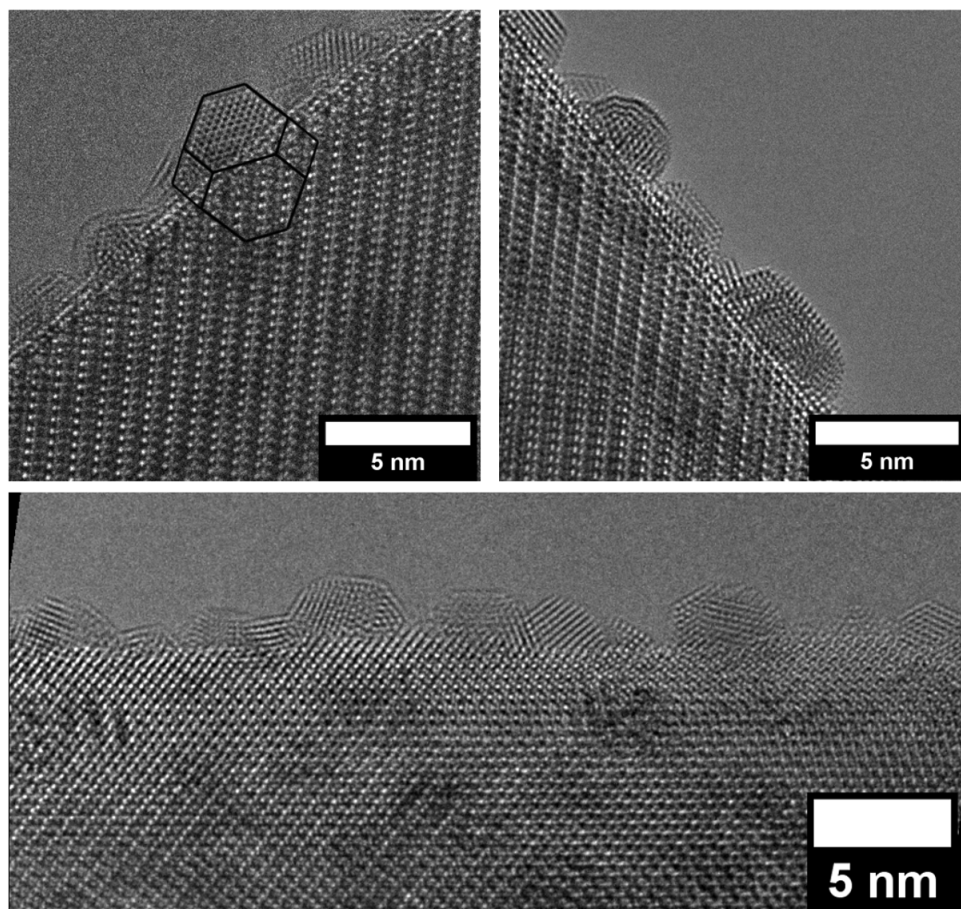


Figure 6.6. Au nanoparticles on NdScO_3 (110) pseudocubic surfaces (top) and a rough surface (bottom). No [110] type particles are observed, though some single crystals are seen. A Wulff shape is outlined in the top left figure to demonstrate that, through the particle has a pointed top similar to the particles in Figure 6.2b, it is not a [110] type particle.

to a moderate population of each. While these trends yield valuable insight to the ways that nanoparticles minimize energy, it is important to note that on all the supports, at least 50% of the particles are twinned, as MTPs are generally preferred at small sizes. The Au particles have a similar adhesion energy and degree of truncation on all supports, and this results in a similar interfacial geometry across all the LnScO_3 supports.

CHAPTER 7

CO Oxidation with Au/LnScO₃**7.1. Introduction**

Au is often referred to as the “most noble” of the noble metals [137] and is largely unreactive as a bulk material; however, in the late 20th century supported Au nanoparticles were found to be excellent heterogeneous catalysts, particularly for low temperature CO oxidation [16, 138]. Beyond reducing sintering at elevated temperatures, properties the substrate (e.g. reducibility [139–141]) can affect the catalytic performance of the system, and many studies of the support effect on CO oxidation by Au have been performed [17, 141–145]. These support effects can be very important [18–21], particularly when the active site sits at the interface between the metal and the support as Au catalyzed CO oxidation is often modeled [17, 138, 139]. In these cases, changes to the support will change the structural and chemical nature of the active site, which can result in significant changes to the catalytic performance of the materials.

Considering this, it is necessary to carefully consider the properties of the support material when designing a catalyst material. The selection of the best support material and metal nanoparticle for a given reaction will generate the ideal catalyst; however, predicting which support material properties are most significant towards this optimization is often a challenge. When considering different support materials to use for a catalyst there are many independently changing properties including, but not limited to, chemistry,

structural symmetry, surface properties, and electronic structure. These properties can both affect the behavior of the support material in reaction conditions (e.g. adsorption of reaction species [139]) and affect the interaction with the supported metal nanoparticle (e.g. particle adhesion [11]). In light of these complicating factors, it can be very difficult to identify the root cause(s) of any changes in catalytic performance when a given metal behaves differently on varied support materials.

Studies have been performed with the intention of disentangling these various support effects and isolating specific metal-support interactions. For example, Schlapka *et al.* performed a combination of physical experiments and theoretical simulations on Pt grown on Ru (0001) surfaces to separate the effect of strain from electronic interactions and study how strain impacts CO adsorption on the metal surface [146]. While successful, only a narrow window of Pt layers on the substrate were found to be accessible to study where the Pt was thick enough to screen the substrate yet thin enough to prevent strain relaxation. Studies of metal films backed by polymer substrates which are then mechanically strained attempt to remove electronic effects from the substrate entirely [147]; however, higher strains become inaccessible due to microstructural changes and delamination [148]. Another approach is to adjust either the surface termination and/or surface facet of the substrate, changing the interfacial structure while holding the bulk properties of the substrate material constant [6, 11, 118, 149–152].

In this chapter, the impact of changing support materials is studied using faceted LnScO_3 supports. As discussed in previous chapters, these materials have similar structures, surfaces, and adhesion energy of the supported Au nanoparticles, holding many of the aforementioned variable properties constant across the series. As a result, any

changes in catalytic performance between different Au/LnScO₃ materials can be isolated and their root causes identified. The probe reaction chosen is CO oxidation; supported Au nanoparticles are well-studied catalysts for this reaction and the lack of side reactions and multiple products allows for easier analysis of changes to performance and attribution of these changes to support properties. The changing lattice parameter is found to have no notable effect on the catalytic performance of the system, while the basicity of the support surface is identified as the significant property in determining the activation energy of Au/LnScO₃ catalyzed CO oxidation. NdScO₃ is the most basic support material, and the increase in basicity results from the chemically active 4f electrons of the lanthanide and the inductive effect these electrons have on the surrounding atoms.

7.2. Methods

The lanthanide scandate supports were synthesized by collaborators (R.J. Paull and E.P. Greenstein) using a hydro-sauna method for producing faceted nanoparticles [25, 26]. The surface areas of the bare supports were calculated using BET analysis with a Micromeritics 3Flex instrument. To characterize the relative CO₂ binding strength, TPD-MS was performed using an AMI-200 and a SRS Universal Gas Analyzer 100. TPD-MS samples were heated at 350 °C for 3 hours, pretreated with CO₂ at 50 °C for 20 min, then heated to 800 °C at a rate of 10 °C/min with simultaneous data collection. TPD-MS experiments were performed by E. Chang.

Deposition and characterization of the Au nanoparticles were discussed in detail in Chapter 4. To determine weight loading of Au on each sample, ICP-MS/OES was used as described in Chapter 2. Size distributions of the Au nanoparticles both before and after

catalytic testing were measured using ADF-STEM performed on a FEI Talos operated at 200 kV at Argonne National Laboratory or a JEOL ARM300F operated at 300 kV at Northwestern University.

Owing to the high atomic weight of the LnScO_3 supports and their large thicknesses, contrast from the small Au nanoparticles in HAADF was often insufficient for accurate size measurement and particle visualization. MAADF imaging was employed instead (multiple microscopes with different accelerating voltages were used and collection angles were experimentally optimized for each sample), in which the intensity at a given point in the image is primarily determined by diffraction contrast rather than mass-thickness effects. This comparison can be seen in Figure 7.1. Particle sizes were measured by drawing a line between the foci of the projected elliptical shapes of the Au, and a hemispherical shape for the Au was assumed when calculating the number of perimeter sites.

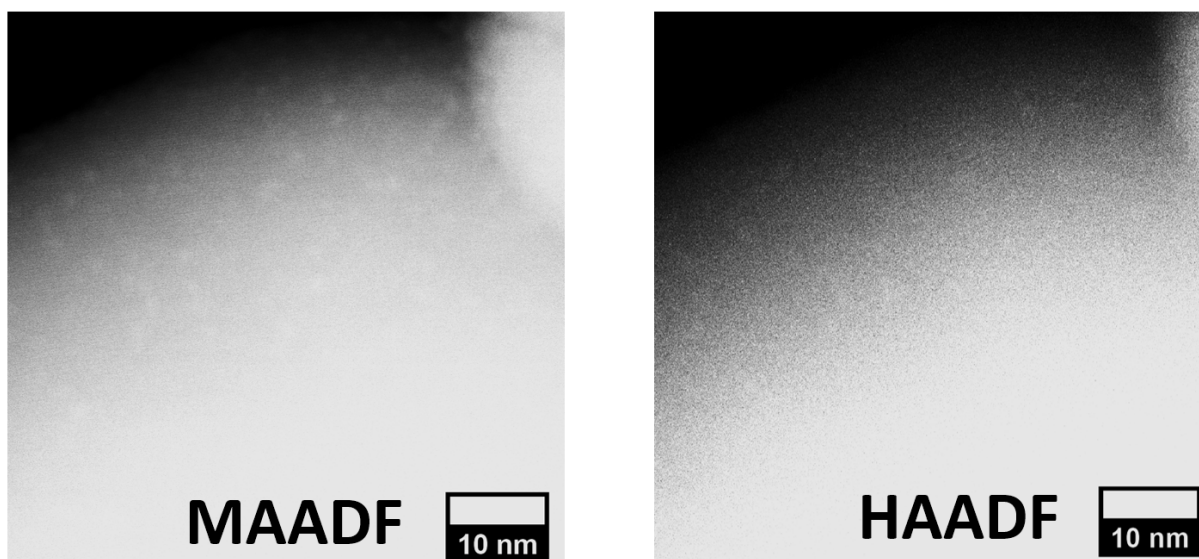


Figure 7.1. A comparison between HAADF and MAADF imaging of Au on GdScO_3 .

CO oxidation experiments were performed by collaborators L. Savereide and S. Tatro. For CO oxidation experiments using these catalysts, the samples were prepared by mixing 10-15 mg of catalyst with 400 mg of quartz sand (SiO_2) from Sigma Aldrich and dried for 90 minutes in a gas mixture of 40 sccm of oxygen and 10 sccm of helium. For analysis, the samples were first brought to 250 °C and held for 5 hours in 40 sccm of oxygen, 10 sccm helium, and 20 sccm of CO_2 to test the catalyst stability, and rate data was extracted after a steady state had been reached. The samples were then tested at 275 °C for 20 min under the same gas composition and flow rate. Finally, the samples were tested at 125, 150, 175, and 200 °C for 15 min each. Gasses bypassed the main reactor during all temperature changes, and the flow rates were controlled with a Camille data acquisition and control system. Products were measured using a Pfeiffer Thermostar Q200 Mass Spectrometer.

DFT calculations were performed for the bulk materials as described in Chapter 2.

7.3. Results

7.3.1. Bare Support Characterization

Images of the faceted nanoparticle supports and their surfaces can be found in Chapter 4 highlighting both the nanoparticle faceting and Sc rich surface terminations. To briefly recap, the LnScO_3 supports form faceted, cuboidal shapes that primarily expose the $(100)_{pc}$ surfaces. These surfaces are dominated by a double layer, Sc rich surface termination along with small areas containing a single layer, Sc rich termination. At the particle edges, the $(110)_{pc}$ surfaces form a bulk-like Sc rich surface termination with oxygen vacancies. The surface area was measured to be approximately 6 m^2/g for all of the

supports used in this work. This corresponds to a side length of approximately 150 nm for a perfectly cuboidal morphology, which is a good match to imaging.

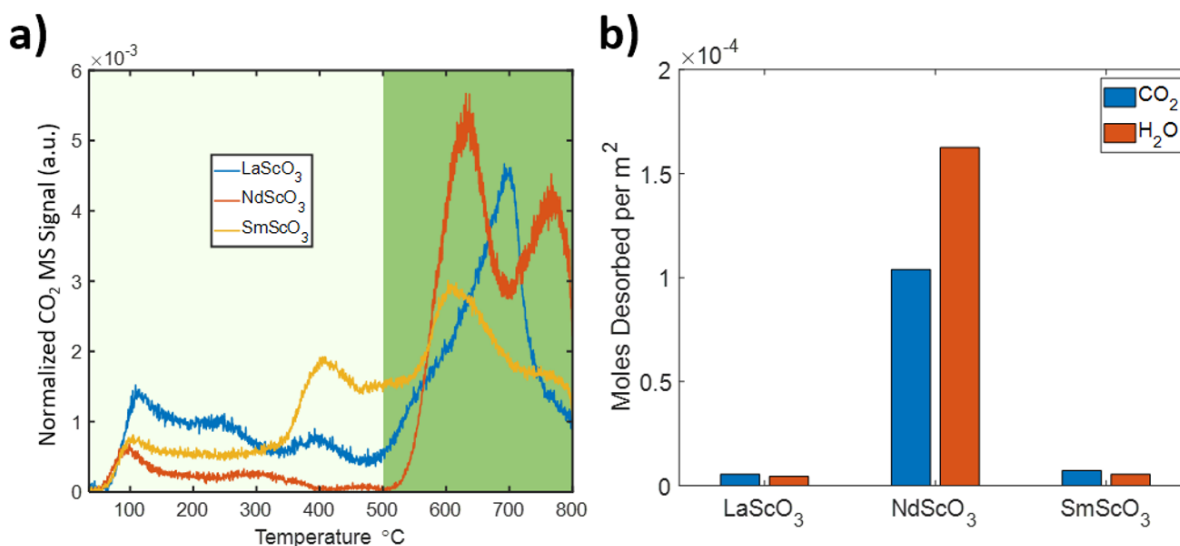


Figure 7.2. TPD-MS results from the bare supports are shown in (a). The signal is normalized to the total integrated CO₂ desorption and is divided at 500 °C between low and high temperature regimes. Moles desorbed per m² of each sample are reported in (b). NdScO₃ both bonds CO₂ more strongly than the other supports and has the most CO₂ per m².

Figure 7.2 contains results of the CO₂ TPD-MS experiments performed on the bare substrate materials. The plot is divided into two regimes for comparison, low temperature below 500 °C and high temperature between 500-800 °C, corresponding to weakly bound and strongly bound CO₂ respectively and as reported in Table 7.1. Comparing the CO₂ desorption from the supports within these regimes, the LaScO₃ and SmScO₃ materials desorb 30-40% of the total CO₂ desorbed during the experiment at low temperatures, while the NdScO₃ only desorbs 10%. The selection of 500 °C as the delineation between low and high temperatures is somewhat arbitrary, but any delineating temperature above 100 °C results in NdScO₃ desorbing a smaller fraction of CO₂ than the other supports at low

temperatures, indicating that the NdScO₃ surface more strongly adsorbs CO₂ and is the most basic.

Table 7.1. Comparison of CO₂ binding populations on LnScO₃

	LaScO ₃	NdScO ₃	SmScO ₃
Weakly Bound	34%	10%	39%
Strongly Bound	66%	90%	61%

In addition to binding a majority of the total CO₂ on the surface stronger than the other supports, NdScO₃ also binds a larger overall quantity of adsorbates, demonstrated in Figure 7.2b. Note the H₂O signal is the result of H₂O that was not removed from the surface during the 350 °C pretreatment step.

7.3.2. Au Sizes and Sintering

Moving to the Au/LnScO₃ catalysts, Au loadings were measured by ICP-MS/OES between 0.18 and 4.77 mole %. The loadings are reported in mole % rather than weight % due to the different molar weight of the supports, though it should be noted that the molar weights of the supports are rather similar. Compared to the weight %, mole % values are 18-24% higher depending on the support. The morphologies and adhesion energy of Au on the LnScO₃ materials was discussed in detail in Chapter 6, with the most relevant result pertaining to this chapter being the similar adhesion energy of Au on all LnScO₃ supports, which will be important later when seeking to assign trends in catalytic performance to catalyst properties.

The average sizes of the deposited Au nanoparticles both before and after catalytic testing are shown in Figure 7.3. Depending on the initial size of the Au, the particles

underwent one of two potential sintering routes: runaway or conventional sintering. The runaway sintering, or sintering of an unexpected magnitude, is the result of instability due to the increased chemical potential of the smaller Au nanoparticles (the chemical potential of a nanoparticle is inversely proportional to its radius). The smaller Au particles are more mobile on the support surface, and this leads to agglomeration, forming large dewetted polycrystals of Au. Particles with a larger initial size are more stable and undergo a conventional sintering with respect to the magnitude of size change and morphology, where the resulting particles remain similar both in relative height and shape.

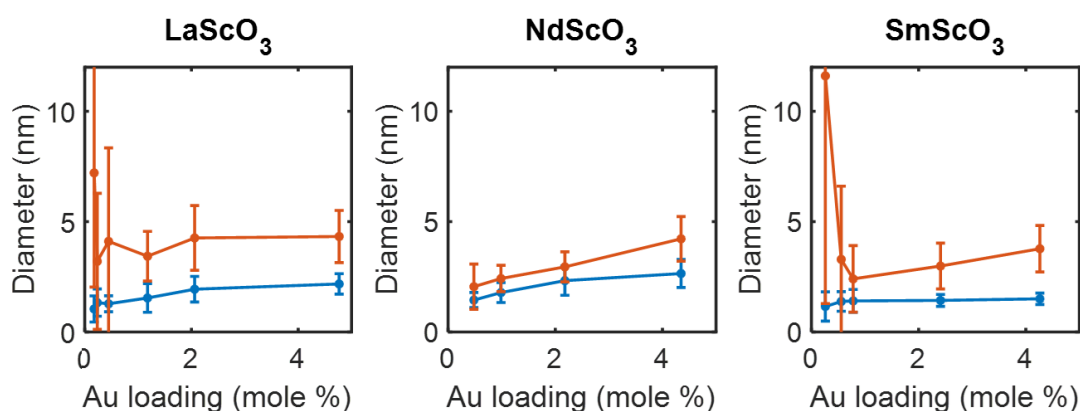


Figure 7.3. Average sizes of the as deposited (blue) and post-catalysis (orange) Au nanoparticles. As seen in the LaScO₃ and SmScO₃ data, very low loadings experienced runaway sintering.

Due to this runaway sintering, the lowest loadings of Au on LaScO₃ and SmScO₃ were not included in the analysis of the catalytic results as they are dissimilar to the other samples; furthermore, these loadings were not deposited on NdScO₃. The presence or absence of runaway sintering was identified by comparing the RMS of the final particle size distribution to the mean final particle size distribution. As the RMS is sensitive to the standard deviation and skew of a sample, a large difference between the two values

indicates the presence of this uncontrolled growth. Of the samples that were not excluded due runaway sintering, nearly all of the post-catalysis Au particle sizes on a given support were within one standard deviation of each other (the exception being the lowest and highest loadings on NdScO₃), indicating that particle size is not a changing variable between samples affecting changes in performance. Au surface density and further details of the particle size distributions can be found in Appendix C.

7.3.3. Catalysis

Figure 7.4a contains the apparent activation energies for CO oxidation calculated from TOF data in between 200 and 275 °C, the TOF data for each sample at 200 °C is in 7.4b, and Arrhenius plots used to calculate E_a are in 7.4c. Due to the fact that this reaction is typically modeled as an interfacial reaction (see Section 7.4.2), the TOF data in all cases is normalized to the number of perimeter Au atoms (i.e. the number of Au atoms at the boundary between the support, the Au nanoparticle, and the gaseous environment) per gram of catalyst. These values are calculated using the sizes measured after catalytic testing because a majority of Au sintering should occur during the initial 5 hour hold at 250 °C. TOF values calculated from initial particle sizes can be found in Appendix D along with TOF data from other temperatures.

At each loading, the highest energy barrier occurs for Au/NdScO₃, followed by Au/SmScO₃ with the lowest barrier on Au/LaScO₃. This matches the trend observed in Figure 7.2a within the same temperature window: NdScO₃ retains the most CO₂, then SmScO₃ followed by LaScO₃. There is less distinction between the supports in the TOF data, but NdScO₃ is typically the slowest at low loadings.

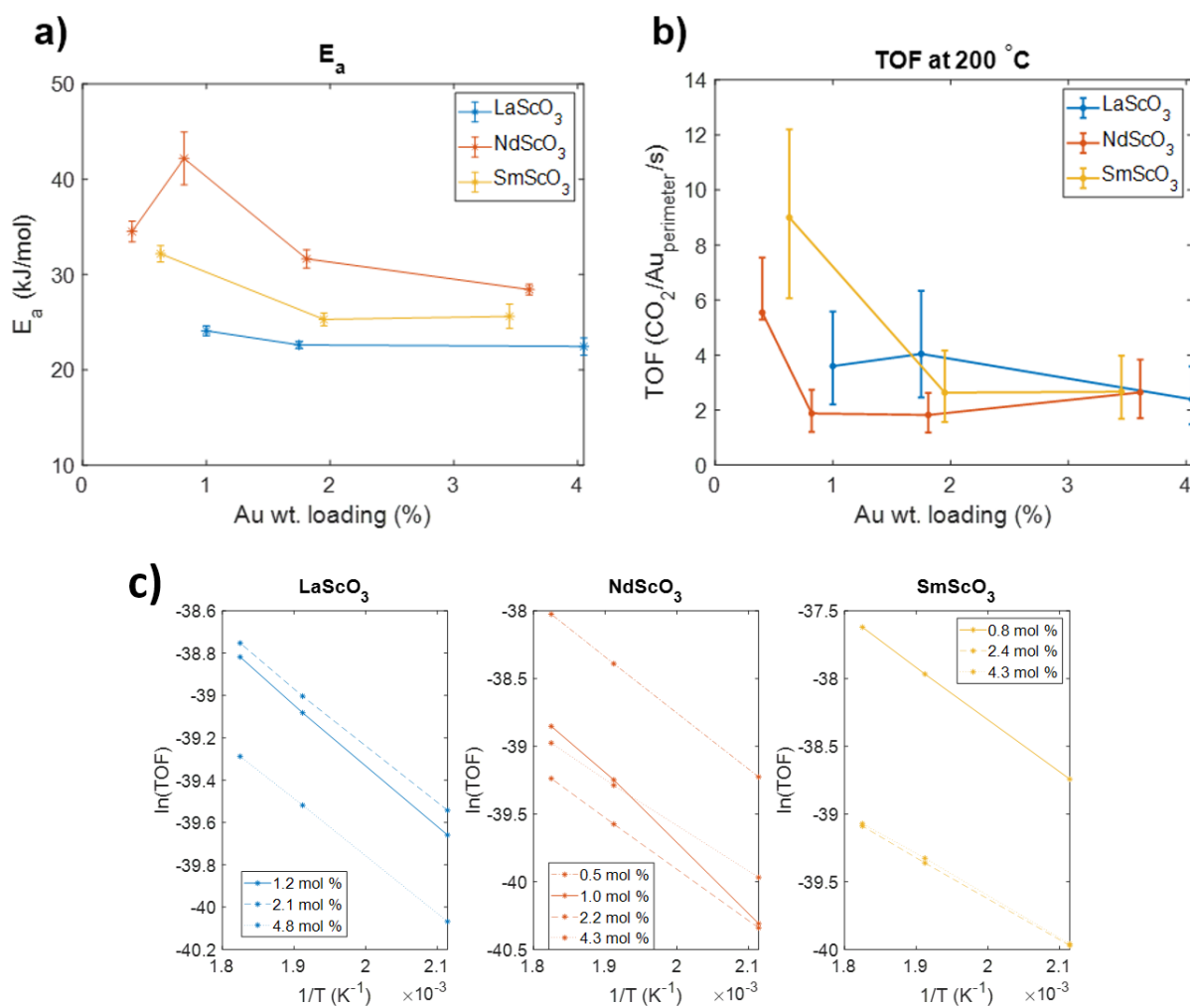


Figure 7.4. Apparent activation energies for CO oxidation with the different support materials at each weight loading is given in (a) with error bars calculated from a linear least squares fit of the Arrhenius plots in (c). TOF data for each sample at 200 °C, along with error bars calculated from the particle size standard deviations are shown in (b).

7.4. Discussion

Owing to the similarities between the support materials and the similar adhesion energy of the Au on each support, many of the potential causes of changes to catalytic

performance between different samples are held constant. Considering the support surfaces, all the LnScO_3 nanoparticle supports have similar Sc rich terminations, indicating that changes to performance are not linked to structural or chemical changes at the surface as they might be when comparing supports such as alumina, zirconia, and titania. Additionally, the lattice parameter changes linearly as the size of the lanthanide changes in the lanthanide series, and a similar trend is not observed in the catalytic data eliminating the lattice parameter and epitaxial effects as the property of significance (this is notably not the case in many other systems where strain plays a significant role [153–156]). This is further evidenced by the similar adhesion energy of Au on the support surfaces despite lattice parameter changes.

7.4.1. Surface Basicity and the 4f Inductive Effect

Strong correlation is observed between catalytic performance and the CO_2 binding strength on the support and, by extension, the support surface basicity. NdScO_3 both binds CO_2 more strongly than the other supports and chemisorbs a significantly larger amount of adsorbates per unit area of the surface as shown in Figure 7.2. The source of this stronger adsorbate interaction is the increased chemical activity of the Nd 4f electrons compared to the other supports. Previous studies of TbScO_3 and DyScO_3 identified 4f electrons at the valence band edge (close to the Fermi energy) using both DFT and XPS, indicating chemical activity [49]. Published XPS results of NdScO_3 contain a similar peak near the Fermi energy [157, 158], and examining the pDOS from DFT calculations of NdScO_3 show the 3 4f electrons near the valence band edge in Figure 7.5. LaScO_3 , which contains

no 4f electrons, and SmScO_3 , which contains 5 4f electrons at deeper energies, do not have comparable chemical activity resulting from the 4f orbitals.

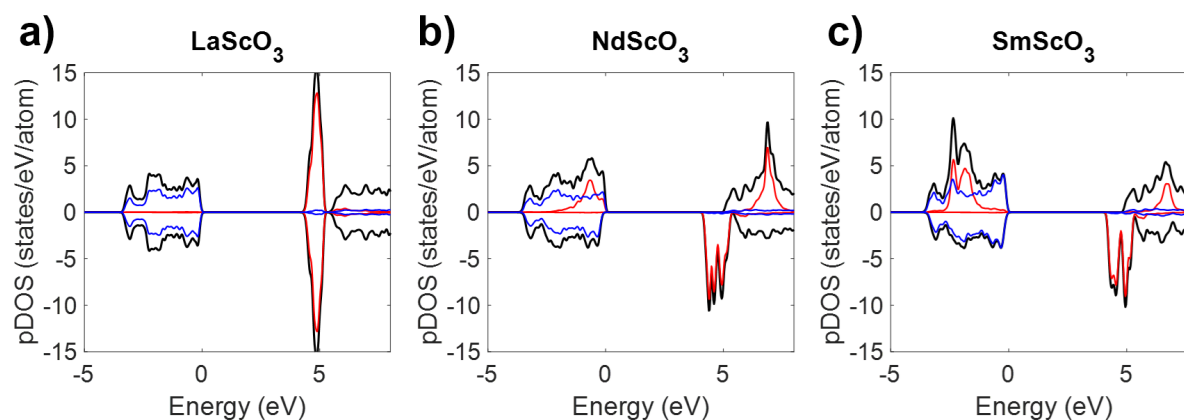


Figure 7.5. Density of states of the LnScO_3 materials used in the catalytic experiments. Black lines represent the total DOS, red the Ln 4f, and blue the O 2p. As seen, the O₂p states sit at the valence band edge for all the materials. The 4f electrons of NdScO_3 are also at the valence band edge, indicating chemical activity, while in LaScO_3 (a), there are no 4f electrons and in SmScO_3 (c) they sit at deeper energies.

The chemical activity of the 4f electrons in NdScO_3 indicates that the Nd sites are less Lewis acidic than the lanthanide sites in the other supports, increasing the basicity of the overall system. This affects the chemisorption of adsorbates requiring electron donation from the support during the reaction process, making chemisorption easier and the resulting binding stronger for those species. It is important to note that this is not a direct process, as the surfaces contain a double layer scandium rich termination. Instead, this is an inductive effect, where the active 4f electrons affect nearby oxygen atoms, which can then more readily donate charge. This is a similar trend to d-band theory as proposed by Hammer and Nørskov [137], wherein a higher d-band center causes a

stronger interaction with adsorbates. However, the mechanisms of d-band theory, which focuses on the filling of antibonding states, and the 4f inductive effect are different.

7.4.2. Reaction Pathway and the Impact of the 4f Electrons

The reducibility of the support material plays a significant role in determining the low energy reaction pathway for CO oxidation, particularly the ability of the support to adsorb O₂ or create O vacancies via reduction. Comparing MgO, an irreducible support, and TiO₂, a reducible support, theoretical studies predict an Eley-Rideal (E-R) mechanism on MgO [159, 160] and a Langmuir-Hinshelwood mechanism on TiO₂ [161] as the low energy pathway. Additionally, reducible supports such as TiO₂ [162] and CeO₂ [163] can form O vacancies as the source of O in the reaction at higher temperatures, promoting a Mars van Krevelen mechanism.

The lanthanide scandate materials studied herein are irreducible, and therefore an E-R mechanism is proposed similar to that on MgO [159, 160] and pictured schematically in Figure 7.6. Here, CO binds directly to the Au (A) then reacts with gaseous O₂ to form the intermediate species of oxidoperoxidocarbonate [164–170], O¹CO²O³ (B, the O atoms are numbered for discussion purposes only here and in Figure 7.6) via electron donation from the support. The intermediate can then either decompose then desorb CO₂ (C), or move directly to D. The O³ remaining at the interface is very active and readily reacts with atmospheric CO.

Forming the O¹CO²O³ intermediate from bound CO and environmental O₂ requires charge transfer to the O³ atom, a process facilitated by the increased basicity of NdScO₃ owing to the 4f inductive effect. Here, the inductive effect both lowers the free energy

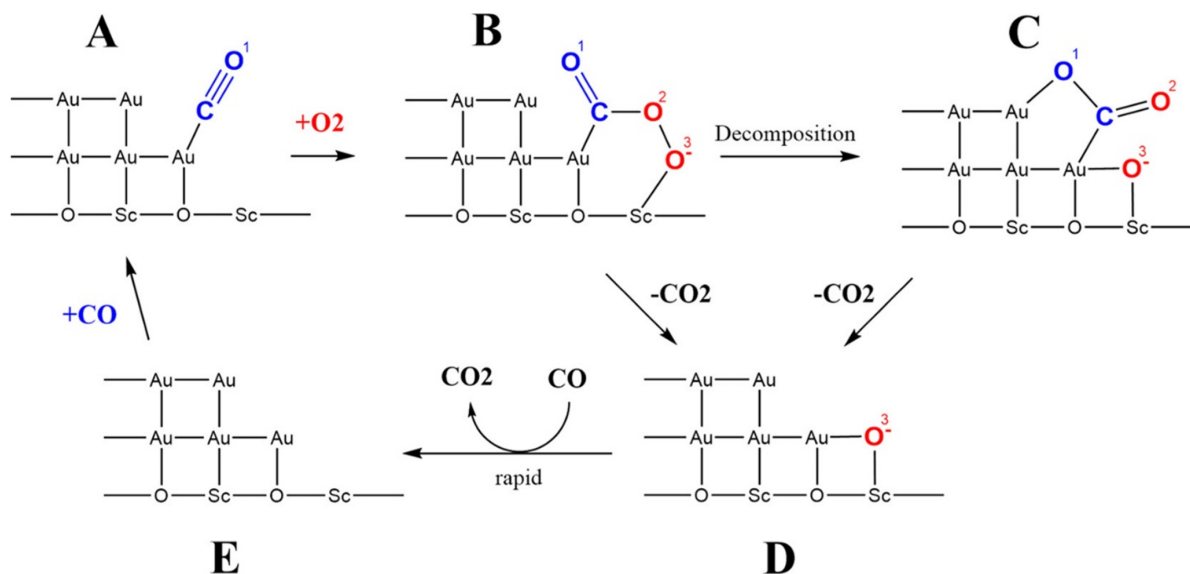


Figure 7.6. Proposed E-R reaction mechanism for CO oxidation over the Au/LnScO₃ catalyst materials. CO adsorbs to the Au nanoparticle in (A) then forms the intermediate O¹CO²O³ species in (B) following the adsorption of O₂. From here the intermediate can either decompose to (C) before CO₂ desorption or move directly to (D). In either case, the lowered energy of (B) on NdScO₃ due to the 4f inductive effect increases the energy barrier. The remaining O₃ at the interface readily reacts with gaseous CO to form CO₂ and refresh the catalyst active site in (E).

of the transition state in the formation of the intermediate O¹CO²O³ species, as well as lowers the free energy of the intermediate. The C atom is bonded to the metal, so the decomposed species in Figure 7.6C relatively agnostic to the 4f inductive effect owing to its distance from the support. By lowering the energy of the intermediate with respect to the later steps of the reaction mechanism, the 4f inductive effect increases the overall energy barrier of CO oxidation over NdScO₃. This is similarly true for the potential pathway moving directly from B to D, as the energy of the desorbed CO₂ does not depend on the support and the relative barrier is higher.

While the 4f inductive effect hinders the reaction in this case and generates a larger energy barrier, this is not universally true for all material systems. Preliminary work from E. P. Greenstein studying CO oxidation with Pt/LnScO₃ found the smallest energy barrier when using Pt/NdScO₃ as the catalyst compared to the other supports, shown in Figure 7.7. Previous studies of this system indicate that factors such as competitive adsorption of the reactant molecules (CO and O₂) [171] cause the formation of the intermediate to be the rate limiting step, and in this case the reduction of the free energy of the intermediate is leveraged to promote the reaction. It is important to emphasize that these results are preliminary and require further study.

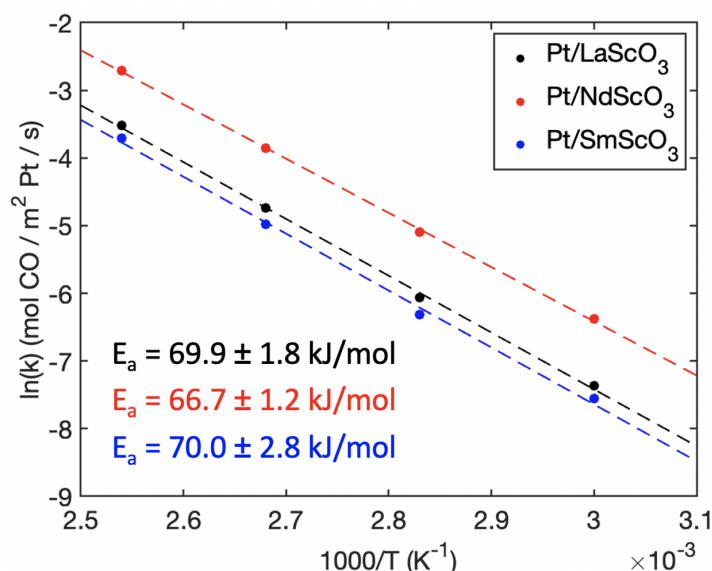


Figure 7.7. Preliminary results of CO oxidation over Pt/LnScO₃. In contrast to Au/LnScO₃, the energy barrier is smallest when the support material is NdScO₃.

7.5. Conclusions

Through detailed experimental and theoretical studies of the Au/LnScO₃ materials and comparison to their performance as catalysts for CO oxidation, strong correlation is observed between the support basicity and apparent activation energy of the reaction. The formation and bonding of the intermediate species to the Au/LnScO₃ interface is affected by changes to the support basicity, which is in turn affected by the 4f inductive effect. Here, small changes to the Lewis acidity of the support due to this inductive effect significantly affect charge transfer to the reaction species, lowering the free energy of the intermediates and changing the energy barriers of the reaction.

This work has been published in [172]

CHAPTER 8

The Pt(110) on LnScO₃ (110) Interface**8.1. Introduction**

Chapter 7 concluded discussing preliminary results of CO oxidation with the Pt/LnScO₃ catalyst system; however, a comprehensive understanding of the behavior of this catalyst requires analysis of the nanoparticle morphologies and energetics. To achieve this, the Pt requires a similar analysis to that performed on the Au nanoparticles in Chapter 6 (see Chapter 9 for proposed future work). Preliminary imaging of Pt supported on LaScO₃ found [110]-type particles on the (100)_{pc} support surfaces, like those found in the Au/LnScO₃ catalysts, as shown in Figure 8.1. This indicates that the stabilization of the [110]-type particles is not unique to Au; rather, it applies other FCC metals supported on LnScO₃ (100)_{pc} surfaces. Furthermore, previous imaging of Pt supported on SrTiO₃, a perovskite with a similar lattice parameter, did not observe the [110] type particles [11, 119]. These observations beg the question: what is unique about the LnScO₃ (100)_{pc} surface that preferentially stabilizes the [110]-type metal FCC nanoparticles?

In this chapter, the interface formed between the (110) plane of Pt and the (110) surface of GdScO₃ is modeled and relaxed with DFT. The arrangement of the O atoms on the reconstructed (110) double layer surface is found to align very well with the corrugated shape of the (110) plane of Pt with minimal strain to the Pt, and analysis of the power spectra of HREM images from the Au/LnScO₃ reveals a coincident site lattice (CSL).

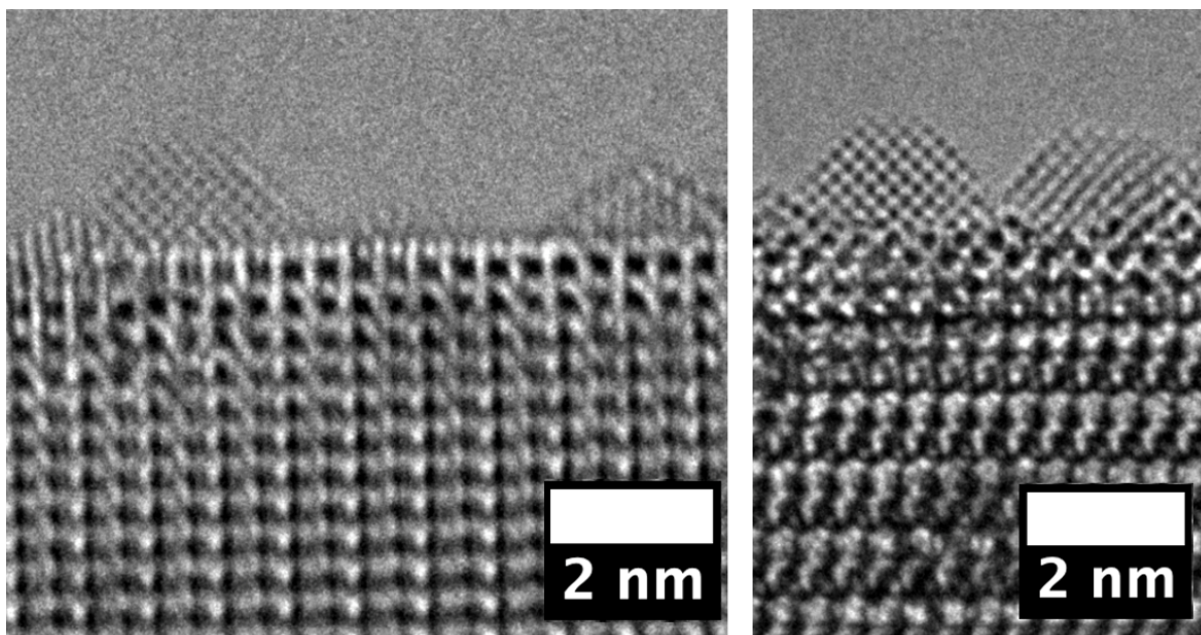


Figure 8.1. Images of [110] type Pt particles on LaScO_3 $(100)_{pc}$ surfaces.

This structural compatibility between the double layer surface reconstruction and the Pt (110) surface is responsible for lowering the γ_{bond} term discussed in Chapter 4, reducing the energy of the [110] type particles on the reconstructed LnScO_3 double layer surfaces. The electronic properties of the interface are then explored, revealing induced charge in the interfacial Pt atoms as well as the presence of metal induced gap states (MIGS).

8.2. Methods

The LnScO_3 support materials were prepared using the same hydro-sauna process as those in previous chapters [25, 26]. In contrast to the deposition precipitation reaction used to deposit Au, the Pt nanoparticles were deposited on the surface using atomic layer

deposition (ALD) carried out by a collaborator, R. Hackler, using trimethyl(methylcyclopentadienyl)platinum(IV) (MeCpPtMe_3) and ozone as the platinum source and counter-reagent respectively for one cycle. The nanoparticles were then imaged using either the ACAT operated at 200 kV at Argonne National Laboratory. DFT calculations were performed using the parameters described in Chapter 2 for the Gd, Sc, and O atoms. The Pt atoms had a muffin tin radius of 2.1, and the Pt 4f electrons were treated as core states. The interface was modeled using a GdScO_3 slab with 180 atoms with 6 overlayers of Pt on each surface, for a total of 252 atoms. $P\bar{1}$ symmetry was used.

8.3. Interfacial Structure

Profile view models of the GdScO_3 (110) and (001) double layer surface structures viewed along a $[100]_{pc}$ direction and a view of Pt along the $[1\bar{1}0]$ direction are shown in Figure 8.2 using space-filling atomic spheres. As seen, the O atoms on the GdScO_3 surfaces form raised rows along the view direction, and this is very similar to the corrugated structure of the (110) surface of Pt. For the Pt/ GdScO_3 system, the corrugation of the Pt (110) surface and the raised O atoms of the (110) surface will align perfectly (i.e. the lower Pt atoms of the corrugation will sit in the channels between the O atoms) when a 2% tensile strain is applied to the Pt in the $[001]$ direction. Applying a 4% compressive strain in the $[1\bar{1}0]$ direction provides a lattice match in the other GdScO_3 $[100]_{pc}$ direction and creates a CSL.

A strictly epitaxial interface implies a perfect alignment of the two similarly oriented constituent lattices with or without the application of strain; this interface instead forms a CSL, where only certain sites align. The coincident nature of the interface is observable

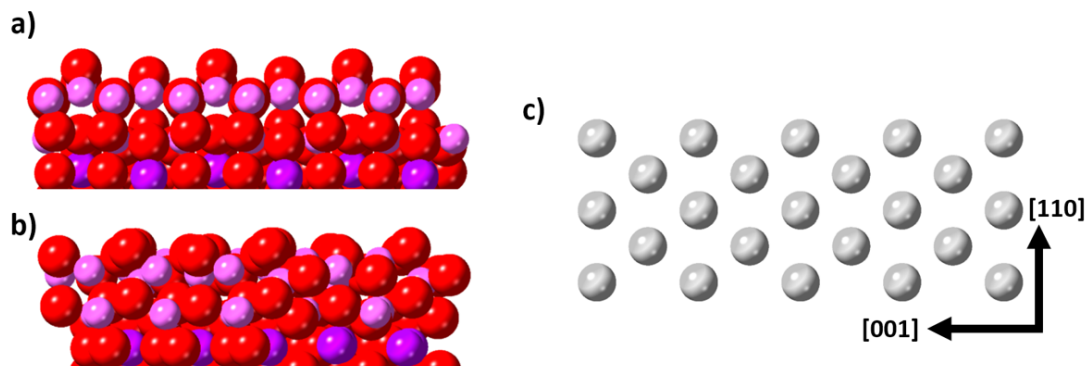


Figure 8.2. Profile views of the (110) and (001) GdScO_3 surfaces in (a) and (b) respectively, with a profile view of the (110) surface of Pt shown in (c) viewed along the $[1\bar{1}0]$ direction.

in Figure 8.3, which is the power spectrum of Figure 6.2b in Chapter 6 (a HREM image containing Au and NdScO_3 viewed along $[110]$ directions, data from Au is used here as no images of Pt are of both high enough quality and properly oriented to clearly observe the power spectra from the nanoparticle). Coincident reciprocal lattice points are highlighted in the figure.

A model interfacial structure was created and is shown in Figure 8.4a and 8.4b, and atomic positions were allowed to relax in DFT yielding the structure in Figure 8.4c and 8.4d. The topographical matching of the O atoms in the surface and the Pt (110) creates a favorable interfacial structure, lowering the γ_{bond} term and promoting the formation of $[110]$ type particles on this surface. Importantly, this is the direct result of the structure of the LnScO_3 $(100)_{pc}$ double layer reconstruction, and this structural matching is not present on the $(100)_{pc}$ single layer reconstruction, or the $(110)_{pc}$ surfaces. As discussed in Chapter 6, $[110]$ type particles were not observed on the $(110)_{pc}$ surfaces nor on rough surfaces. It is important to note that if the reconstruction was unknown, the presence of the $[110]$ -type particles would be inexplicable. Additionally, this pattern of raised O

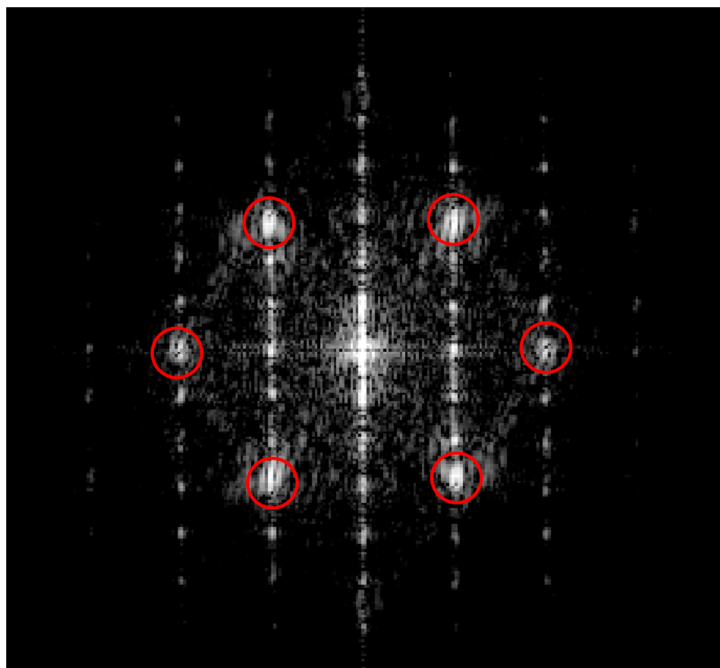


Figure 8.3. Power spectrum of Figure 6.2b, which includes Au and GdScO₃ along [110] zone axes. Overlapping reciprocal lattice points are outlined in red, demonstrating the coincident nature of the two orientations.

atoms is not present on SrTiO₃ nanoparticle surface reconstructions [59], where this type of interface is not typically observed as previously mentioned.

8.4. Induced Charges

The Pt atoms at the interface are arranged as depicted in Figure 8.5. To explore the electronic interaction between the Pt and substrate atoms, the Bader charge [173] of each interfacial Pt atom was calculated, and these results are overlaid on each atom in Figure 8.5. Briefly, the Bader charge reported here is a measure of the total number of electrons associated with a given atom in a structure subtracted from the number of electrons the atom should have given its atomic number (e.g. 78 for Pt). In a typical metal this value

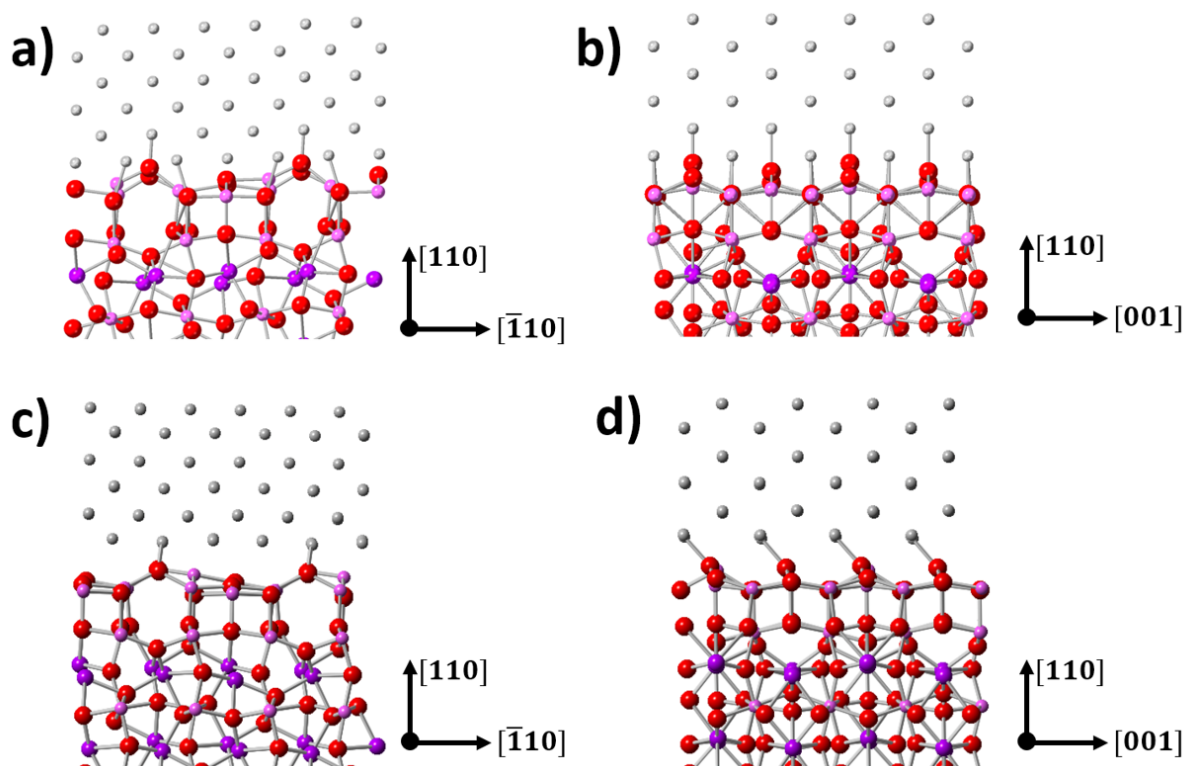


Figure 8.4. The initial structural model for the (110) interface is shown in (a) and (b), along with the final, DFT relaxed structure in (c) and (d). The Pt and GdScO_3 directions are given by the axes to the right of each model.

would be zero for all atoms, while for a purely ionic solid such as NaCl these values would be close to +1 and -1 for Na and Cl respectively. Further details of the Bader charge are found in the references.

The results of this analysis are consistent with those expected when considering image charge [174–176], or the charge that is induced near an oxide surface. Local dipole moments will form at the surface due to the non-zero charge of the surface atoms, here -2 and +3 for the O and Sc respectively, and these induce a small amount of charge in the Pt. As seen in Figure 8.5, the Pt atoms that are directly above the empty Sc sites (recall from Chapter 3 and Chapter 4 that 6 of 8 potential Sc sites are occupied in

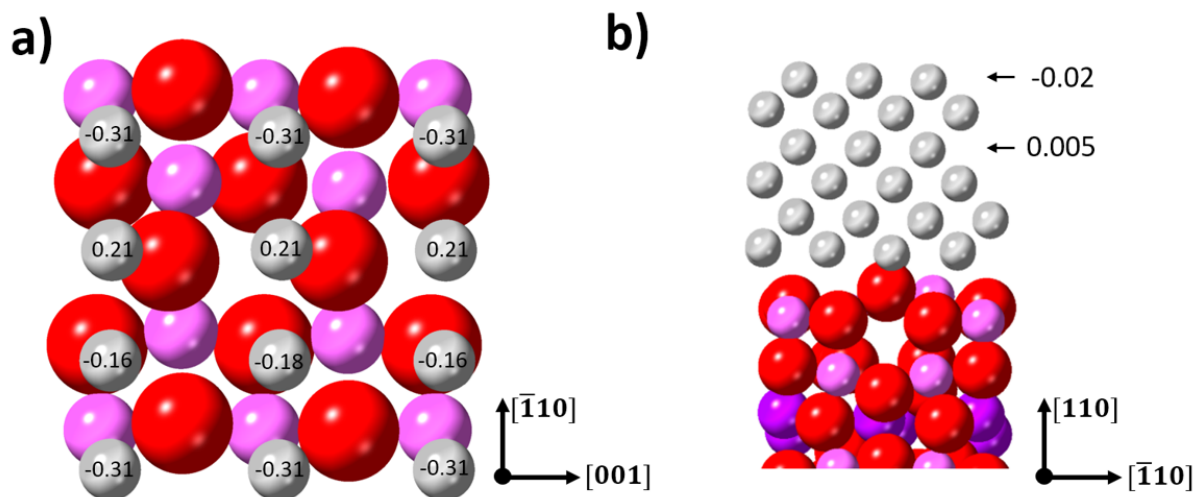


Figure 8.5. Arrangement of the first layer of Pt atoms at the interface is shown in (a), along with the Bader charges overlaid on each atom. The average Bader charges at the topmost and an inner layer of the Pt are given in (b) and are close to zero as expected.

the reconstruction) have a slight positive charge associated with them, while those near the Sc atoms have a slight negative charge. This small amount of induced charge has been predicted in other systems [177–181], though the listed references are not perfect comparisons to the Pt/LnScO₃ system. Moving away from the interface, the Pt Bader charge predictably approaches zero as shown in Figure 8.5b.

In future work on this interface, this calculation could be repeated for other LnScO₃ materials to explore any variations on this induced charge with the different Ln cations, particularly NdScO₃ considering the inductive effect.

8.5. Electronic Structure of the Interface

Figure 8.6 contains the pDOS of the O 2p and Sc 3d states in the interfacial GdScO₃ layer compared to the bulkmost layer. At the interface, the GdScO₃ is no longer purely an

insulator as the pDOS is nonzero between the valence band and conduction band edges, as defined by the O 2p and Sc 3d states of bulkmost layers respectively. These MIGS are a common feature of metal-oxide interfaces [182–186] and result from Fermi level pinning due to the presence of the metal. These states are isolated at the interface - the total density of states of the 3 GdScO₃ atomic layers closest to the interface can be found in Appendix E, along with the 3 interfacial layers of Pt for completeness.

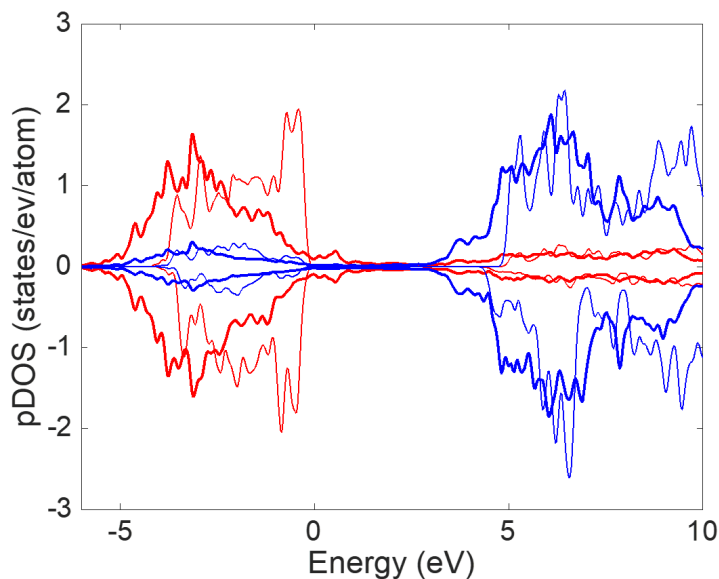


Figure 8.6. Comparison of the interfacial (bold lines) and bulk (thin lines) O 2p (red) and Sc 3d (blue) pDOS of GdScO₃. Positive values are spin up and negative are spin down.

Additionally, Figure 8.7 compares the electronic structures of the negative (blue) and positive (red) Pt atoms at the interface discussed in the previous section with the electronic structure of bulk Pt (black). As shown, the difference between the two interfacial Pt atom types is rather small compared to the difference between bulk and interfacial Pt. It is possible that the sites will behave slightly differently in catalytic reactions that

would require electron donation or acceptance by the catalyst, though more calculations including adsorbates would be necessary to begin drawing significant conclusions.

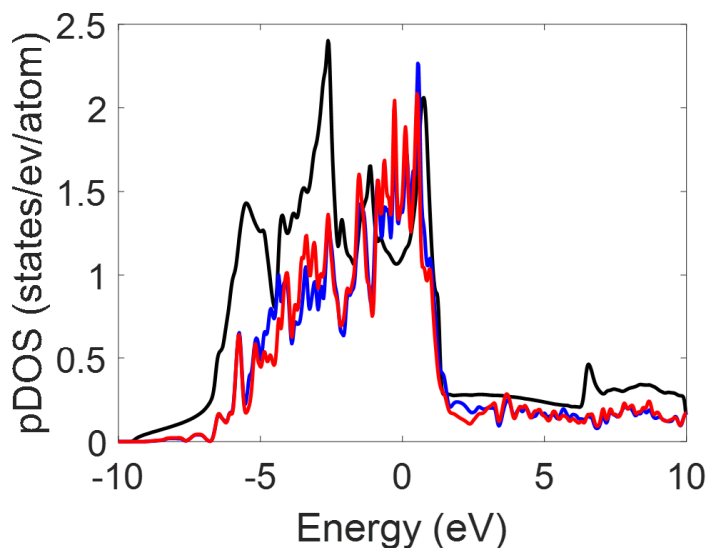


Figure 8.7. pDOS of the positive (red) and negative (blue) Pt atoms at the GdScO_3 interface compared to the pDOS of Pt from a separate, bulk calculation.

8.6. Conclusions

The [110]-type particles discussed in Chapter 6 are also observed with Pt, indicating that the interface formed between these particles and the support has a strong γ_{bond} comparable to the energy difference between γ_{111} and γ_{110} . To understand the origin of this strong bonding, the structure of the interface between Pt (110) and GdScO_3 (110) is modeled, and its electronic structure and properties are assessed using DFT. The CSL nature of the interface, along with the topographical compatibility of the O atoms of the reconstruction with the Pt (110) surface, reduce the interfacial energy and promote the formation of the [110]-type particles. The calculated electronic properties of the interface

are unsurprising considering previous literature regarding image charge and MIGS, and future work comparing these properties on the different LnScO_3 would be informative towards understanding any variations in the LnScO_3 materials in future applications.

CHAPTER 9

Summary and Future Work**9.1. Summary**

In this thesis, a series of lanthanide scandate materials were characterized in detail using both experimental and computational methods, then used as supports for noble metal nanoparticles to catalyze CO oxidation. The LnScO_3 materials were found to have a similar, Sc rich double layer termination on a majority of the exposed facets, and the supported Au nanoparticles had a similar degree of adhesion on all of the support materials. The 4f electrons near the valence band edge in NdScO_3 generate an inductive effect that facilitates stronger binding of adsorbates compared to the other LnScO_3 materials. This effect stabilizes the intermediate species in the reaction, and CO oxidation over Au/NdScO_3 had the highest apparent activation energy as a result. Looking forward as we transition to studying Pt on the LnScO_3 supports, I propose the following 4 projects for future work.

9.2. Theoretical and Experimental Analysis of Pt/ LnScO_3 - Electronic Structure

In Chapter 8, the interface between the (110) surface of Pt and the (110) surface of GdScO_3 was analyzed using density functional theory informed by HREM. This epitaxial relationship was observed via electron microscopy, and further experimental study using DPC and EELS would be an appropriate compliment to the DFT analysis presented in the

previous chapter. Additionally, the interface between Pt(111) and the support surface can be studied both theoretically and experimentally, then compared to the Pt(110) interface.

DPC is a STEM technique in which the position of the central diffraction disc is tracked to determine the local electronic structure of a material. Electric fields will deflect the beam, and by measuring these deflections one can identify the direction and magnitude of electric polarization. A schematic of this technique and an example application measuring polarization is given in Figure 9.1.

Performing a series of DPC experiments on samples of Pt supported on the different LnScO₃ materials would give useful insight towards the electronic structure of the interface. Catalytic reactions are driven by electron transfer between the catalyst and reactants, and the major conclusion of Chapter 7 was that the 4f inductive effect from Nd facilitates easier electron transfer to the intermediate species. Through DPC the direction and relative magnitude of any electron transfer between the different support materials and Pt nanoparticles can be experimentally compared, and the impact of the 4f inductive effect can be observed.

Along with DPC, EELS measurements of the interface would serve to experimentally confirm the metal induced gap states (MIGS) that were identified by glsdft in Chapter 8. Comparable experiments have been performed on a Cu/MgO interface, observing these states in both DFT and EELS [182]. By observing any pre-edge features in the oxygen K-edge in EELS, these states can be verified and compared across the different lanthanide scandate materials.

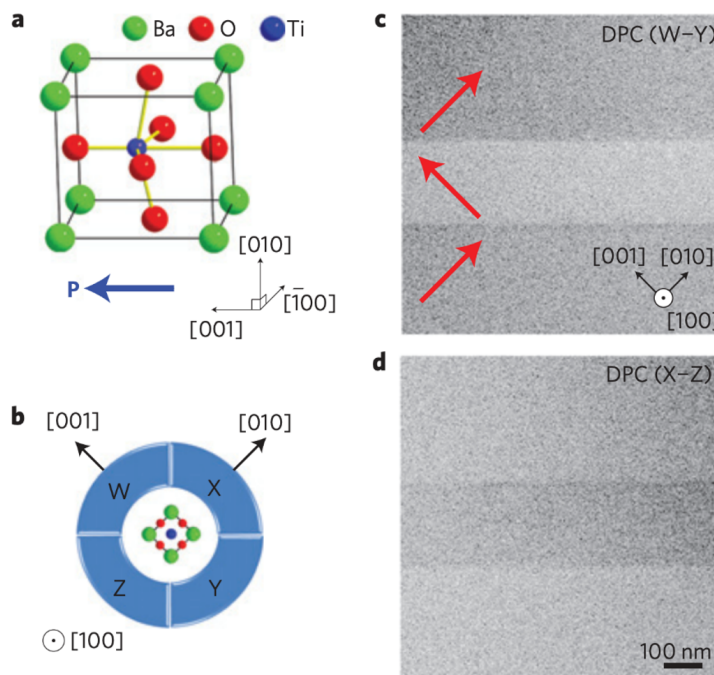


Figure 9.1. Schematic of the DPC method and application to measure polarization of BaTiO_3 (a). Considering the detector geometry in (b), the direction and magnitude of the beam deflection can be measured via the difference in signal between opposing detector segments, as in (c) and (d). Explicitly, where (W-Y) is bright in Figure (d), the beam has deflected towards segment W. Figure reproduced by permission from Springer Nature, Nature Physics [8], Copyright 2012.

9.3. Experimental Analysis of Pt/ LnScO_3 - Adhesion and Orientation

Chapter 5 contains an experimental assessment of the adhesion energies and morphological distribution of Au/LnScO_3 . While the strain mismatch affected the relative population of twinned particles compared to single crystals, the adhesion energies remained relatively constant. A comparable analysis of Pt is certainly warranted for a full understanding of the interfacial energetics and strain in the Pt particles.

While no significant changes in particle adhesion were observed in Au, this may not be the case for Pt: Enterkin *et al.* demonstrated the impact of strain mismatch on Pt nanoparticle adhesion on SrTiO₃ vs. (Ba,Sr)TiO₃ in Figure 9.2a [11]. Additionally, initial DRIFTS measurements of Pt/LnScO₃ in Figure 9.2b show a relationship between the CO binding configuration and the support material used. Considering this previous work, I believe a comparative study of Pt on the different LnScO₃ materials to observe the particle adhesion and morphology, as well as carefully measuring lattice parameters to observe any potential strain in the Pt, will provide necessary insight to the behavior of these particles in catalysis.

I hypothesize that the Pt/LnScO₃ system will also be ideal for studying the effect of strain mismatch on Pt orientation. Previous work on Pt/SrTiO₃ found a significantly higher population of single crystalline particles than twinned particles [11, 119], and the preliminary imaging performed on Pt/LnScO₃ agrees with this finding. The (110) interface discussed in Chapter 8 is the result of strong bonding between the nanoparticle and support while the (111) interface is the result of the lower energy of the (111) plane of Pt. The strain mismatch between LnScO₃ and Pt varies depending on the LnScO₃ material, and this should preferentially affect the bonding of the (110) interface while having a lesser effect on the (111). Instead of forming MTPs to accommodate different amounts of tensile strain, I suspect the Pt particle orientation and adhesion energies will be affected. This can be experimentally confirmed by comparing the relative populations and adhesion energies of each orientation on the different support materials, then compared to the results of catalytic experiments.

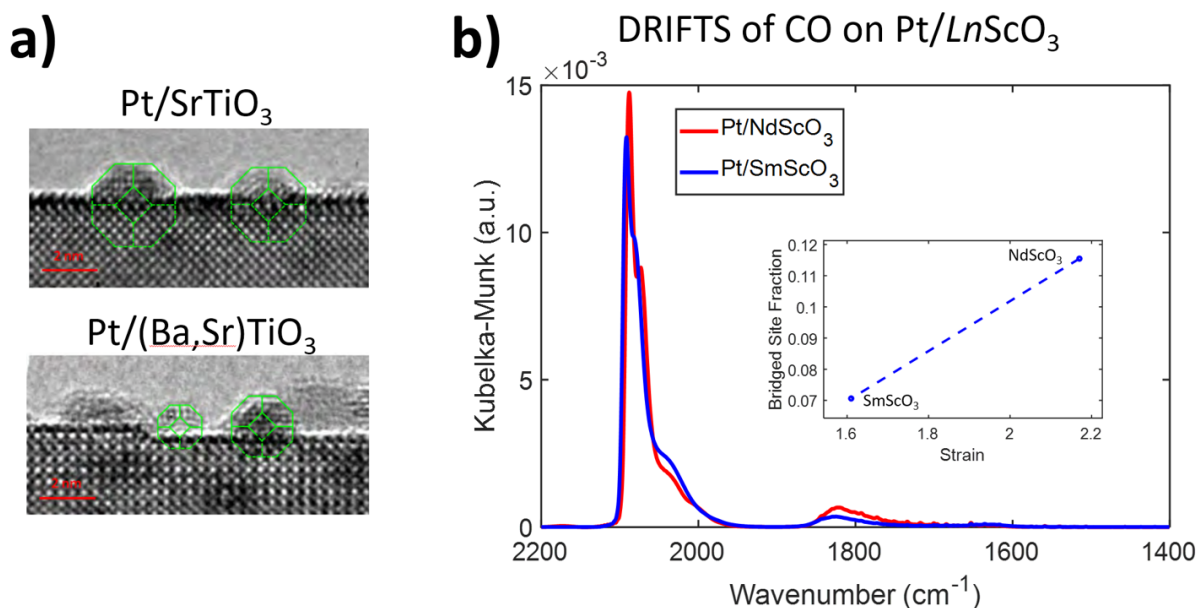


Figure 9.2. HREM Pt supported on SrTiO₃ and (Ba,Sr)TiO₃ is shown in (a). The strain mismatch is greater on (Ba,Sr)TiO₃, and the Pt particles have a greater adhesion energy demonstrated by the decreased adhesion. DRIFTS of CO on Pt/LnScO₃ is reported in (b). The signal above 2000 cm⁻¹ is associated with linearly bound CO, and the signal near 1800 cm⁻¹ with bridged CO [9, 10]. The relative population of bridged compared to linearly bound CO (calculated via integrating the peak areas) as a function of strain mismatch is inset, though adding more datapoints is necessary to begin drawing conclusions related to trends in this behavior. (a) is reproduced by permission from Springer Nature, Topics in Catalysis [11], Copyright 2013.

9.4. Using Pt/LnScO₃ for New Catalytic Reactions - Particle Strain Mismatch vs Support Basicity

The research proposed in the previous section will be essential towards understanding the relationship between strain mismatch and the Pt nanoparticle behavior, and following that work the Pt/LnScO₃ samples can be used to catalyze other reactions to determine the key properties that dictate performance of different reactions. In the Au/LnScO₃

system binding the intermediates was influenced by the 4f inductive effect while the Au was similar on all supports, if the Pt/LnScO₃ system is significantly influenced by the strain mismatch, both the strain and inductive effect can be probed in tandem.

Performance metrics (such as activation energy, rate, and selectivity) that depend heavily on the support basicity will have a minimum or maximum over Pt/NdScO₃, while metrics dependent on the strain mismatch will have an intermediate value over Pt/NdScO₃. However, it is likely that a combination of the basicity and strain mismatch impact catalytic performance metrics, and comparing SmScO₃ and LaScO₃ will help to deconvolute that combination since they have similar basicities but different lattice parameters. Adding GdScO₃ to the support library and performing similar CO₂ desorption measurements will also provide a fourth point of comparison. The research proposed in the previous section should be done first so it is known exactly which aspects of the Pt are changing from sample to sample when analyzing any catalytic results.

9.5. Synthetic Control of LnScO₃ Substrate Faceting

My final proposed project focuses on the synthesis of the LnScO₃ substrate materials. Previous work on SrTiO₃ nanoparticles demonstrated the ability to control which facet is primarily exposed using different alcohols as surfactants [104], and expanding this control to the LnScO₃ system will allow the inductive effect to be further explored and applied to affect catalytic performance.

In Chapter 4 the pseudocubic {100} facets of LnScO₃ were found to consist mostly of a Sc rich double layer termination, while the {110} type facets were single layer terminations. Despite two full Sc rich layers on the cuboidal substrates used in Chapter 7, the

inductive effect of the lanthanide was able to facilitate electron transfer and alter catalytic behavior. By synthesizing the LnScO_3 materials to preferentially expose the single layer $\{110\}$ type facets, the impact of the inductive effect should be amplified and generate a more significant impact on the catalytic performance.

As discussed at the end of Chapter 4, $\Delta\mu_{\text{Sc}_2\text{O}_3}$ will impact the thermodynamic Wulff shape of the nanoparticles. If $\Delta\mu_{\text{Sc}_2\text{O}_3}$ can be controlled, this should grant a degree of shape control over the products, allowing selectivity towards different faceting. As a first step, performing a detailed analysis of the experimental Wulff shapes produced by the current synthesis procedure will help determine $\Delta\mu_{\text{Sc}_2\text{O}_3}$ in current synthesis procedure. From there, adjustments can be made to either the relative concentrations of Sc precursor in solution or surfactants can be added, and their impact can be assessed via imaging of the particles and analysis of the produced shapes. However it should be noted that this comparison will not give exact values for $\Delta\mu_{\text{Sc}_2\text{O}_3}$, as the predicted shapes are thermodynamic and the synthesis certainly has a degree of kinetic influence.

Unlike the previous SrTiO_3 hydrothermal synthesis methods, the LnScO_3 particles are synthesized in an open flow, tube reactor [26]. As a result, the surfactants would be added to the bubbler solution to change the gas environment of the furnace. The surfaces of the new particles would need to be studied first, as new synthesis environments can change the reconstruction that forms.

References

- [1] D. B. Williams and C. B. Carter, *Transmission electron microscopy : a textbook for materials science*. New York: Springer, 2nd ed., 2009.
- [2] “Aberrations: Spherical and chromatic, <https://www.japanistry.com/aberrations/>,” Sep 2017.
- [3] E. J. Kirkland, “Image Simulation in Transmission Electron Microscopy,” in *Kavli summer school*, pp. 1–14, 2006.
- [4] J. A. Ascencio, M. Perez-Alvarez, S. Tehuacanero, and M. Jose-Yacaman, “Experimental and theoretical studies of instabilities of metal nanoparticles: a new kind of quasimelting,” *Applied Physics a-Materials Science & Processing*, vol. 73, no. 3, pp. 295–300, 2001.
- [5] N. P. Young, M. A. van Huis, H. W. Zandbergen, H. Xu, and A. I. Kirkland, “Transformations of gold nanoparticles investigated using variable temperature high-resolution transmission electron microscopy,” *Ultramicroscopy*, vol. 110, no. 5, pp. 506–516, 2010.
- [6] B. R. Chen, L. A. Crosby, C. George, R. M. Kennedy, N. M. Schweitzer, J. G. Wen, R. P. Van Duyne, P. C. Stair, K. R. Poepelmeier, L. D. Marks, and M. J. Bedzyk, “Morphology and CO oxidation activity of Pd nanoparticles on SrTiO₃ Nanopolyhedra,” *Acs Catalysis*, vol. 8, no. 6, pp. 4751–4760, 2018.
- [7] T. Akita, M. Kohyama, and M. Haruta, “Electron Microscopy Study of Gold Nanoparticles Deposited on Transition Metal Oxides,” *Accounts of Chemical Research*, vol. 46, no. 8, pp. 1773–1782, 2013.
- [8] N. Shibata, S. D. Findlay, Y. Kohno, H. Sawada, Y. Kondo, and Y. Ikuhara, “Differential phase-contrast microscopy at atomic resolution,” *Nature Physics*, vol. 8, no. 8, pp. 611–615, 2012.

- [9] P. B. Wells, "Characterization of the standard platinum/silica catalyst europt-1. 5. chemisorption of carbon monoxide and of oxygen," *Applied Catalysis*, vol. 18, no. 2, pp. 259–272, 1985.
- [10] C. Lentz, S. P. Jand, J. Melke, C. Roth, and P. Kaghazchi, "DRIFTS study of CO adsorption on Pt nanoparticles supported by DFT calculations," *Journal of Molecular Catalysis A: Chemical*, vol. 426, pp. 1–9, 2017.
- [11] J. A. Enterkin, R. M. Kennedy, J. Lu, J. W. Elam, R. E. Cook, L. D. Marks, P. C. Stair, C. L. Marshall, and K. R. Poeppelmeier, "Epitaxial stabilization of face selective catalysts," *Topics in Catalysis*, vol. 56, no. 18-20, pp. 1829–1834, 2013.
- [12] I. Chorkendorff and J. W. Niemantsverdriet, *Concepts of modern catalysis and kinetics*. Weinheim: Wiley-VCH, 2nd ed., 2007.
- [13] L. Liu and A. Corma, "Metal Catalysts for Heterogeneous Catalysis: From Single Atoms to Nanoclusters and Nanoparticles," *Chemical Reviews*, vol. 118, no. 10, pp. 4981–5079, 2018. PMID: 29658707.
- [14] M. Boudart, *Catalysis by supported metals*, vol. 20, pp. 153–166. Academic Press, 1969.
- [15] M. Boudart, "Heterogeneous Catalysis by Metals," *Journal of Molecular Catalysis*, vol. 30, no. 1-2, pp. 27–38, 1985.
- [16] M. Haruta, T. Kobayashi, H. Sano, and N. Yamada, "Novel Gold Catalysts for the Oxidation of Carbon-Monoxide at a Temperature Far Below 0°C," *Chemistry Letters*, no. 2, pp. 405–408, 1987.
- [17] M. Haruta, "Size- and support-dependency in the catalysis of gold," *Catalysis Today*, vol. 36, no. 1, pp. 153–166, 1997. Copper, Silver and Gold in Catalysis.
- [18] A. B. Stiles, *Catalyst supports and supported catalysts*. 1 1987.
- [19] F. Polo-Garzon, Z. Bao, X. Zhang, W. Huang, and Z. Wu, "Surface Reconstructions of Metal Oxides and the Consequences on Catalytic Chemistry," *ACS Catalysis*, vol. 9, no. 6, pp. 5692–5707, 2019.
- [20] G. A. Somorjai, "Surface Reconstruction and Catalysis," *Annual Review of Physical Chemistry*, vol. 45, no. 1, pp. 721–751, 1994.

- [21] S. J. Tauster, S. C. Fung, and R. L. Garten, "Strong metal-support interactions. Group 8 noble metals supported on titanium dioxide," *Journal of the American Chemical Society*, vol. 100, no. 1, pp. 170–175, 1978.
- [22] B.-R. Chen, C. George, Y. Lin, L. Hu, L. Crosby, X. Hu, P. C. Stair, L. D. Marks, K. R. Poeppelmeier, R. P. Van Duyne, and M. J. Bedzyk, "Morphology and oxidation state of ALD-grown Pd nanoparticles on TiO_2^- and SrO-terminated SrTiO_3 nanocuboids," *Surface Science*, vol. 648, pp. 291–298, 2016. Special issue dedicated to Gabor Somorjai's 80th birthday.
- [23] K. J. Kim, H. Han, T. Defferriere, D. Yoon, S. Na, S. J. Kim, A. M. Dayaghi, J. Son, T.-S. Oh, H. M. Jang, and G. M. Choi, "Facet-Dependent in Situ Growth of Nanoparticles in Epitaxial Thin Films: The Role of Interfacial Energy," *Journal of the American Chemical Society*, vol. 141, no. 18, pp. 7509–7517, 2019. PMID: 30998333.
- [24] Y. Lin, Z. Wu, J. Wen, K. Ding, X. Yang, K. R. Poeppelmeier, and L. D. Marks, "Adhesion and Atomic Structures of Gold on Ceria Nanostructures: The Role of Surface Structure and Oxidation State of Ceria Supports," *Nano Letters*, vol. 15, no. 8, pp. 5375–5381, 2015. PMID: 26222267.
- [25] R. J. Paull, Z. R. Mansley, T. Ly, L. D. Marks, and K. R. Poeppelmeier, "Synthesis of Gadolinium Scandate from a Hydroxide Hydrogel," *Inorganic Chemistry*, vol. 57, no. 7, pp. 4104–4108, 2018.
- [26] R. J. Paull, T. Ly, Z. R. Mansley, K. R. Poeppelmeier, and L. D. Marks, "Controlled Two-Step Formation of Faceted Perovskite Rare-Earth Scandate Nanoparticles," *Crystals*, vol. 9, no. 4, 2019.
- [27] G. Wulff, "On the question of speed of growth and dissolution of crystal surfaces.," *Zeitschrift Fur Krystallographie Und Mineralogie*, vol. 34, no. 5/6, pp. 449–530, 1901.
- [28] A. Dinghas, "On Wulff's geometric theorem for the balanced form of crystals," *Zeitschrift Fur Kristallographie*, vol. 105, no. 4, pp. 304–314, 1944.
- [29] M. V. Laue, "Der Wulffsche Satz für die Gleichgewichtsform von Kristallen," *Zeitschrift Fur Kristallographie*, vol. 105, pp. 124–133, 1943.
- [30] S. Ino, "Epitaxial Growth of Metals on Rocksalt Faces Cleaved in Vacuum. II. Orientation and Structure of Gold Particles Formed in Ultrahigh Vacuum," *Journal of the Physical Society of Japan*, vol. 21, no. 2, pp. 346–362, 1966.

- [31] W. L. Winterbottom, “Equilibrium shape of a small particle in contact with a foreign substrate,” *Acta Metallurgica*, vol. 15, no. 2, pp. 303–310, 1967.
- [32] Y. Jiang, Z. Chen, Y. Han, P. Deb, H. Gao, S. Xie, P. Purohit, M. W. Tate, J. Park, S. M. Gruner, V. Elser, and D. A. Muller, “Electron ptychography of 2D materials to deep sub-ångström resolution,” *Nature*, vol. 559, no. 7714, pp. 343–349, 2018.
- [33] J. M. Cowley, *Diffraction physics*. North-Holland personal library, Amsterdam ; New York: Elsevier Science B.V., 3rd rev. ed., 1995.
- [34] J. C. H. Spence, *High-resolution electron microscopy*. Oxford, United Kingdom ; New York, NY: Oxford University Press, fourth edition. ed., 2017.
- [35] L. M. Peng, S. L. Dudarev, and M. J. Whelan, *High-energy electron diffraction and microscopy*. Monographs on the physics and chemistry of materials, Oxford ; New York: Oxford University Press, 2004.
- [36] P. B. Hirsch, *Electron microscopy of thin crystals*. London,: Butterworths, 1965.
- [37] M. Haider, S. Uhlemann, E. Schwan, H. Rose, B. Kabius, and K. Urban, “Electron microscopy image enhanced,” *Nature*, vol. 392, no. 6678, pp. 768–769, 1998.
- [38] O. Scherzer, “Over some errors of electrons lenses.,” *Zeitschrift Fur Physik*, vol. 101, no. 5, pp. 593–603, 1936.
- [39] O. Scherzer, “The Theoretical Resolution Limit of the Electron Microscope,” *Journal of Applied Physics*, vol. 20, no. 1, pp. 20–29, 1949.
- [40] P. W. Hawkes, “Aberration correction past and present,” *Philosophical Transactions of the Royal Society a-Mathematical Physical and Engineering Sciences*, vol. 367, no. 1903, pp. 3637–3664, 2009.
- [41] L. D. Marks, “Lecture notes in Advanced Electron Microscopy,” Winter 2016.
- [42] P. Hohenberg and W. Kohn, “Inhomogeneous electron gas,” *Physical review*, vol. 136, no. 3B, p. B864, 1964.
- [43] W. Kohn and L. J. Sham, “Self-Consistent Equations Including Exchange and Correlation Effects,” *Phys. Rev.*, vol. 140, pp. A1133–A1138, Nov 1965.
- [44] P. Novák, J. Kuneš, L. Chaput, and W. E. Pickett, “Exact exchange for correlated electrons,” *physica status solidi (b)*, vol. 243, no. 3, pp. 563–572, 2006.

- [45] F. Tran, J. Kuneš, P. Novák, P. Blaha, L. D. Marks, and K. Schwarz, “Force calculation for orbital-dependent potentials with FP-(L)APW+lo basis sets,” *Computer Physics Communications*, vol. 179, no. 11, pp. 784–790, 2008.
- [46] P. Blaha, K. Schwarz, F. Tran, R. Laskowski, G. K. H. Madsen, and L. D. Marks, “WIEN2k: An APW+lo program for calculating the properties of solids,” *The Journal of Chemical Physics*, vol. 152, no. 7, p. 074101, 2020.
- [47] J. P. Perdew, A. Ruzsinszky, G. I. Csonka, O. A. Vydrov, G. E. Scuseria, L. A. Constantin, X. Zhou, and K. Burke, “Restoring the Density-Gradient Expansion for Exchange in Solids and Surfaces,” *Phys. Rev. Lett.*, vol. 100, p. 136406, Apr 2008.
- [48] J. P. Perdew, K. Burke, and M. Ernzerhof, “Generalized Gradient Approximation Made Simple,” *Phys. Rev. Lett.*, vol. 78, pp. 1396–1396, Feb 1997.
- [49] C. A. Mizzi, P. Koirala, and L. D. Marks, “Electronic structure of lanthanide scandates,” *Physical Review Materials*, vol. 2, no. 2, p. 025001, 2018.
- [50] M. Schmidbauer, A. Kwasniewski, and J. Schwarzkopf, “High-precision absolute lattice parameter determination of SrTiO₃, DyScO₃ and NdGaO₃ single crystals,” *Acta Crystallographica Section B*, vol. 68, pp. 8–14, Feb 2012.
- [51] R. E. Schlier and H. E. Farnsworth, “Structure and Adsorption Characteristics of Clean Surfaces of Germanium and Silicon,” *The Journal of Chemical Physics*, vol. 30, no. 4, pp. 917–926, 1959.
- [52] K. Takayanagi, Y. Tanishiro, S. Takahashi, and M. Takahashi, “Structure analysis of Si(111)-7 × 7 reconstructed surface by transmission electron diffraction,” *Surface Science*, vol. 164, no. 2, pp. 367–392, 1985.
- [53] P. J. Estrup, *Reconstruction of Metal Surfaces*, pp. 205–230. Berlin, Heidelberg: Springer Berlin Heidelberg, 1984.
- [54] L. D. Marks, “Direct Imaging of Carbon-Covered and Clean Gold (110) Surfaces,” *Physical Review Letters*, vol. 51, no. 11, pp. 1000–1002, 1983.
- [55] M. Van Hove, R. Koestner, P. Stair, J. Bibérian, L. Kesmodel, I. Bartoš, and G. Somorjai, “The surface reconstructions of the (100) crystal faces of iridium, platinum and gold: I. Experimental observations and possible structural models,” *Surface Science*, vol. 103, no. 1, pp. 189–217, 1981.

- [56] M. Van Hove, R. Koestner, P. Stair, J. Bibérian, L. Kesmodel, I. Bartoš, and G. Somorjai, “The surface reconstructions of the (100) crystal faces of iridium, platinum and gold: II. Structural determination by LEED intensity analysis,” *Surface Science*, vol. 103, no. 1, pp. 218–238, 1981.
- [57] C. B. Duke, “Semiconductor Surface Reconstruction: The Structural Chemistry of Two-Dimensional Surface Compounds,” *Chemical Reviews*, vol. 96, no. 4, pp. 1237–1260, 1996. PMID: 11848788.
- [58] G. P. Srivastava, “Theory of semiconductor surface reconstruction,” *Reports on Progress in Physics*, vol. 60, pp. 561–613, May 1997.
- [59] T. K. Andersen, D. D. Fong, and L. D. Marks, “Pauling’s rules for oxide surfaces,” *Surface Science Reports*, vol. 73, no. 5, pp. 213–232, 2018.
- [60] P. W. Murray, F. M. Leibsle, H. J. Fisher, C. F. J. Flipse, C. A. Muryn, and G. Thornton, “Observation of ordered oxygen vacancies on $\text{TiO}_2(100)1\times 3$ using scanning tunneling microscopy and spectroscopy,” *Phys. Rev. B*, vol. 46, pp. 12877–12879, Nov 1992.
- [61] Y. Wang, O. Warschkow, and L. D. Marks, “Surface evolution of rutile TiO_2 (100) in an oxidizing environment,” *Surface Science*, vol. 601, no. 1, pp. 63–67, 2007.
- [62] D. Kienzle, P. Koirala, and L. Marks, “Lanthanum aluminate (110) 3×1 surface reconstruction,” *Surface Science*, vol. 633, pp. 60–67, 2015.
- [63] C. H. Lanier, J. M. Rondinelli, B. Deng, R. Kilaas, K. R. Poeppelmeier, and L. D. Marks, “Surface Reconstruction with a Fractional Hole: $(\sqrt{5} \times \sqrt{5})R26.6^\circ$ LaAlO_3 (001),” *Phys. Rev. Lett.*, vol. 98, p. 086102, Feb 2007.
- [64] H. Nörenberg and J. Harding, “The surface structure of $\text{CeO}_2(001)$ single crystals studied by elevated temperature STM,” *Surface Science*, vol. 477, no. 1, pp. 17–24, 2001.
- [65] T. Ly, J. Wen, and L. D. Marks, “Kinetic Growth Regimes of Hydrothermally Synthesized Potassium Tantalate Nanoparticles,” *Nano Letters*, vol. 18, no. 8, pp. 5186–5191, 2018. PMID: 29975544.
- [66] N. Nakagawa, H. Y. Hwang, and D. A. Muller, “Why some interfaces cannot be sharp,” *Nature Materials*, vol. 5, no. 3, pp. 204–209, 2006.
- [67] C. H. Lee, V. Skoromets, M. D. Biegalski, S. M. Lei, R. Haislmaier, M. Bernhagen, R. Uecker, X. X. Xi, V. Gopalan, X. Marti, S. Kamba, P. Kuzel, and D. G.

- Schlom, "Effect of stoichiometry on the dielectric properties and soft mode behavior of strained epitaxial SrTiO₃ thin films on DyScO₃ substrates," *Applied Physics Letters*, vol. 102, no. 8, p. 082905, 2013.
- [68] S. Karimoto and M. Naito, "Electron-doped infinite-layer thin films with T-C over 40 K grown on DyScO₃ substrates," *Applied Physics Letters*, vol. 84, no. 12, pp. 2136–2138, 2004.
- [69] S. Hu, Z. Yue, J. S. Lim, S. J. Callori, J. Bertinshaw, A. Ikeda-Ohno, T. Ohkochi, C. H. Yang, X. Wang, C. Ulrich, and J. Seidel, "Growth and Properties of Fully Strained SrCoO_x (x approximate to 2.8) Thin Films on DyScO₃," *Advanced Materials Interfaces*, vol. 2, no. 8, p. 1500012, 2015.
- [70] J. H. Haeni, P. Irvin, W. Chang, R. Uecker, P. Reiche, Y. L. Li, S. Choudhury, W. Tian, M. E. Hawley, B. Craigo, A. K. Tagantsev, X. Q. Pan, S. K. Streiffer, L. Q. Chen, S. W. Kirchoefer, J. Levy, and D. G. Schlom, "Room-temperature ferroelectricity in strained SrTiO₃," *Nature*, vol. 430, no. 7001, pp. 758–761, 2004.
- [71] E. M. Kneedler, B. T. Jonker, P. M. Thibado, R. J. Wagner, B. V. Shanabrook, and L. J. Whitman, "Influence of substrate surface reconstruction on the growth and magnetic properties of Fe on GaAs(001)," *Physical Review B*, vol. 56, no. 13, pp. 8163–8168, 1997.
- [72] S. Cook, K. Letchworth-Weaver, I. C. Tung, T. K. Andersen, H. Hong, L. D. Marks, and D. D. Fong, "How heteroepitaxy occurs on strontium titanate," *Science Advances*, vol. 5, no. 4, 2019.
- [73] A. Biswas, C. H. Yang, R. Ramesh, and M. H. Jeong, "Atomically flat single terminated oxide substrate surfaces," *Progress in Surface Science*, vol. 92, no. 2, pp. 117–141, 2017.
- [74] M. Kawasaki, K. Takahashi, T. Maeda, R. Tsuchiya, M. Shinohara, O. Ishiyama, T. Yonezawa, M. Yoshimoto, and H. Koinuma, "Atomic Control of the SrTiO₃ Crystal Surface," *Science*, vol. 266, no. 5190, pp. 1540–1542, 1994.
- [75] J. Yeh and I. Lindau, "Atomic subshell photoionization cross sections and asymmetry parameters: $1 \leq Z \leq 103$," *Atomic Data and Nuclear Data Tables*, vol. 32, no. 1, pp. 1–155, 1985.
- [76] U. Fano and J. W. Cooper, "Spectral Distribution of Atomic Oscillator Strengths," *Rev. Mod. Phys.*, vol. 40, pp. 441–507, Jul 1968.

- [77] J. W. Cooper, "Photoionization from Outer Atomic Subshells. A Model Study," *Phys. Rev.*, vol. 128, pp. 681–693, Oct 1962.
- [78] F. Herman and S. Skillman, *Atomic structure calculations*. Prentice-Hall, 1963.
- [79] C. Fadley, R. Baird, W. Siekhaus, T. Novakov, and S. Bergström, "Surface analysis and angular distributions in x-ray photoelectron spectroscopy," *Journal of Electron Spectroscopy and Related Phenomena*, vol. 4, no. 2, pp. 93–137, 1974.
- [80] T. A. Carlson and G. McGuire, "Study of the x-ray photoelectron spectrum of tungsten—tungsten oxide as a function of thickness of the surface oxide layer," *Journal of Electron Spectroscopy and Related Phenomena*, vol. 1, no. 2, pp. 161–168, 1972.
- [81] E. McCafferty and J. Wightman, "An X-ray photoelectron spectroscopy sputter profile study of the native air-formed oxide film on titanium," *Applied Surface Science*, vol. 143, no. 1, pp. 92–100, 1999.
- [82] L. Pauling, "The principles determining the structure of complex ionic crystals," *Journal of the American Chemical Society*, vol. 51, no. 1-4, pp. 1010–1026, 1929.
- [83] C. A. Mizzi, P. Koirala, A. Gulec, and L. D. Marks, "Charging ain't all bad: Complex physics in DyScO₃," *Ultramicroscopy*, vol. 203, pp. 119–124, 2019.
- [84] Z. R. Mansley, C. A. Mizzi, P. Koirala, J. Wen, and L. D. Marks, "Structure of the (110) LnScO₃ (Ln=Gd,Tb,Dy) surfaces," *Physical Review Materials*, vol. 4, no. 4, p. 045003, 2020.
- [85] L. D. Marks and D. J. Smith, "Direct Surface Imaging in Small Metal Particles," *Nature*, vol. 303, no. 5915, pp. 316–317, 1983.
- [86] L. D. Marks, "Direct Atomic Imaging of Solid-Surfaces .1. Image Simulation and Interpretation," *Surface Science*, vol. 139, no. 1, pp. 281–298, 1984.
- [87] Y. Lin, J. Wen, L. Hu, R. M. Kennedy, P. C. Stair, K. R. Poeppelmeier, and L. D. Marks, "Synthesis-dependent atomic surface structures of oxide nanoparticles," *Phys Rev Lett*, vol. 111, no. 15, p. 156101, 2013.
- [88] Y. Y. Lin, Z. L. Wu, J. G. Wen, K. R. Poeppelmeier, and L. D. Marks, "Imaging the Atomic Surface Structures of CeO₂ Nanoparticles," *Nano Letters*, vol. 14, no. 1, pp. 191–196, 2014.

- [89] W. Zhang and W. T. Zheng, "Transmission electron microscopy finds plenty of room on the surface," *Physical Chemistry Chemical Physics*, vol. 17, no. 22, pp. 14461–14469, 2015.
- [90] W. T. Yuan, Y. Wang, H. B. Li, H. L. Wu, Z. Zhang, A. Selloni, and C. H. Sun, "Real-Time Observation of Reconstruction Dynamics on $\text{TiO}_2(001)$ Surface under Oxygen via an Environmental Transmission Electron Microscope," *Nano Letters*, vol. 16, no. 1, pp. 132–137, 2016.
- [91] W. T. Yuan, H. L. Wu, H. B. Li, Z. X. Dai, Z. Zhang, C. H. Sun, and Y. Wang, "In Situ STEM Determination of the Atomic Structure and Reconstruction Mechanism of the $\text{TiO}_2(001)$ (1 x 4) Surface," *Chemistry of Materials*, vol. 29, no. 7, pp. 3189–3194, 2017.
- [92] M. Ek, I. Beinik, A. Bruix, S. Wendt, J. V. Lauritsen, and S. Helveg, "Step edge structures on the anatase $\text{TiO}_2(001)$ surface studied by atomic-resolution TEM and STM," *Faraday Discussions*, vol. 208, pp. 325–338, 2018.
- [93] L. H. Liu, Z. Y. Cheng, J. Zhu, and R. Yu, "Flexible Cation Distribution for Stabilizing a Spinel Surface," *Journal of Physical Chemistry C*, vol. 124, no. 30, pp. 16431–16438, 2020.
- [94] D. W. Hoffman and J. W. Cahn, "Vector Thermodynamics for Anisotropic Surfaces .1. Fundamentals and Application to Plane Surface Junctions," *Surface Science*, vol. 31, no. 1, pp. 368–388, 1972.
- [95] J. W. Cahn and D. W. Hoffman, "Vector Thermodynamics for Anisotropic Surfaces .2. Curved and Faceted Surfaces," *Acta Metallurgica*, vol. 22, no. 10, pp. 1205–1214, 1974.
- [96] L. D. Marks and L. Peng, "Nanoparticle shape, thermodynamics and kinetics," *Journal of Physics: Condensed Matter*, vol. 28, no. 5, pp. 053001–053001, 2016.
- [97] L. D. Marks, "Modified Wulff constructions for twinned particles," *Journal of Crystal Growth*, vol. 61, no. 3, pp. 556–566, 1983.
- [98] L. D. Marks, "Surface structure and energetics of multiply twinned particles," *Philosophical Magazine A: Physics of Condensed Matter, Structure, Defects and Mechanical Properties*, vol. 49, no. 1, pp. 81–93, 1984.
- [99] A. Howie and L. D. Marks, "Elastic strains and the energy balance for multiply twinned particles," *Philosophical Magazine A: Physics of Condensed Matter, Structure, Defects and Mechanical Properties*, vol. 49, no. 1, pp. 95–109, 1984.

- [100] R. G. Chaudhuri and S. Paria, "Core/Shell Nanoparticles: Classes, Properties, Synthesis Mechanisms, Characterization, and Applications," *Chemical Reviews*, vol. 112, no. 4, pp. 2373–2433, 2012.
- [101] P. G. de Gennes, "Soft Matter (Nobel Lecture)," *Angewandte Chemie International Edition in English*, vol. 31, no. 7, pp. 842–845, 1992.
- [102] M. Lattuada and T. A. Hatton, "Synthesis, properties and applications of Janus nanoparticles," *Nano Today*, vol. 6, no. 3, pp. 286–308, 2011.
- [103] C. T. Dinh, T. D. Nguyen, F. Kleitz, and T. O. Do, "Shape-Controlled Synthesis of Highly Crystalline Titania Nanocrystals," *Acs Nano*, vol. 3, no. 11, pp. 3737–3743, 2009.
- [104] L. Q. Dong, H. Shi, K. Cheng, Q. Wang, W. J. Weng, and W. Q. Han, "Shape-controlled growth of SrTiO₃ polyhedral submicro/nanocrystals," *Nano Research*, vol. 7, no. 9, pp. 1311–1318, 2014.
- [105] X. H. Liu, G. Z. Qiu, and X. G. Li, "Shape-controlled synthesis and properties of uniform spinel cobalt oxide nanocubes," *Nanotechnology*, vol. 16, no. 12, pp. 3035–3040, 2005.
- [106] C. H. B. Ng and W. Y. Fan, "Shape evolution of Cu₂O nanostructures via kinetic and thermodynamic controlled growth," *Journal of Physical Chemistry B*, vol. 110, no. 42, pp. 20801–20807, 2006.
- [107] Y. Qi, T. Bian, S. I. Choi, Y. Y. Jiang, C. H. Jin, M. S. Fu, H. Zhang, and D. R. Yang, "Kinetically controlled synthesis of Pt-Cu alloy concave nanocubes with high-index facets for methanol electro-oxidation," *Chemical Communications*, vol. 50, no. 5, pp. 560–562, 2014.
- [108] Y. G. Sun and Y. N. Xia, "Shape-controlled synthesis of gold and silver nanoparticles," *Science*, vol. 298, no. 5601, pp. 2176–2179, 2002.
- [109] W. W. Wang and Y. J. Zhu, "Shape-controlled synthesis of zinc oxide by microwave heating using an imidazolium salt," *Inorganic Chemistry Communications*, vol. 7, no. 9, pp. 1003–1005, 2004.
- [110] Y. G. Wang, G. Xu, L. L. Yang, Z. H. Ren, X. Wei, W. J. Weng, P. Y. Du, G. Shen, and G. R. Han, "Formation of single-crystal SrTiO₃ dendritic nanostructures via a simple hydrothermal method," *Journal of Crystal Growth*, vol. 311, no. 8, pp. 2519–2523, 2009.

- [111] Y. N. Xia, X. H. Xia, and H. C. Peng, "Shape-Controlled Synthesis of Colloidal Metal Nanocrystals: Thermodynamic versus Kinetic Products," *Journal of the American Chemical Society*, vol. 137, no. 25, pp. 7947–7966, 2015.
- [112] Y. J. Xiong, J. M. McLellan, J. Y. Chen, Y. D. Yin, Z. Y. Li, and Y. N. Xia, "Kinetically controlled synthesis of triangular and hexagonal nanoplates of palladium and their SPR/SERS properties," *Journal of the American Chemical Society*, vol. 127, no. 48, pp. 17118–17127, 2005.
- [113] L. L. Yang, Y. J. Wang, Q. Q. Zou, and Y. G. Wang, "Effect of temperature and KOH concentration on hydrothermal synthesis of SrTiO₃ dendrites," *Frontiers of Advanced Materials and Engineering Technology, Pts 1-3*, vol. 430-432, p. 225, 2012.
- [114] J. K. Yuan, W. N. Li, S. Gomez, and S. L. Suib, "Shape-controlled synthesis of manganese oxide octahedral molecular sieve three-dimensional nanostructures," *Journal of the American Chemical Society*, vol. 127, no. 41, pp. 14184–14185, 2005.
- [115] S. Ino and S. Ogawa, "Multiply Twinned Particles at Earlier Stages of Gold Film Formation on Alkali Halide Crystals," *Journal of the Physical Society of Japan*, vol. 22, no. 6, pp. 1365–1374, 1967.
- [116] J. B. Park, S. F. Conner, and D. A. Chen, "Bimetallic Pt-Au clusters on TiO₂(110): Growth, surface composition, and metal-support interactions," *Journal of Physical Chemistry C*, vol. 112, no. 14, pp. 5490–5500, 2008.
- [117] J. Y. Park, Y. Zhang, M. Grass, T. Zhang, and G. A. Somorjai, "Tuning of catalytic CO oxidation by changing composition of Rh-Pt bimetallic nanoparticles," *Nano Letters*, vol. 8, no. 2, pp. 673–677, 2008.
- [118] J. A. Enterkin, W. Setthapun, J. W. Elam, S. T. Christensen, F. A. Rabuffetti, L. D. Marks, P. C. Stair, K. R. Poeppelmeier, and C. L. Marshall, "Propane oxidation over Pt/SrTiO₃ nanocuboids," *ACS Catalysis*, vol. 1, no. 6, pp. 629–635, 2011.
- [119] J. A. Enterkin, K. K. R. Poeppelmeier, and L. L. D. Marks, "Oriented Catalytic Platinum Nanoparticles on High Surface Area Strontium Titanate Nanocuboid Surfaces," *Nanoletters*, vol. 11, no. 11, pp. 993–997, 2011.
- [120] M. P. Neupane, I. S. Park, T. S. Bae, H. K. Yi, M. Uo, F. Watari, and M. H. Lee, "Titania nanotubes supported gelatin stabilized gold nanoparticles for medical implants," *Journal of Materials Chemistry*, vol. 21, no. 32, pp. 12078–12082, 2011.

- [121] M. Malakootian, A. Nasiri, and M. A. Gharaghani, "Photocatalytic degradation of ciprofloxacin antibiotic by TiO₂ nanoparticles immobilized on a glass plate," *Chemical Engineering Communications*, vol. 207, no. 1, pp. 56–72, 2020.
- [122] Z. R. Mansley and L. D. Marks, "Modified Winterbottom Construction Including Boundaries," *Journal of Physical Chemistry C*, vol. 124, no. 51, pp. 28038–28043, 2020.
- [123] R. Zanella, S. Giorgio, C. H. Shin, C. R. Henry, and C. Louis, "Characterization and reactivity in CO oxidation of gold nanoparticles supported on TiO₂ prepared by deposition-precipitation with NaOH and urea," *Journal of Catalysis*, vol. 222, no. 2, pp. 357–367, 2004.
- [124] S. Patala, L. D. Marks, and M. Olvera de la Cruz, "Thermodynamic Analysis of Multiply Twinned Particles: Surface Stress Effects," *The Journal of Physical Chemistry Letters*, vol. 4, no. 18, pp. 3089–3094, 2013.
- [125] P. M. Ajayan and L. D. Marks, "Phase instabilities in small particles," *Phase Transitions*, vol. 24-26, no. 1, pp. 229–258, 1990.
- [126] S. Ino, "Stability of Multiply-Twinned Particles," *Journal of the Physical Society of Japan*, vol. 27, no. 4, pp. 941–953, 1969.
- [127] C. L. Cleveland and U. Landman, "The energetics and structure of nickel clusters: Size dependence," *The Journal of Chemical Physics*, vol. 94, no. 11, pp. 7376–7396, 1991.
- [128] V. G. Gryaznov, A. M. Kaprelov, A. E. Romanov, and I. A. Polonskii, "Channels of Relaxation of Elastic Stresses in Pentagonal Nanoparticles," *physica status solidi (b)*, vol. 167, no. 2, pp. 441–450, 1991.
- [129] C. L. Johnson, E. Snoeck, M. Ezcurdia, B. Rodríguez-González, I. Pastoriza-Santos, L. M. Liz-Marzán, and M. J. Hÿtch, "Effects of elastic anisotropy on strain distributions in decahedral gold nanoparticles," *Nature Materials*, vol. 7, no. 2, pp. 120–124, 2008.
- [130] S. Patala, L. D. Marks, and M. Olvera de la Cruz, "Elastic Strain Energy Effects in Faceted Decahedral Nanoparticles," *The Journal of Physical Chemistry C*, vol. 117, no. 3, pp. 1485–1494, 2013.
- [131] G. D. Barmparis and I. N. Remediakis, "First-principles atomistic Wulff constructions for gold nanoparticles," *arXiv:1111.4667*, pp. 1–6, nov 2011.

- [132] C. R. Berry, "Electron Diffraction from Small Crystals," *Phys. Rev.*, vol. 88, pp. 596–599, Nov 1952.
- [133] H. Wasserman and J. Vermaak, "On the determination of a lattice contraction in very small silver particles," *Surface Science*, vol. 22, no. 1, pp. 164–172, 1970.
- [134] Q. Jiang, L. H. Liang, and D. S. Zhao, "Lattice Contraction and Surface Stress of fcc Nanocrystals," *The Journal of Physical Chemistry B*, vol. 105, no. 27, pp. 6275–6277, 2001.
- [135] W. H. Qi and M. P. Wang, "Size and shape dependent lattice parameters of metallic nanoparticles," *Journal of Nanoparticle Research*, vol. 7, no. 1, pp. 51–57, 2005.
- [136] I. N. Leontyev, A. B. Kuriganova, N. G. Leontyev, L. Hennem, A. Rakhmatullin, N. V. Smirnova, and V. Dmitriev, "Size dependence of the lattice parameters of carbon supported platinum nanoparticles: X-ray diffraction analysis and theoretical considerations," *RSC Adv.*, vol. 4, pp. 35959–35965, 2014.
- [137] B. Hammer and J. K. Norskov, "Why Gold Is the Noblest of All the Metals," *Nature*, vol. 376, no. 6537, pp. 238–240, 1995.
- [138] R. Meyer, C. Lemire, S. K. Shaikhutdinov, and H. Freund, "Surface chemistry of catalysis by gold," *Gold Bulletin*, vol. 37, no. 1-2, pp. 72–124, 2004.
- [139] L. Molina and B. Hammer, "Some recent theoretical advances in the understanding of the catalytic activity of Au," *Applied Catalysis A: General*, vol. 291, no. 1, pp. 21–31, 2005. Catalysis by Gold.
- [140] F. B. Noronha, E. C. Fendley, R. R. Soares, W. E. Alvarez, and D. E. Resasco, "Correlation between catalytic activity and support reducibility in the CO₂ reforming of methane over Pt/Ce_xZr_{1-x}O₂ catalysts," *Chemical Engineering Journal*, vol. 82, no. 1, pp. 21–31, 2001.
- [141] D. Widmann, Y. Liu, F. Schüth, and R. Behm, "Support effects in the Au-catalyzed CO oxidation – Correlation between activity, oxygen storage capacity, and support reducibility," *Journal of Catalysis*, vol. 276, no. 2, pp. 292–305, 2010.
- [142] M. Comotti, W. C. Li, B. Spliethoff, and F. Schuth, "Support effect in high activity gold catalysts for CO oxidation," *Journal of the American Chemical Society*, vol. 128, no. 3, pp. 917–924, 2006.

- [143] M. Sankar, Q. He, R. V. Engel, M. A. Sainna, A. J. Logsdail, A. Roldan, D. J. Willock, N. Agarwal, C. J. Kiely, and G. J. Hutchings, "Role of the Support in Gold-Containing Nanoparticles as Heterogeneous Catalysts," *Chemical Reviews*, vol. 120, no. 8, pp. 3890–3938, 2020.
- [144] E. D. Park and J. S. Lee, "Effects of pretreatment conditions on CO oxidation over supported Au catalysts," *Journal of Catalysis*, vol. 186, no. 1, pp. 1–11, 1999.
- [145] O. S. Alexeev, S. Y. Chin, M. H. Engelhard, L. Ortiz-Soto, and M. D. Amiridis, "Effects of reduction temperature and metal-support interactions on the catalytic activity Pt/ γ -Al₂O₃ and Pt/TiO₂ for the oxidation of CO in the presence and absence of H₂," *Journal of Physical Chemistry B*, vol. 109, no. 49, pp. 23430–23443, 2005.
- [146] A. Schlapka, M. Lischka, A. Gross, U. Kasberger, and P. Jakob, "Surface strain versus substrate interaction in heteroepitaxial metal layers: Pt on Ru(0001)," *Physical Review Letters*, vol. 91, no. 1, p. 016101, 2003.
- [147] K. Yan, T. A. Maark, A. Khorshidi, V. A. Sethuraman, A. A. Peterson, and P. R. Guduru, "The Influence of Elastic Strain on Catalytic Activity in the Hydrogen Evolution Reaction," *Angewandte Chemie-International Edition*, vol. 55, no. 21, pp. 6175–6181, 2016.
- [148] N. S. Lu, X. Wang, Z. G. Suo, and J. Vlassak, "Failure by simultaneous grain growth, strain localization, and interface debonding in metal films on polymer substrates," *Journal of Materials Research*, vol. 24, no. 2, pp. 379–385, 2009.
- [149] G. S. Foo, G. X. Hu, Z. D. Hood, M. J. Li, D. E. Jiang, and Z. L. Wu, "Kinetics and Mechanism of Methanol Conversion over Anatase Titania Nanoshapes," *Acs Catalysis*, vol. 7, no. 8, pp. 5345–5356, 2017.
- [150] G. S. Foo, Z. D. Hood, and Z. L. Wu, "Shape Effect Undermined by Surface Reconstruction: Ethanol Dehydrogenation over Shape-Controlled SrTiO₃ Nanocrystals," *Acs Catalysis*, vol. 8, no. 1, pp. 555–565, 2018.
- [151] V. Komanicky, H. Iddir, K. C. Chang, A. Menzel, G. Karapetrov, D. Hennessy, P. Zapol, and H. You, "Shape-Dependent Activity of Platinum Array Catalyst," *Journal of the American Chemical Society*, vol. 131, no. 16, pp. 5732–5733, 2009.
- [152] A. K. P. Mann, Z. L. Wu, F. C. Calaza, and S. H. Overbury, "Adsorption and Reaction of Acetaldehyde on Shape-Controlled CeO₂ Nanocrystals: Elucidation of Structure-Function Relationships," *Acs Catalysis*, vol. 4, no. 8, pp. 2437–2448, 2014.

- [153] V. Jalan and E. J. Taylor, "Importance of Interatomic Spacing in Catalytic Reduction of Oxygen in Phosphoric-Acid," *Journal of the Electrochemical Society*, vol. 130, no. 11, pp. 2299–2301, 1983.
- [154] M. Gsell, P. Jakob, and D. Menzel, "Effect of substrate strain on adsorption," *Science*, vol. 280, no. 5364, pp. 717–720, 1998.
- [155] M. Escudero-Escribano, P. Malacrida, M. H. Hansen, U. G. Vej-Hansen, A. Velazquez-Palenzuela, V. Tripkovic, J. Schiotz, J. Rossmeisl, I. E. L. Stephens, and I. Chorkendorff, "Tuning the activity of Pt alloy electrocatalysts by means of the lanthanide contraction," *Science*, vol. 352, no. 6281, pp. 73–76, 2016.
- [156] A. Khorshidi, J. Violet, J. Hashemi, and A. A. Peterson, "How strain can break the scaling relations of catalysis," *Nature Catalysis*, vol. 1, no. 4, pp. 263–268, 2018.
- [157] R. T. Haasch, E. Breckenfeld, and L. W. Martin, "An Introduction to Single Crystal Perovskites and Single Crystal Rare-Earth Scandate Perovskites Analyzed Using X-ray Photoelectron Spectroscopy," *Surface Science Spectra*, vol. 21, no. 1, pp. 84–86, 2014.
- [158] R. T. Haasch, L. W. Martin, and E. Breckenfeld, "Single Crystal Rare-earth Scandate Perovskites Analyzed Using X-ray Photoelectron Spectroscopy: 2. NdScO₃(110)," *Surface Science Spectra*, vol. 21, no. 1, pp. 140–148, 2014.
- [159] L. M. Molina and B. Hammer, "Active role of oxide support during CO oxidation at Au/MgO," *Physical Review Letters*, vol. 90, no. 20, p. 206102, 2003.
- [160] L. M. Molina and B. Hammer, "Theoretical study of CO oxidation on Au nanoparticles supported by MgO(100)," *Phys. Rev. B*, vol. 69, p. 155424, Apr 2004.
- [161] L. M. Molina, M. D. Rasmussen, and B. Hammer, "Adsorption of O₂ and oxidation of CO at Au nanoparticles supported by TiO₂(110)," *Journal of Chemical Physics*, vol. 120, no. 16, pp. 7673–7680, 2004.
- [162] P. Schlexer, D. Widmann, R. J. Behm, and G. Pacchioni, "CO Oxidation on a Au/TiO₂ Nanoparticle Catalyst via the Au-Assisted Mars-van Krevelen Mechanism," *Acs Catalysis*, vol. 8, no. 7, pp. 6513–6525, 2018.
- [163] H. Y. Kim, H. M. Lee, and G. Henkelman, "CO Oxidation Mechanism on CeO₂-Supported Au Nanoparticles," *Journal of the American Chemical Society*, vol. 134, no. 3, pp. 1560–1570, 2012.

- [164] N. C. for Biotechnology Information, "PubChem Compound Summary for CID 5460578, Oxidoperoxidocarbonate(.1-).," 2021.
- [165] H. Huber, D. McIntosh, and G. A. Ozin, "Metal Atom Model for Oxidation of Carbon-Monoxide to Carbon-Dioxide - Gold Atom Carbon Monoxide Dioxygen Reaction and Gold Atom Carbon Dioxide Reaction," *Inorganic Chemistry*, vol. 16, no. 5, pp. 975–979, 1977.
- [166] Z. P. Liu, P. Hu, and A. Alavi, "Catalytic role of gold in gold-based catalysts: A density functional theory study on the CO oxidation on gold," *Journal of the American Chemical Society*, vol. 124, no. 49, pp. 14770–14779, 2002.
- [167] Q. G. Jiang, J. F. Zhang, Z. M. Ao, H. J. Huang, H. Y. He, and Y. P. Wu, "First Principles Study on the CO Oxidation on Mn-Embedded Divacancy Graphene," *Frontiers in Chemistry*, vol. 6, 2018.
- [168] T. Davran-Candan, M. Demir, and R. Yildirim, "Analysis of reaction mechanisms and kinetics of preferential CO oxidation over Au/ γ -Al₂O₃," *Reaction Kinetics Mechanisms and Catalysis*, vol. 104, no. 2, pp. 389–398, 2011.
- [169] D. Y. Tang and J. Zhang, "Theoretical investigation on CO oxidation catalyzed by a copper nanocluster," *Rsc Advances*, vol. 3, no. 35, pp. 15225–15236, 2013.
- [170] J. Hagen, L. D. Socaciu, M. Elijazyfer, U. Heiz, T. M. Bernhardt, and L. Woste, "Coadsorption of CO and O₂ on small free gold cluster anions at cryogenic temperatures: Model complexes for catalytic CO oxidation," *Physical Chemistry Chemical Physics*, vol. 4, no. 10, pp. 1707–1709, 2002.
- [171] D. J. Burnett, A. T. Capitano, A. M. Gabelnick, A. L. Marsh, D. A. Fischer, and J. L. Gland, "In-situ soft X-ray studies of CO oxidation on the Pt(111) surface," *Surface Science*, vol. 564, no. 1, pp. 29–37, 2004.
- [172] Z. R. Mansley, R. J. Paull, L. Savereide, S. Tatro, E. P. Greenstein, A. Gosavi, E. Cheng, J. Wen, K. R. Poeppelmeier, J. M. Notestein, and L. D. Marks, "Identifying Support Effects in Au-Catalyzed CO Oxidation," *ACS Catalysis*, vol. 11, no. 19, pp. 11921–11928, 2021.
- [173] R. F. W. Bader, "A quantum theory of molecular structure and its applications," *Chemical Reviews*, vol. 91, no. 5, pp. 893–928, 1991.
- [174] F. Ernst, "Metal-oxide interfaces," *Materials Science and Engineering: R: Reports*, vol. 14, no. 3, pp. 97–156, 1995.

- [175] Q. Fu and T. Wagner, “Interaction of nanostructured metal overlayers with oxide surfaces,” *Surface Science Reports*, vol. 62, no. 11, pp. 431–498, 2007.
- [176] D. Duffy, J. Harding, and A. Stoneham, “Atomistic modelling of the metal/oxide interface with image interactions,” *Acta Metallurgica et Materialia*, vol. 40, pp. S11–S16, 1992.
- [177] J. Goniakowski, “Electronic structure of MgO-supported palladium films: Influence of the adsorption site,” *Phys. Rev. B*, vol. 57, pp. 1935–1941, Jan 1998.
- [178] J. Goniakowski, C. Mottet, and C. Noguera, “Non-reactive metal/oxide interfaces: from model calculations towards realistic simulations,” *physica status solidi (b)*, vol. 243, no. 11, pp. 2516–2532, 2006.
- [179] G. Pacchioni and N. Rösch, “Supported nickel and copper clusters on MgO(100): A first-principles calculation on the metal/oxide interface,” *The Journal of Chemical Physics*, vol. 104, no. 18, pp. 7329–7337, 1996.
- [180] E. Tea, J. Huang, G. Li, and C. Hin, “Atomic bonding and electrical potential at metal/oxide interfaces, a first principle study,” *The Journal of Chemical Physics*, vol. 146, no. 12, p. 124706, 2017.
- [181] L. Xu and G. Henkelman, “Calculations of Ca adsorption on a MgO(100) surface: Determination of the binding sites and growth mode,” *Phys. Rev. B*, vol. 77, p. 205404, May 2008.
- [182] D. A. Muller, D. A. Shashkov, R. Benedek, L. H. Yang, J. Silcox, and D. N. Seidman, “Atomic scale observations of metal-induced gap states at (222)MgO/Cu interfaces,” *Physical Review Letters*, vol. 80, no. 21, pp. 4741–4744, 1998.
- [183] S. Choi, D.-H. Lee, S. G. Louie, and J. Clarke, “Localization of Metal-Induced Gap States at the Metal-Insulator Interface: Origin of Flux Noise in SQUIDS and Superconducting Qubits,” *Phys. Rev. Lett.*, vol. 103, p. 197001, Nov 2009.
- [184] S. Andersson, P. Brühwiler, A. Sandell, M. Frank, J. Libuda, A. Giertz, B. Brena, A. Maxwell, M. Bäumer, H.-J. Freund, and N. Mårtensson, “Metal–oxide interaction for metal clusters on a metal-supported thin alumina film,” *Surface Science*, vol. 442, no. 1, pp. L964–L970, 1999.
- [185] J.-R. Huo, L. Li, H.-X. Cheng, X.-X. Wang, G.-H. Zhang, and P. Qian, “The structural, electronic and optical properties of Au–ZnO interface structure from the first-principles calculation,” *Modern Physics Letters B*, vol. 32, no. 07, p. 1850107, 2018.

- [186] H. Li, M. Saito, C. Chen, K. Inoue, K. Akagi, and Y. Ikuhara, “Strong metal–metal interaction and bonding nature in metal/oxide interfaces with large mismatches,” *Acta Materialia*, vol. 179, pp. 237–246, 2019.
- [187] L. D. Marks, *The Structure of Small Silver Particles*. PhD thesis, University of Cambridge, Cambridge, England, 1980.

APPENDIX A

Surface Energy Minimization Proof

This proof is modeled Appendix 3.2 in Prof. L. Marks's thesis [187], which is a translation of the proof by von Laue [29], and is also published as the Supporting Information of the reference [122]. It differs from the original owing to the inclusion of a 3rd type of “surface” as the interface. First consider the crystallites as separate entities with their own origins. Defining variables, we have distances m_i as normal distances from the origin to an external surface, n_j as the normal distance from the origin to a twin boundary, and p_k as the normal distance to the interface. External surface areas are M_i , twin surface areas are N_j , and the interfacial areas are P_k ; and they will have energies of γ_i , γ_{twin} , and γ_{eff} respectively.

We can now write the total surface energy (S) and the total volume (V) of the system as:

$$(A.1) \quad S = \sum_i \gamma_i M_i + \sum_j \gamma_{twin} N_j + \sum_k \gamma_{eff} P_k$$

$$(A.2) \quad V = \frac{1}{3} \left(\sum_i m_i M_i + \sum_j (n_j N_j + n'_j N'_j) + \sum_k p_k P_k \right)$$

where n'_j and N'_j are the contributions to twin boundary j from the complementary crystallite, taking care to count each twin boundary only once.

A Lagrangian (L) can be written and minimized using a linear combination of the variables $Q_l = \sum_q a_q m_q + \sum_r b_r n_r + \sum_s c_s n'_s + \sum_t d_t p_t$ as below:

$$(A.3) \quad \frac{\partial L}{\partial Q_l} = 0 = \sum_i \gamma_i \frac{\partial M_i}{\partial Q_l} + \sum_j \gamma_{twin} \frac{\partial N_j}{\partial Q_l} + \sum_k \gamma_{eff} \frac{\partial P_k}{\partial Q_l} + 2\lambda \frac{\partial V}{\partial Q_l}$$

Now, differentiating the volume over a given variable gives:

$$(A.4) \quad \frac{\partial V}{\partial m_u} = M + u = \frac{1}{2} \left(\sum_i m_i \frac{\partial M_i}{\partial m_u} + \sum_j \left(n_j \frac{\partial N_j}{\partial m_u} + n'_j \frac{\partial N'_j}{\partial m_u} \right) + \sum_k p_k \frac{\partial P_k}{\partial m_u} \right)$$

Grouping together all remaining, non-zero terms of the differentiation over all of Q_l yields the following from the differentiated Lagrangian:

$$(A.5) \quad \frac{\partial L}{\partial Q_l} = 0 = \sum_i (\gamma_i - \lambda m_i) \frac{\partial M_i}{\partial Q_l} + \sum_j (\gamma_{twin} - \lambda(n_j + n'_j)) \frac{\partial N_j}{\partial Q_l} + \sum_k (\gamma_{eff} - \lambda p_k) \frac{\partial P_k}{\partial Q_l}$$

where the solution, given a general Q_l , is:

$$(A.6) \quad \lambda = \frac{\gamma_i}{m_i} = \frac{\gamma_{twin}}{(n_j + n'_j)} = \frac{\gamma_{eff}}{p_k}$$

The symmetry of opposing faces in a twin boundary, $n_j = n'_j$, allows further simplification to:

$$(A.7) \quad \lambda = \frac{\gamma_i}{m_i} = \frac{\gamma_{twin}}{2n_j} = \frac{\gamma_{eff}}{p_k}$$

The factor of $\frac{1}{2}$ is associated with the twin energies since each crystallite is treated individually, confirming that there is no double counting of these energies.

APPENDIX B

Substitution of γ_{eff}

Considering the Wulff construction for a strongly faceted particle, the following relationships can be applied:

- (1) The contribution to the total volume from a surface i with an incremental area dA_i is: $dV = \frac{1}{3}\gamma_i dA_i$
- (2) If one assumes all surfaces and interfaces are perfectly flat and faceted: $\int \gamma(\hat{n}dA = \sum_i \gamma_i A_i$

The interface of an individual crystallite, can be separated from the other surfaces in the ϵ_w term and Equation 5.2 can be rewritten as follows for that single crystallite after applying the previously mentioned relationships:

$$(B.1) \quad \epsilon_w(h) = \frac{1}{\gamma_{111}} \frac{\sum_i \gamma_i A_i + \gamma_{int} A_{int}}{(\int dV(h))^{\frac{2}{3}}}$$

Now summing this expression over j individual crystallites, the sum of the interfacial contributions can be separated:

$$(B.2) \quad \sum_j \epsilon_{w,j} = \sum_j \left[\frac{1}{\gamma_{111}} \frac{\sum_i \gamma_i A_i + \gamma_{int} A_{int}}{(\int dV(h))^{\frac{2}{3}}} \right]_j = \sum_j \left[\frac{1}{\gamma_{111}} \frac{\sum_i \gamma_i A_i}{(\int dV(h))^{\frac{2}{3}}} \right]_j + \sum_j \left[\frac{1}{\gamma_{111}} \frac{\gamma_{int} A_{int}}{(\int dV(h))^{\frac{2}{3}}} \right]_j$$

If we take f_j to be the fraction of the total interfacial area ($A_{int,tot} = \sum_j A_{int,j}$) encompassed by crystallite j such that $f_j = \frac{A_{int,j}}{A_{int,tot}}$, we obtain from the rightmost term of

the previous equation:

$$(B.3) \quad \sum_j \gamma_{int,j} A_{int,j} = A_{int,tot} \sum_j \gamma_{int,j} f_j = A_{int,tot} \gamma_{eff}$$

APPENDIX C

Au Particle Size Statistics

Figure C.1 shows the areal density of Au on the support surfaces calculated from the Au loadings, particle sizes, and support surface areas both before and after catalysis.

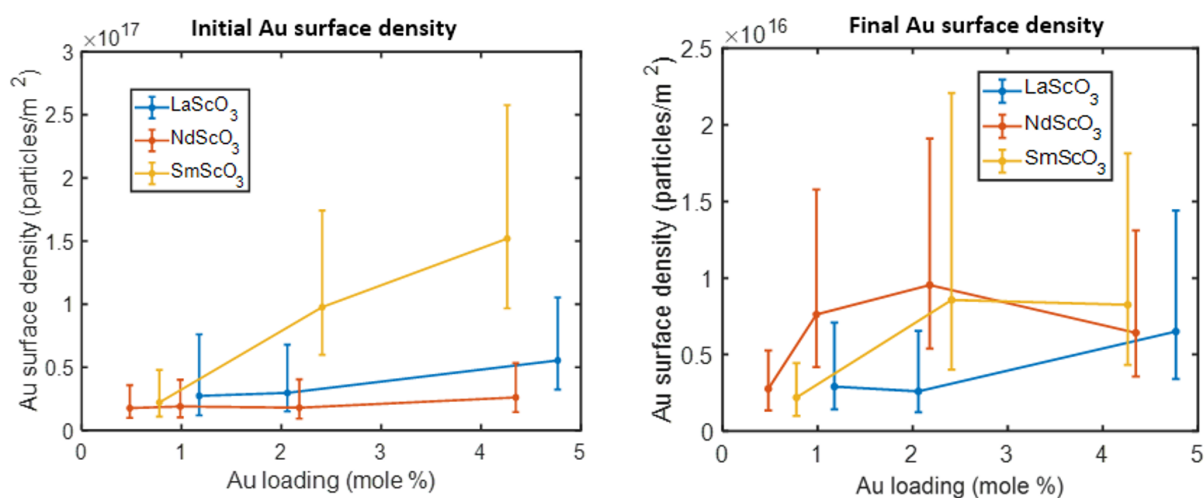


Figure C.1. Surface density of Au nanoparticles both as deposited (left) and after catalytic testing (right).

Table C.1 contains more detailed statistics of the Au particle sizes. The samples on which the Au nanoparticles underwent runaway sintering have a large disagreement between the RMS and mean particle sizes, which is given in the rightmost column with large values bolded. A histogram of the particle size distribution after catalysis on one such sample is shown in Figure C.2. This sample was close to the transition between conventional and runaway sintering, with a mixture of both occurring as evidenced by the bimodal distribution.

Table C.1. Average Au sizes (d_{avg} , given in nm), standard deviations (STD), and RMS disagreement of the post-catalysis samples

Support	Loading (mole %)	d_{avg} (initial)	STD (initial)	d_{avg} (final)	STD (final)	RMS disagreement (RMS - d_{avg})
LaScO ₃	0.18	1.04	0.59	7.21	5.18	1.64
LaScO ₃	0.24	1.33	0.62	3.20	3.08	1.23
LaScO ₃	0.45	1.28	0.36	4.11	4.23	1.79
LaScO ₃	1.18	1.54	0.65	3.44	1.13	0.18
LaScO ₃	2.06	1.94	0.58	4.26	1.47	0.25
LaScO ₃	4.77	2.18	0.46	4.33	1.18	0.16
NdScO ₃	0.48	1.45	0.34	2.06	1.02	0.24
NdScO ₃	0.99	1.77	0.45	2.42	0.60	0.07
NdScO ₃	2.18	2.33	0.66	2.95	0.68	0.08
NdScO ₃	4.35	2.65	0.63	4.22	1.01	0.12
SmScO ₃	0.26	1.16	0.66	11.61	10.32	3.85
SmScO ₃	0.56	1.38	0.44	3.29	3.32	1.38
SmScO ₃	0.78	1.41	0.52	2.41	1.51	0.43
SmScO ₃	2.41	1.43	0.27	2.99	1.04	0.18
SmScO ₃	4.26	1.50	0.26	3.77	1.05	0.14

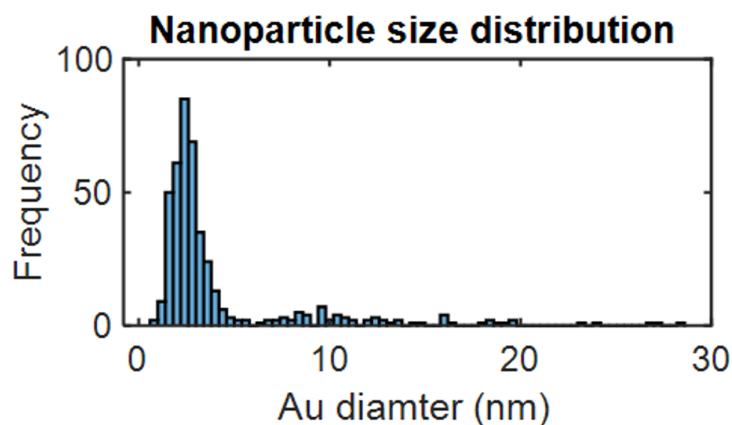


Figure C.2. Au size distribution after catalytic testing on LaScO₃ with a loading of 0.45 mole %. Due to the runaway sintering in some of the particles, a bimodal distribution develops.

APPENDIX D

Expanded TOF Results

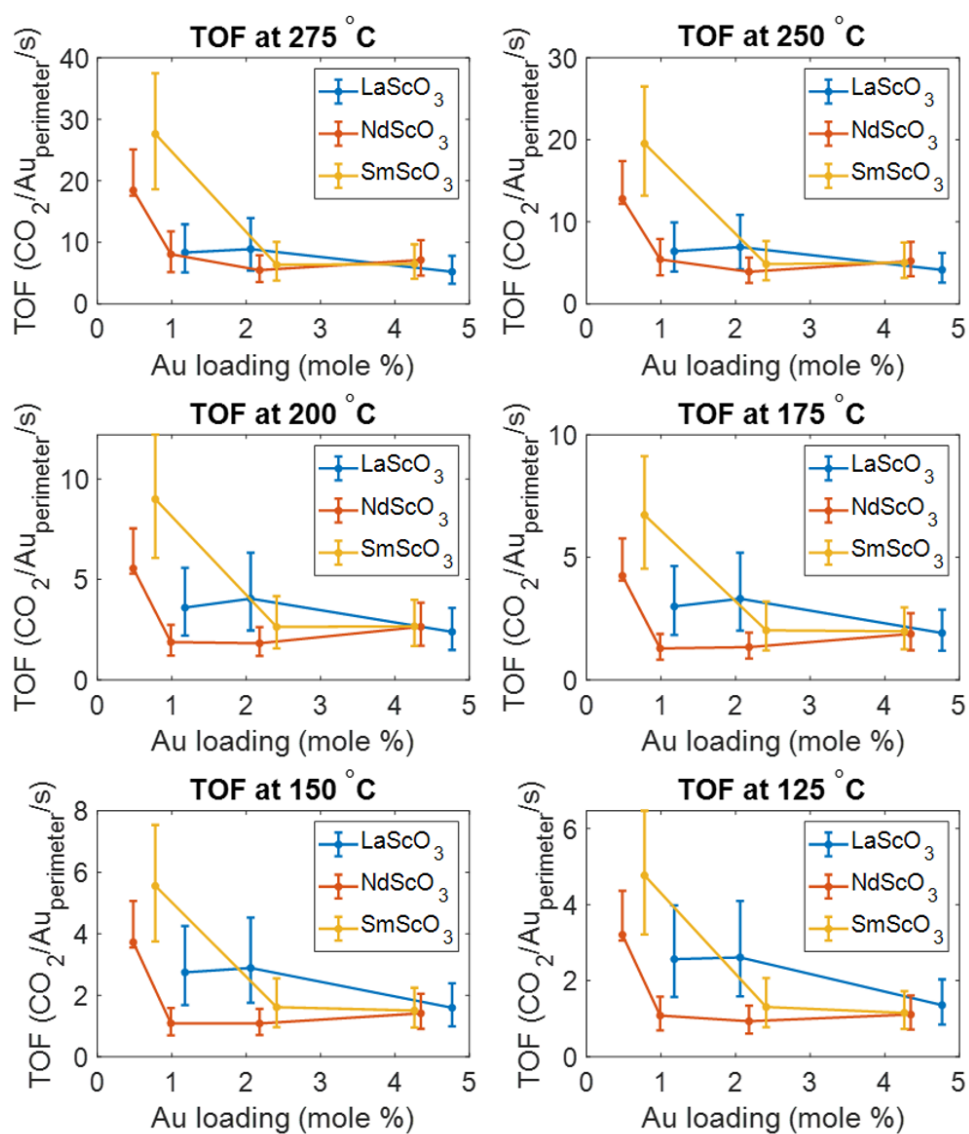


Figure D.1. TOF data from the samples at all measured temperatures using the particle sizes measured after catalysis. Error bars are calculated using the particle standard deviations.

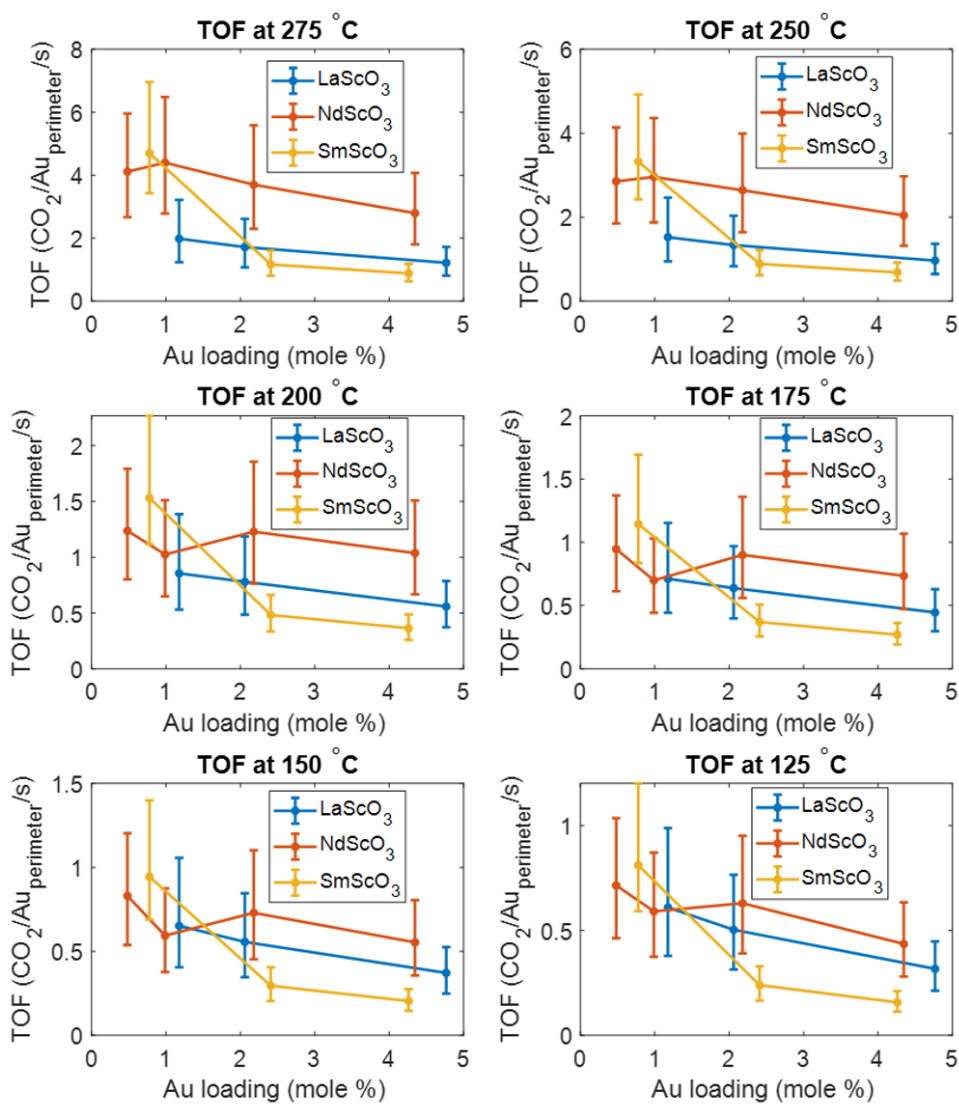


Figure D.2. TOF data from the samples at all measured temperatures using the particle sizes measured before catalysis. As noted in the main text of Chapter 7, the particle sizes measured after catalysis are more representative of the experimental conditions, but these are reported here for completeness and show no unexpected or unrealistic results. Error bars are calculated using the particle standard deviations.

APPENDIX E

Layer Resolved DOS of the Interface

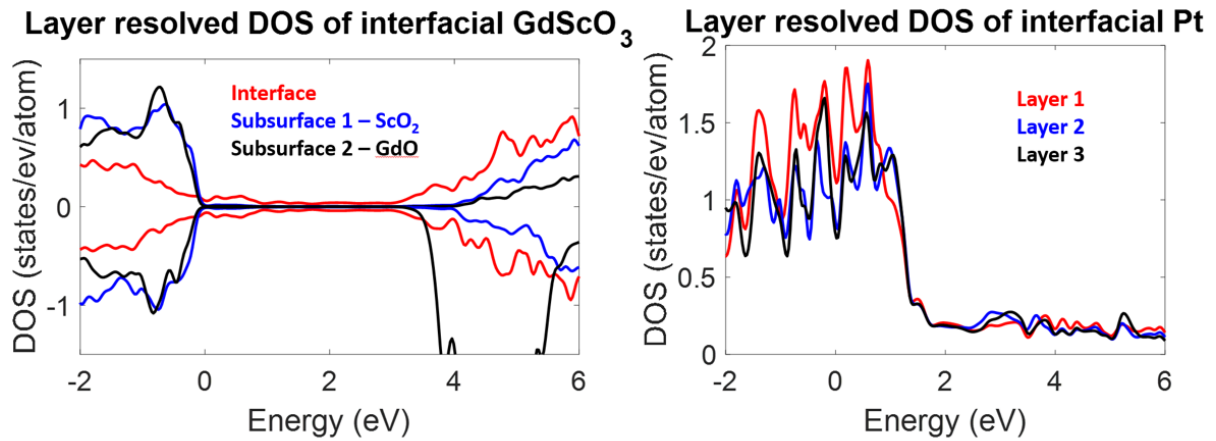


Figure E.1. Layer resolved DOS of the interfacial layers of GdScO_3 and Pt near E_f . In both cases, red represents the layer at the interface, blue is the next nearest, and black is the third layer. As seen, the MIGS largely disappear after the first atomic layer of GdScO_3 , and the Pt is mostly unaffected, though some differences exist at the interfacial layer. In the GdScO_3 DOS, the occupied regions are both O 2p and appear similar, while the unoccupied regions are Sc 3d in Subsurface 1 and Gd 4f in Subsurface 2. Positive values are spin up while negative are spin down.